NUMERICAL SIMULATION OF MECHANICAL AND THERMAL FLUID–STRUCTURE INTERACTION IN LABYRINTH SEALS

Zur Erlangung des akademischen Grades eines

Doktors der Ingenieurwissenschaften (Dr.-Ing.)

vom Fachbereich Maschinenbau
an der Technischen Universität Darmstadt

genehmigte

Dissertation

von

M. Sc. Yu Du
aus Tianjin, V. R. China

Hauptreferent:	Prof. Dr. rer. nat. Michael Schäfer
Korreferent:	Prof. Dr.–Ing. Heinz–Peter Schiffer
Tag der Einreichung:	18. Mai 2010
Tag der mündlichen Prüfung:	14. Juli 2010

Darmstadt 2010
D17

Acknowledgment

It is a great pleasure to thank those who have helped me on the path towards this thesis.

I am deeply grateful for the opportunity to have Professor Schäfer as an advisor for the past three years. I still vividly remember the excitement of receiving the Ph.D. offer at his institute. He has given me sufficient freedom in research, and at the same time the guidance and encouragement when my steps faltered. He taught me how to do research by holding me to a high research standard. Besides, he is astonishingly efficient at revising papers and responding to inquiries, which has become my model of professional dedication.

My co–advisor, Professor Schiffer, as well as Dr. Bornkessel from Rolls–Royce Germany and Dr. Dullenkopf from Universität Karlsruhe have given me many valuable advices. I am sincerely grateful to them for the inspiring discussion that helped me find the research orientation.

Thanks to Dr. van de Loo and Dr. Lazanowski for their efforts to create an academic and friendly atmosphere at the graduate school. Thanks to Carina Schuster, Heike Hoffmann, and Monika Müller for being amazingly cheerful, kindhearted, and patient. I would also like to thank the system administrators, Christian Schmitt and Michael Fladerer, for ensuring an up–to–date and stable system environment that I never had to worry about installing software or losing files.

I am also heartily thankful to my FNB colleagues who share an interest in numerical methods. They showed me how to question thoughts and express ideas. I would like to acknowledge Saim Yigit for leading me into the world of FASTEST and FSI. I have enjoyed the friendship of my fellow graduate students at the graduate school. My sincere thanks to my fellow scholarship holders of the Graduiertenkolleg for the valuable discussion.

I have been truly fortunate to share an office with Stephen Sachs who not only proofread my thesis but also tolerated my German. He is a generous and humorous person, and really enthusiastic about mathematics. Our arguments about engineering and mathematical issues have benefited me tremendously. The many weekends and evenings of overtime we spent together in the office will be my precious memory.

I deeply appreciate the efforts of Xiaohui Guo, my college roommate, who helped

Contents

List of Tables

x

List of Figures

Nomenclature

Latin letters:

$\mathbf{a}$	nodal displacements (m)
A	area (m^2)
$\mathbf{b}$	body force per unit mass (m/s^2)
c	fluid speed of sound (m/s)
c_p	fluid specific heat capacity at constant pressure (J/kg K)
c_s	solid specific heat (J/kg K)
$\mathbf{C}$	elasticity tensor (Pa)
C_{stiff}	exponent of mesh stiffness model
C_μ	$k - \varepsilon$ turbulence model constant, $= 0.09$
d	displacement (m)
$\mathbf{D}$	strain rate tensor (s^{-1})
e	internal energy per unit mass (J/kg)
ec	eccentricity (m)
E	Young's modulus (Pa)
$\mathbf{E}$	Green–Lagrangian strain tensor
$F, \mathbf{f}$	force (N)
h	enthalpy (m^2/s^2)
H	channel height (m)
htc	heat transfer coefficient (W/m^2 K)
$\mathbf{I}$	identity tensor
k	turbulent kinetic energy (m^2/s^2)
$\mathbf{K}$	stiffness (N/m)
$L, \mathbf{l}$	length (m)
$\dot{m}$	mass flow (kg/s)
$\mathbf{M}$	mass (kg)
n	rotational speed (rpm)
$\mathbf{n}$	unit normal vector
$\mathbf{N}$	shape functions
p	pressure (Pa)
$\mathbf{q}$	heat flux (W/m^2)

$\dot{Q}$	heat flow (W)
$\dot{Q}_{id}$	expansion function ($\sqrt{\text{kg K/J}}$)
R	radius (m)
$\Re$	specific gas constant (J/kg K)
$\mathbf{S}$	second Piola–Kirchhoff stress tensor (Pa)
S_E	energy source (W/m^3)
S_ϕ	source of ϕ
t	time (s)
$\mathbf{t}$	surface force (Pa)
T	temperature (K)
$\mathbf{T}$	stress tensor (Pa)
$U, \mathbf{u}$	displacement (m)
$v, \mathbf{v}$	velocity (m/s)
V	control volume size (m^3)
$\mathbf{W}$	spin tensor (s^{-1})
$x/y/z$	x/y/z Cartesian coordinate (m)
$\mathbf{x}/\mathbf{X}$	Eulerian/Lagrangian coordinates (m)

Greek letters:

α	coefficient of thermal expansion (K^{-1})
β	numerical parameter in Newmark–β methods
γ	numerical parameter in Newmark–β methods
Γ	domain area (m^2)
Γ_{disp}	mesh stiffness (m^2/s)
$\boldsymbol{\delta}$	displacement relative to the previous mesh locations (m)
Δ	difference
ε	dissipation rate of the turbulent kinetic energy (m^2/s^3), RMS convergence target
$\boldsymbol{\varepsilon}$	Cauchy strain tensor
θ	amplitude decay factor
κ	ratio of specific heats
λ	thermal conductivity (W/m K)
λ_ϕ	diffusivity of ϕ
μ	dynamic (molecular) viscosity (kg/m s)
μ_{eff}	effective viscosity (kg/m s)
μ_t	turbulent (eddy) viscosity (kg/m s)
ν	Poisson's ratio
ρ	density (kg/m^3)
$\boldsymbol{\sigma}$	Cauchy stress tensor (Pa)
$\boldsymbol{\tau}$	stress deviator tensor (Pa)

τ_w	wall shear stress (Pa)
ϕ	variables transferred across the fluid–solid surface, scalar fluid variable
φ	flow factor (kg $\sqrt{\text{K}}$/MPa m s)
ψ	heat source (W/kg)
ω	angular velocity (rad/s)
Ω	domain volume (m^3)

Subscripts:

0	initial values
f/s	fluid/solid field
id	ideal
in/out	inlet/outlet condition
$lift$	lift force
new/old	value at the current/last FSI iteration
sum	sum value
tan	circumferential direction
$tot/stat$	total/static value
$x/y/z$	x/y/z direction in Cartesian coordinate system

Superscripts:

ec/d	value due to displacement ec/d
el/th	elastic/thermal tensor
g	grid
int/ext	internal/external values
JD	related to Jaumann stress rate and strain rate
log/nom	logarithmic/nominal strain
SE	related to second Piola–Kirchhoff stress and Green strain
$^-$	mean value
$'$	fluctuating component

Dimensionless numbers:

C_D	$\dot{m}/\dot{m}_{id}$, discharge coefficient
K_{out}	$v_{tan}/\omega R$, outlet swirl ratio
M_{tan}	$\omega R/c$, circumferential Mach number
Nu	$htc\,L/\lambda_f$, Nusselt number
Re	$\rho v L/\mu$, Reynolds number
y^+	dimensionless wall distance
π	$p_{tot,in}/p_{stat,out}$, pressure ratio

σ $\qquad$ $c_p \, \Delta T_{tot}/\omega^2 R^2$, windage heating coefficient

Chapter 1

Introduction

1.1 Labyrinth Seals in Jet Engines

Non–contacting gas seals in jet engines are mainly used to reduce the leakage flow between components of different pressures and prevent the rotor from contacting the stator. Since the rotor rotates at a very high speed, any contact between the rotor and the stator can damage the seal, cause deterioration of seal performance, and lead to engine failures eventually.

One of the most important non–contacting seals is called the labyrinth seal, which is named after its shape. As shown in Fig. 1.1, the seal is composed of alternating teeth and cavities. Despite the recent advanced sealing techniques, labyrinth seals remain the most common non–contacting seals in modern jet engines. They can be found in many locations serving significant purposes, for example, to reduce the mass flow at blade shrouds, to control the cooling air in order to prevent hot gas ingress, and to minimize stage losses in turbines [1].

By employing labyrinth seals, contactless sealing is provided at stationary/rotating surfaces with certain amount of leakage [2], which is counted as a major source of losses. However, sufficient tip clearances are mandatory in baseline designs of labyrinth seals owing to the inevitable transient structural and thermal deformations during operations. Therefore, great challenges are imposed on the design of labyrinth seals to ensure that: 1) sufficient gaps are maintained between the rotating/stationary components; 2) the leakage is minimized to decrease fuel consumption, enhance thrust, and thus improve the overall engine performance [3].

In addition to investigations of leakage behaviors, the trend of increasing turbine inlet temperature and pressure ratio in modern jet engines requires more comprehensive and accurate predictions of other seal performances, such as swirl development and heat transfer, which haven't been thoroughly studied in the past. In particular, heat transfer investigations mainly focus on the fluid–solid heat exchange and the total temperature increase due to internal losses. The latter is also called the windage

1
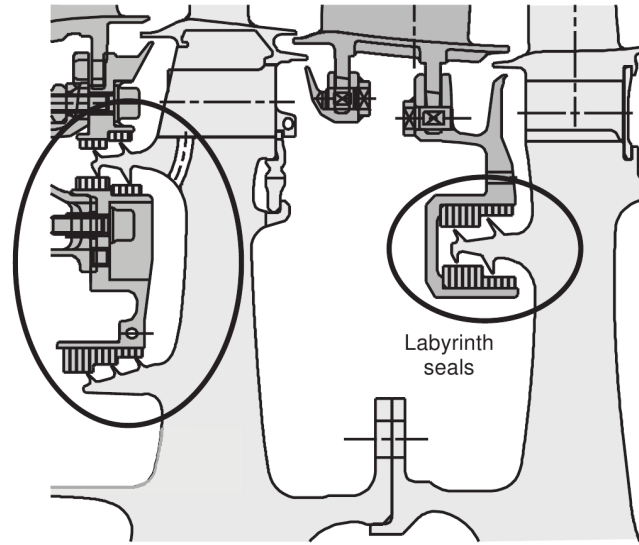
Figure 1.1: Labyrinth seals in the high pressure turbine cooling air system from the BR700 series (Denecke et al., 2005)

heating. For example, the windage heating plays a significant role when the cooling air runs through labyrinth seals and chills the turbine blades. As the cooling air is heated up via the windage heating, the cooling performance is strongly degraded and thus the blade lifetime is shortened. Another example shows the importance of studies on swirl development. The incidence angle of downstream blades, which is a major factor of stage losses, are strongly dependent on the exit–swirl of interstage labyrinth seals [4].

The involvement of high rotational speed and high gas temperature in jet engines causes complex physics in labyrinth seals. In general, there are three dominant effects that need to be considered, which are the centrifugal effect, the thermal effect, and the rotor vibration induced by fluid forces [5]. The centrifugal force and thermal expansions can lead to significant growth of rotor in radial direction and affect the tip clearance as a result. Moreover, the tip clearance changes with rotational speed and gas temperature accordingly under different flight conditions. Bending vibrations of the rotor excited by fluid forces can also invoke radial displacements and cause instability issues.

It can be concluded that all effects discussed above involve fluid–structure interactions (FSI). However, most works found in literature aimed at solving such problems using decoupled approaches. For example, the fluid induced vibration is usually studied using rotordynamic models, which assume equations of motion for the rotor and use fluid forces to determine the equation coefficients. However, structural impacts on the fluid field are totally neglected. The centrifugal and thermal FSI effects have been observed in some experimental studies. Delgado and Proctor (2006) [6] found

that the two effects cause the leakage to increase by up to 70%. Similarly, the experiments of Waschka et al. (1992) [7] shows centrifugal growths and thermal expansions of up to 50% of the original clearance. In some numerical studies, the two effects are accounted for by modifying the geometry of the fluid model using measured centrifugal and thermal growths. Such examples can be found in the CFD models by Millward and Edwards (1996) [8]. Denecke also adopted and extended the approach to rotating stepped labyrinth seals [1].

In the numerical investigations above, it is always necessary to make assumptions in order to decouple the sophisticated FSI problems. However, since the fluid and the structure affect each other strongly in reality, it indeed requires fully coupled FSI modeling.

In addition to the lack of profound research in FSI induced structural deformation, another gap is the use of empirical models to estimate the heat transfer between fluid and solid, which is crucial for the thermal design of labyrinth seals. For example, semi–experimental semi–numerical methods are applied to determine heat transfer coefficients and Nusselt numbers in [9, 10]. In particular, temperatures are first measured in the fluid field and the structure separately, and then fed to thermal finite element analysis as boundary conditions in order to calculate the heat flow. Although the method is straightforward, it is associated with two major drawbacks. First, the involvement of experiments is expensive; second, the accuracy is restrained by experimental equipments and metrology. For example, as the typical size of labyrinth seals is small, it not only restricts the maximum number of measuring points, but also behaves poorly in existence of sudden change of geometries [9]. In brief, the fluid–solid heat transfer is beyond the capability of traditional single field analyses and requires multifield coupling.

To summarize, by introducing fully coupled FSI simulations, the current study of labyrinth seals can be enriched in terms of: 1) studying FSI effects that are beyond the scope of separate CFD or Computational Solid Mechanics (CSM) simulations; 2) reducing potential errors introduced by single field approximations; 3) obtaining additional information and more accurate predictions of fluid and solid fields.

1.2 Previous Work on Labyrinth Seals

Recent research on labyrinth seals mainly focuses on experimental and numerical studies of leakage, heat transfer, rotordynamic effects, seal configurations and seal power loss. There are also some efforts putting on theoretical studies of these issues.

1.2.1   Review of Experimental Studies

Among experimental investigations, leakage is the most common parameter being studied. Proctor and Delgado (2004) [11] tested leakage of labyrinth seals (Fig. 1.2) and other competing non–contacting seals for operating conditions of room temperature and stationary rotor. Test results showed that both the brush and finger seal offered substantial improvements in leakage performance over labyrinth seals. Later they studied the leakage and power loss of labyrinth seals at various temperatures, seal pressure drops, and rotational speeds [6]. They found out that the seal leakage decreases with the increase of rotational speed due to centrifugal growth of the test disk, which reduces the tip clearance and increases with test temperature due to thermal growth outward from the disk which results in larger seal clearance. Furthermore, seal power loss increases with rotational speed, seal pressure drop, mass flow, and radial clearance. In experiments conducted by Gamal and Vance (2008) [12], the effects of tooth thickness, tooth profile, and eccentric rotor on leakage were examined through a series of non–rotating tests. They found out that by doubling the tooth thickness the mass flow can be reduced by up to 20%, possibly due to increase of frictional losses. Besides, reduction in cavity depth has virtually no impact on leakage. However, they did not reach to a consistent conclusion on how the tooth profile can influence leakage. In addition, they observed increase of leakage with eccentricity.
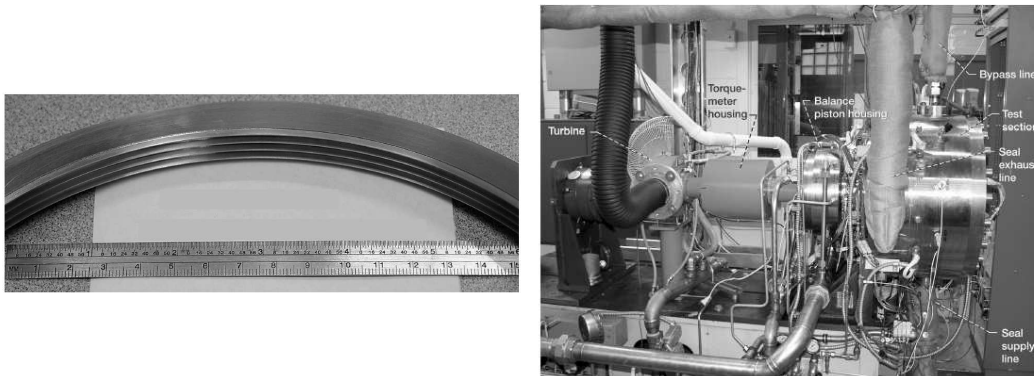
Figure 1.2: Four–knife labyrinth seal and seal test rig (Proctor and Delgado, 2004)

Initial experimental work on heat transfer in labyrinth seals can be traced back to 1988, when Wittig et al. [9] tested leakage and heat transfer of stepped labyrinth seals for different geometries and pressure ratios. Flow and wall temperatures of seal components were first measured and then applied to a finite element program to determine heat transfer coefficients and Nusselt numbers. In addition, they simulated the flow with a finite difference code and used analogies to calculate the wall heat flux and Nusselt numbers. However, the numerical and experimental Nusselt numbers didn't agree at the teeth and step locations. Waschka et al. (1992) [7]

used similar experimental approaches to investigate discharge and heat transfer coefficients in rotating stepped labyrinth seals. Measurements showed that the clearance can be reduced by approximately 50% due to centrifugal growth and thermal expansion, which demonstrates the significance of rotation on reducing the leakage and enhancing the heat transfer. They also did a parallel numerical study using a finite volume code [10, 13, 14], the results of which confirmed the conclusions they reached by experimental efforts. In addition, they also found that the Nusselt numbers for different tip clearance sizes are almost identical. Millward and Edwards (1996) [8] presented results of windage heating in high–speed seals on various designs and derived a correlation to predict windage heating in labyrinth seals without honeycomb. Their research work indicated that the windage heating power increases with mass flow, rotational speed, nominal radius, and surface area. In the experiments done by Willenborg et al. (2001) [15], the influences of Reynolds number, pressure ratio, and tip clearance on leakage and heat transfer in a stepped labyrinth seal were determined. The same finite element procedure as in [9] was used to calculate the heat transfer coefficients and Nusselt numbers. The discharge coefficient turned out to have stronger dependence on the Reynolds number than on the pressure ratio. In particular, Nusselt numbers continuously increase with the increase of Reynolds numbers. Based on the same numerical and test approach, Willenborg et al. (2002) [16] also included a honeycomb facing in the stepped labyrinth seal. The results revealed a significant reduction of heat transfer with the honeycomb facing. Denecke et al. (2005) [4] measured windage heating and exit–swirl in stepped labyrinth seals with honeycomb; see Fig. 1.3 for the test rig. Accurate prediction of these variables is of increasing importance in current turbomachineries. The test data, in turn, will help with model validation.
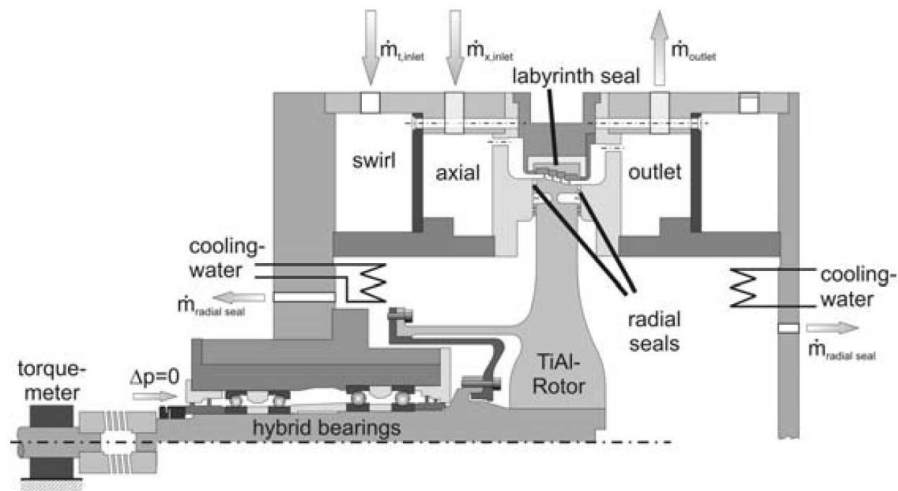
Figure 1.3: Schematic view of the test rig section (Denecke et al., 2005)

In order to understand rotordynamic effects, Kwanka (2000) [17] presented a novel experimental procedure for the identification of rotordynamic coefficients, and found out that the stepped labyrinth seal has less favorable rotordynamic properties than a straight–through seal. Later, Kwanka (2001) [18] used this procedure to test various methods of improving seal stability. Swirl brakes at the entrance of the seal are highly effective, while the use of honeycomb generates larger excitation. Therefore, a honeycomb in combination with swirl brakes is recommended for both good sealing and good rotordynamic performance. An example of utilizing rotordynamic coefficients for overall rotor analysis can be found in [19]. In this work, Shen et al. (2007) used the stiffness and damping coefficients of labyrinth seals presented in reference [2] to calculate the nonlinear dynamics and stability of a rotor–bearing–seal system analytically.

Complex seal configurations are the focus of many experiments. To improve understandings of the feature "annular groove" in stepped labyrinth seals, Rhode et al. (1997) [20] observed the through–flow jet penetration into the annular groove using a water leakage and flow visualization facility. They found that the presence of an annular groove on the stator can result in higher leakage resistances. Later, they (1997) [21] used the same procedure to determine the geometry–leakage relationship for stepped labyrinth seals with another feature, "sloping surfaces". It was found that the combination of a sloping surface and a curved surface on the rotor within the cavities will lead to a significant leakage reduction. Michaud et al. (2003) [22] conducted tests on a 2D stepped labyrinth seal in order to understand the influence of geometry and flow parameters on leakage and velocity field. With moderately modified geometry, a leakage reduction of up to 17% was achieved. Abradable lands in current labyrinth seals allow the teeth to rub grooves into the stator. In an experimental investigation of 2D labyrinth seals, Denecke et al. (2003) [23] presented the influence of various rub–groove geometries on seal leakage. They also showed the main flow mechanisms induced by rub–grooves using water–channel visualization.

More details of the aforementioned experiments, such as seal configurations and operating conditions, are listed in Tab. 1.1 for comparison.

Table 1.1: Seal configurations and operating conditions in previous experimental investigations

Research group	2D planar /3D	straight– through	stepped	honey- comb	rotating	hot air	max. press –ure ratio	inlet swirl	eccentric rotor
Denecke et al. (2003)	2D planar	x	x				(water)		
Denecke et al. (2005)	3D		x	x	x		1.3	x	
Gamal&Vance (2008)	3D	x					6.8		x
Kwanka (2000)	3D	x	x		x		2.0		
Kwanka (2001)	3D	x		x	x		2.0	swirl brakes	
Michaud et al. (2003)	2D planar		x				10.0		
Millward&Edwards (1996)	3D	x	x		x		1.9		
Proctor&Delgado (2004)	3D	x					6.1		
Proctor&Delgado (2006)	3D	x			x	x	6.1		
Rhode et al. (1997)	2D planar		x				(water)		
Schramm et al. (2002)	2D planar		x	x			1.6		
Waschka et al. (1991–1993)	2D planar	x	x		x	x	2.0		
Willenborg et al. (2001, 2002)	2D planar		x	x		x	1.6		
Wittig et al. (1988)	2D planar	x	x			x	2.5		

1.2.2   Review of Numerical Studies

Numerical studies of labyrinth seals mostly refer to CFD simulations of the flow through seals. CFD is used to reveal flow details and to predict the leakage. Back in 1993, Rhode and Hibbs (1993) [24] used a Navier–Stokes finite difference code to model leakage of a straight–through labyrinth seal with given inlet and outlet pressures. The numerical results were in good agreement with test measurements, with a leakage discrepancy of less than 8%. Schramm et al. (2004) [25] applied an annealing optimization model to minimize the leakage through a stepped labyrinth seal, using step position and height as variables. They found that varying step positions can lead to changes in flow patterns. It was found that the combination of a large step distance to the upstream knife and a large step height is most effective in reducing leakage. With the aid of CFD simulations, Wang et al. (2004) [26] studied the behavior of the flow through stepped labyrinth seals in the presence of disengagement. The distance from tooth tip to step was found to influence leakage significantly. Vakili et al. (2005) [27] presented their numerical work on the same stepped labyrinth seal as in [22]. This effort is to understand the mechanisms behind leakage reduction and total pressure loss. In particular, they looked into factors such as turbulence induced viscous losses, cavity vortex generation, flow stagnation losses, and increased flow streamline curvature. Li et al. (2006) studied rotating straight–through and stepped labyrinth seals (Fig. 1.4) in [28] to determine the influence of pressure ratio and fin pitch on leakage. Based on modeling, they showed that the leakage decreases as fin pitch or inlet/outlet pressure ratio decreases. However, the numerical results were not validated against any experiments.
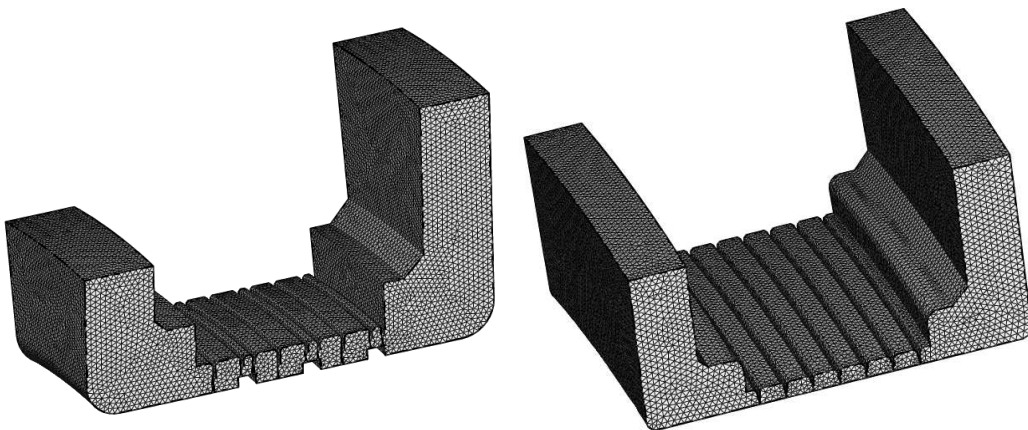
Figure 1.4: Computational grid of the stepped and the straight–through labyrinth seals (Li et al., 2006)

Numerical methods are widely used in determining rotordynamic coefficients. In order to calculate fluid forces, 3D CFD simulation is required. Moore (2003) [29]

used CFD to predict leakage and rotordynamic forces. Their results demonstrate improved leakage and rotordynamic predictions over bulk–flow approaches. Hirano et al. (2005) [30] calculated the rotordynamic force of a 3D labyrinth seal using CFD. Compared with bulk–flow methods, the CFD results showed a lower prediction of the destabilizing forces. However, the numerical results were not validated with any test results. Schettel et al. (2005) [31] did calculations of stiffness coefficients and the numerical results were validated against test data. It is shown that the stiffness coefficients are functions of pressure drop, rotational speed, and entrance swirl. In this study, a missing part was further discussion on damping coefficients.

CFD simulation also assists researchers greatly in gaining insights of flow associated with complex seal configurations. Schramm et al. (2002) [32] presented numerical predictions and experimental investigations of leakage and velocity field to understand the flow patterns in stepped labyrinth seals with honeycomb structures. The numerical results agreed well with test data and showed very detailed features for the flow into the honeycomb. It was found that the honeycomb facing can result in an increase of leakage. Choi and Rhode (2004) [33] proposed to approximate a 3D flow by employing a 2D CFD model in a honeycomb labyrinth seal, which can highly reduce computational costs. Leakage predictions were compared among cases. The numerical results also showed close agreements with measurements. In reference [34], Soemarwoto et al. (2007) numerically investigated the flow characteristics in labyrinth seals with honeycomb land and canted knives. They identified the effects of honeycomb and canted knives with respect to decreased production of losses.

There were also some attempts in applying numerical investigations to heat transfer effects, where experimental studies dominate. For example, Denecke et al. (2005) [4] simulated a stepped labyrinth seal with honeycomb to evaluate the ability of the numerical model to predict windage heating, exit–swirl, and velocity profiles. The numerical results showed excellent agreement with test results. Yan et al. (2009) [35] studied the leakage and windage effects in stepped labyrinth seals with honeycomb lands with numerical approaches (Fig. 1.5). They determined how pressure ratio and clearance size can affect the discharge coefficient and windage heating number.

In Tab. 1.2, there is a summary for the seal designs, CFD codes, and turbulence models used in the numerical investigations mentioned above.

Compared to the numerical effort put into the areas above, only a few publications on FSI simulations of labyrinth seals are available, and these rare examples are discussed in this paragraph. In his dissertation [36], Lange (2005) simulated a 2D planar straight–through labyrinth seal with a flexible rotor and presented the rotor vibration induced by the flow under different pressure ratios. He showed that, in principle, it is feasible to apply the in–house approach to FSI in labyrinth seals. However, there is a lack of supporting parameter studies. Kudriavtsev et al. (2003) [37] simulated the steady one–way FSI in a finger seal, where the calculated fluid forces were passed to the structural solver and applied as loads on the seal components. Fujita and
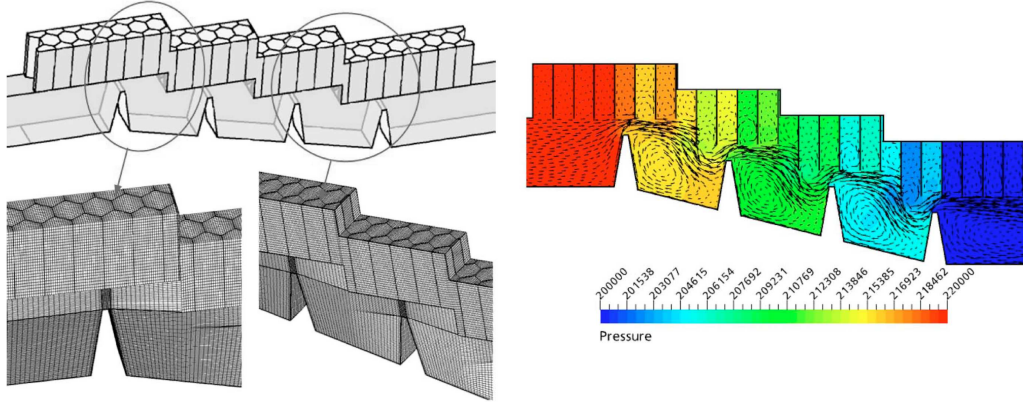
Figure 1.5: Mesh and static pressure distribution (Pa) of the stepped labyrinth seal with honeycomb land (Yan et al., 2009)

Kato (2004) [38] simplified labyrinth seals to thin cylindrical shells with a fixed end and a freely supported end, where the inner shell was elastic and the outer rigid. Then, they did an analytical study on the vibration considering FSI between shells and fluids flowing through a narrow passage. The latter two investigations extremely simplified the coupling characteristics and the geometry of labyrinth seals.

1.2.3   Review of Theoretical Studies

In comparison with numerous experimental works and booming numerical analyses, there has been only a few theoretical studies published over the last years. However, these analytical models can help us to better understand the mystery between parameters and phenomena. For example, Yucel and Kazakia (2001) [39] presented analytical approaches for leakage prediction. The study extended to higher inlet/outlet pressure differences by incorporating pressure dependent flow coefficients. The results compared favorably with CFD calculations. In the presence of a non–axisymmetric rotation of the rotor in a stepped labyrinth seal, Eser (2002) [40] calculated the rotor-dynamic coefficients by analytically solving the continuity and momentum equations. For non–rotating labyrinth seals, there is an existing set of dimensionless numbers to characterize leakage and heat transfer. Denecke et al. (2005) [41] extended the set of non–dimensional numbers for rotating labyrinth seals to cover swirl and windage heating using the dimensional analysis theorem. As part of the continuous work, Denecke et al. (2008) proposed analytical approaches in [42] to predict the discharge behavior, swirl development, and overall total temperature increase.

Table 1.2: Seal designs and numerical approaches in previous CFD investigations

Research group	2D/3D	straight–through	stepped	honey-comb	rotating	hot air	inlet swirl	CFD code	turbulence model
Choi&Rhode (2004)	3D		x	x				Star–CD	$k-\varepsilon$
Denecke et al. (2005)	3D		x	x	x		x	FLUENT	realizable $k-\varepsilon$
Hirano et al. (2005)	3D	x			x		x	CFX–TASCflow	$k-\varepsilon$
Li et al. (2006)	3D	x	x		x		x	FLUENT	$k-\varepsilon$
Millward&Edwards (1996)	2D	x	x		x			PACE	$k-\varepsilon$, near wall $k-l$
Moore (2003)	3D	x			x		x	SCISEAL	$k-\varepsilon$
Rhode&Hibbs (1993)	2D	x			x			(FD based)	$k-\varepsilon$
Schettel et al. (2005)	3D	x			x		x	CFX–TASCflow	$k-\varepsilon$
Schramm et al. (2002, 2004)	3D		x	x				TASCflow3D	$k-\varepsilon$
Soemarwoto et al. (2007)	3D		x	x	x	x		ENSOLV	TNT $k-\omega$
Vakili et al. (2005)	2D		x		x	x		FLUENT	$k-\varepsilon$
Wang et al. (2004)	2D		x					FLUENT	RNG $k-\varepsilon$
Waschka et al. (1991–1993)	2D	x	x		x	x		(FV based)	$k-\varepsilon$
Wittig et al. (1988)	2D	x	x			x		(FD based)	$k-\varepsilon$
Yan et al. (2009)	3D		x	x	x		x	CFX	$k-\varepsilon$

1.3   Numerical Simulation of FSI – State of the Art

1.3.1   Progress in FSI Research

Over the past years, FSI has attracted growing interests and has become one of the major focuses in the field of computational engineering [43]. Generally, there are two main approaches for FSI problems: the monolithic approach, which solves the governing equations of fluid and solid in a single solver; and the partitioned approach, which in contrast solves the governing equations separately in two distinct solvers. In the partitioned approach, it requires communication between two solvers at interfaces and, therefore, involves various coupling algorithms. There are two main categories of coupling algorithms, which are one–way and two–way coupling. One–way coupling refers to the case where the data transfer is unidirectional, and two–way coupling means bidirectional data transfer. Two–way coupling can be further divided into explicit and implicit method. In the former case, data is exchanged only once per timestep, while in the latter case, it allows for several FSI iterations within each timestep till convergence is reached.

At the institute of the author, numerical methods for FSI have been a main focus [44, 45], and an implicit partitioned coupling approach of two–way FSI [46] has been developed by combining the multigrid fluid solver FASTEST [47] and the FEM based structural solver FEAP [48] via the coupling interface MpCCI [49]. This approach has been continuously improved to meet requirements set by sophisticated FSI problems. In [50], the approach was verified by the well–known laminar FSI benchmark [51]: good agreements have been observed between numerical results and reference values. An elliptic grid smoothing technique was implemented to cope with large structural displacements in FSI [52, 53] as shown in Fig. 1.6. In addition, a case of turbulent FSI was presented in [53]. Later this approach was extended to thermal FSI, as well as turbulent FSI using LES [54].
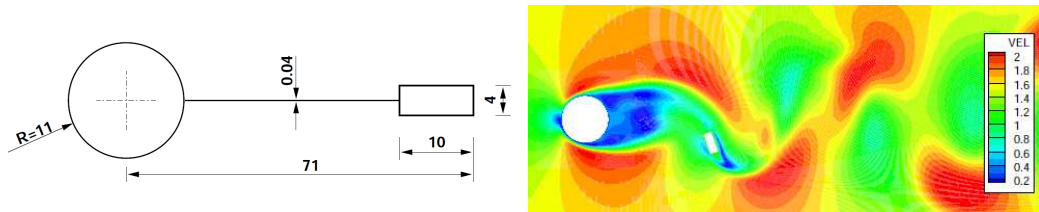
Figure 1.6: FSI simulation with large structural deformations (Yigit, 2008)

The monolithic approach has an advantage in robustness, but requires an extra code for the combined governing equations. In [55], a monolithic approach based on finite volume method (FVM) was developed and applied to several basic test cases. Another displacement based FVM approach was proposed in [56]. However, its application was restricted to simple structural problems. Meanwhile, a monolithic

finite element method (FEM) multigrid approach was presented by Hron and Turek (2006) [57] to solve the time dependent interaction between an incompressible fluid and an elastic solid.

In comparison with the monolithic case, the partitioned approach is preferred on more occasions due to its better compatibility with existing highly efficient CFD and CSM codes, thus saving the effort of code developing. The communication between different solvers requires a coupling interface to interpolate and exchange data. For this purpose, the Fraunhofer Institute SCAI developed MpCCI [49], a commercial code coupling library. MpCCI supports various commercial simulation codes and provides a programmable interface for in–house codes. An alternative to MpCCI is the academic code called preCICE [58], which has been developed at TU München recently and provides solutions for basic coupling issues, such as data mapping, data communication, and coupling schemes.

One–way coupling is only capable of representing weakly coupled physics, such as thermal–stress problems. When the fluid and the solid significantly affect each other, two–way coupling is needed. Furthermore, explicit methods usually deliver less accurate results and suffer from stability problems. Therefore, they are suitable for simple cases only. In contrast, implicit methods are more favorable and thus adopted in most academic FSI investigations. For example, the stability issues in implicit partitioned approaches were explored by Vierendeels (2009) [59] and Förster et al. (2007) [60] for coupled problems involving incompressible fluids and flexible structures. The introduction of artificial compressibility stabilizing the coupling method was presented as well. Küttler and Wall embedded dynamic relaxation methods [61] and vector extrapolation [62] methods into a partitioned fixed–point FSI solver to improve the simulation efficiency. In [63], van Zuijlen and Bijl (2009) reduced the cost of sub–iterations in implicit partitioned approaches by applying a multilevel acceleration technique. Moreover, Münsch and Breuer (2009) [64] studied several issues of using LES in their implicit partitioned FSI approach, where FASTEST is coupled with the structural code CARAT via the interface CoMa.

1.3.2 Survey of Industrial Applications

As seen in the last section, huge progress has been made in numerical methods of FSI, which allows FSI implementation in industrial cases at affordable computational costs. However, it is also realized that most applications are still at the rudimentary level, where tremendous simplifications are introduced and/or less sophisticated FSI approaches are adopted, like rigid structure, one–way coupling, etc..

Several typical industrial applications of FSI are summarized in Tab. 1.3, and their key numerical features are compared there. Mechanical and thermal FSI refers to cases, the coupling quantities in which are force/displacement and heat flow/temperature, respectively. Steady or transient FSI differs in whether the coupled process

is time dependent. Mesh deformation indicates that the fluid mesh is recalculated on receiving the structural displacements. The focus of the FSI analysis, either on the structure or on the flow, is defined as subject of interest in the last column. The suitability of a monolithic approach for various FSI effects is a crucial feature, since some monolithic approaches target specific FSI effects and drastically simplify the structural or the fluid governing equations. For example, the monolithic approach proposed by Wang et al. (2008) is suitable only for water–plate coupling, where the terms of linear water wave are incorporated into the equations of motion of elastic plates [65]. Similarly, in another monolithic approach developed by Sigrist and Broc (2006–2009), the fluid is modeled by added mass and added stiffness terms in the finite element discretization of the structure, instead of a complete modeling [66, 67].

The increasing popularity of FSI simulations can be seen from Tab. 1.3, covering a wide range of industrial branches. Most of the cases presented here used partitioned approaches, while monolithic approaches are relatively rare. Among various partitioned approaches, the one–way and two–way explicit approaches are dominant compared to the limited applications of the two–way implicit method. However, the former two are limited to simple or weakly coupled FSI effects; in some extreme cases, the fluid mesh does not need to be deformed. With growing industrial demands for more accurate simulations of more complex FSI effects, the implicit method for two–way FSI will thrive in the foreseeable future.

Another trend can be recognized from Tab. 1.3, that present FSI simulations usually serve for the purpose of structural analysis.

1.4 Goals of the Study

The thesis aims at investigating various FSI effects in labyrinth seals by means of numerical simulations. It consists in three main goals:

- Verify the accuracy and evaluate the efficiency of the numerical tool in parallel computations against the FSI benchmark.

- Study the fluid force induced vibrations in non–rotating labyrinth seals using 3D transient FSI models. The purposes are to predict rotor oscillations numerically and study the influences of pressure difference and mass flow quantitatively.

- Investigate the centrifugal growth and fluid–solid heat transfer in rotating high–temperature labyrinth seals by means of systematic parameter studies. The purposes are to reveal the impacts of various operating conditions on the seal behaviors in the presence of FSI effects and to provide guidelines on the choice among different FSI models and traditional CFD models.

Table 1.3: Industrial cases using numerical simulations of FSI

(a) Partitioned approaches

Research group	application field	mechanical /thermal	one–way /two–way	explicit /implicit	steady /transient	mesh de- formation	subject of interest
Benra&Dohmen (2007) [68]	pump impeller	mech.	two–way	explicit	trn.	yes	both
Diwakar&Lin (2007) [69]	pipe network	both	one–way	–	trn.	no	structure
Gorla et al. (2002, 2005) [70, 71]	turbine blade	both	one–way	–	steady	no	structure
Ito et al. (2008) [72]	sloshing inside tanks	mech.	one–way	–	trn.	no	structure
Kuntz&Menter (2004) [73]	aeronautics	mech.	two–way	explicit	trn.	yes	both
Pericevic et al. (2005) [74, 75]	blood vessel	mech.	one–way	–	trn.	no	structure
Timperi et al. (2008) [76]	nuclear reactor	mech.	two–way	explicit	trn.	yes	structure
Zhang (2007) [77]	wing flutter	mech.	two–way	implicit	trn.	yes	structure

(b) Monolithic approaches

Research group	application field	mechanical /thermal	general purpose	method	steady /transient	mesh de- formation	subject of interest
Sigrist&Broc (2007, 2009) [66, 67]	nuclear reactor	mech.	no	FEM	modal analysis	no	structure
Tezduyar et al. (2007) [78]	spacecraft parachute	mech.	yes	FEM	trn.	yes	both
Wang et al. (2008) [65]	offshore engineering	mech.	no	hybrid FEM–BEM	modal analysis	no	structure

1.5   Organization of the Thesis

The thesis is organized in the following way:

Chapter 1 gives an overview of the roles and challenges of labyrinth seals in modern jet engines and reviews literature works on labyrinth seals, numerical methods of FSI and their industrial applications.

Chapter 2 lays out the theoretical dimensions of the study. It begins by introducing the basic concepts in the design of labyrinth seals, then moves on to the fundamentals of computational mechanics and the numerical methods of FSI.

Chapter 3 introduces the numerical tools for the study. The main features of the fluid solver, the structural solver, and the built–in coupling interface are briefly described. Last, it compares several popular commercial FSI approaches.

Chapter 4 first studies and verifies the FSI approach against the numerical FSI benchmark, then examines the parallel performance of the approach.

Chapter 5 solves the fluid force induced vibration problem. It begins with the setup and verification of the numerical models, then goes on to the detailed flow features and structural modal analysis. Finally, results of the mechanical FSI are presented, including dependency studies of the initial condition, as well as influences of pressure ratio and mass flow on the rotor amplitude.

Chapter 6 investigates the centrifugal and thermal effects. It first defines and validates the fluid and the solid models. Then, various FSI approaches are established, followed by systematical comparisons of FSI and CFD models. Last, the heat transfer behavior on the fluid–rotor/stator interfaces is presented.

Finally, key learnings from this study are concluded in chapter 7.

Chapter 2

Fundamentals

This chapter briefly reviews the basic concepts in the design of labyrinth seals, fundamentals of Computational Fluid Dynamics (CFD) and Computational Solid Mechanics (CSM) with emphasis on the current work, and numerical methods of FSI.

2.1 Essentials of Labyrinth Seals

Labyrinth seals are classic non–contacting seals in turbomachinery, such as compressors, turbines, and pumps. They meet the sealing requirement, while certain leakage is allowed. This work focuses on the labyrinth seals in jet engines with gas as the working fluid.

Figure 2.1 shows the typical seal configurations in jet engines. Many alternatives can be found in the literature [79]. They are chosen according to the leakage requirement, operating conditions, manufacturing capabilities, etc.. Both straight–through and stepped labyrinth seals are often mounted with abradable honeycomb structures, which allow for further reduction of the radial tip clearance and thus decrease in leakage. Once the teeth and the honeycomb come into contact, the thin wall honeycomb structure will be easily grooved with less collision and less damage to the teeth compared to massive walls.

(a) Straight–through   (b) Stepped   (c) With honeycomb
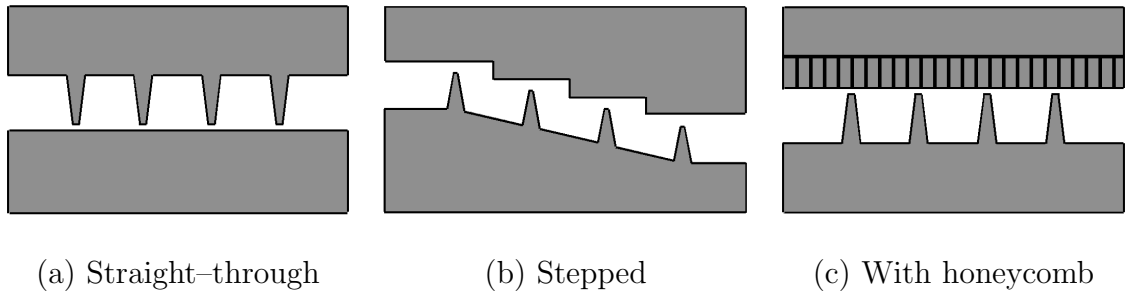
Figure 2.1: Various configurations of labyrinth seals

The thermodynamic behavior of labyrinth seals can be understood by examining the flow through the annular orifices and cavities. Driven by the pressure drop, the compressible gas is accelerated through the narrow tooth tip, which can be described as an approximately isentropic process. Subsequently, the flow enters the cavity and expands, as the velocity increases and the static pressure and temperature decrease. In the cavity, the flow expands further and dissipates in small eddies. This process is isobaric in ideal cases, so that the kinetic energy turns into thermal energy [5]. From a global point of view, the cavity pressure drops and the tip velocity rises from the inlet to the outlet. In non–rotating labyrinth seals, the total enthalpy is constant across the seal, while the entropy grows. In comparison, the total enthalpy increases in rotating labyrinth seals by receiving work from the rotor. In other words, the power loss of the rotor is transformed into flow frictions, which accelerate and heat the fluid. The reduction of leakage is achieved by the vortices built in the cavities, as the energy contained in the flow is dissipated.

In general, investigations of labyrinth seals seek to determine the relation between seal layout/operating conditions and seal performances. Labyrinth seals are often studied using rotordynamic models, which focus on the bending vibration of the rotor excited by the fluid forces. The vibration is described by linear differential equations of motion, the coefficients of which are determined using fluid forces obtained in experiments or numerical simulations. In addition to rotordynamic models, various half–empirical correlations are commonly used to predict seal performances, for example, the Knife–To–Knife (KTK) models, where leakage, swirl, etc. can be predicted based on the input of seal geometries and operating conditions. The following parameters are commonly used in the literature to describe the primary characteristics of labyrinth seals and are adopted in this study.

There are several parameters related to the leakage behavior. The corresponding dimensionless number, discharge coefficient C_D, is given by

$$C_D = \frac{\dot{m}}{\dot{m}_{ideal}} \tag{2.1}$$

$$\dot{m}_{id} = \frac{\dot{Q}_{id}\, p_{tot,in}\, A}{\sqrt{T_{tot,in}}}$$

$$\dot{Q}_{id} = \sqrt{\frac{2\kappa}{\Re(\kappa-1)}\left[1-\left(\frac{1}{\pi}\right)^{\frac{\kappa-1}{\kappa}}\right]}\left(\frac{1}{\pi}\right)^{\frac{1}{\kappa}}$$

where $\dot{m}$ denotes mass flow, the ideal mass flow $\dot{m}_{id}$ is derived from the non–choked isentropic flow of ideal gases through an annular, A is the cross–sectional area over the tooth tips, $p_{tot,in}$ and $T_{tot,in}$ designate the inlet total pressure and temperature, respectively, and the expansion function $\dot{Q}_{id}$ is defined by the pressure ratio π, ratio of specific heats κ, and specific gas constant $\Re$. The flow factor, φ, is also commonly

used to represent the leakage rate

$$\varphi = \frac{\dot{m}\sqrt{T_{tot,in}}}{2R\,p_{tot,in}} \tag{2.2}$$

with the radius R. Choked flow occurs when C_D or φ remains constant regardless of a further increase in $p_{tot,in}$.

The effect of total temperature increase due to internal losses is called windage heating and is measured by the dimensionless number, windage heating coefficient σ

$$\sigma = \frac{c_p\,\Delta T_{tot}}{\omega^2 R^2} \tag{2.3}$$

where ΔT_{tot} is taken as the difference of the average total temperature between the inlet and the outlet, ω is the rotational speed, and c_p is the fluid specific heat capacity at constant pressure.

The swirl development across the seal is defined by the outlet swirl ratio K_{out}

$$K_{out} = \frac{v_{tan}}{\omega R} \tag{2.4}$$

with the average circumferential velocity at the outlet v_{tan}.

In heat transfer analyses, the Nusselt number Nu and heat transfer coefficient *htc* represent the ratio of convective to conductive heat transfer across the fluid–solid boundary

$$htc = \frac{\dot{Q}}{A(T_f - T_s)}, \quad \overline{htc} = \frac{\dot{Q}_{sum}}{A_{sum}(\overline{T_f} - \overline{T_s})} \tag{2.5}$$

$$\mathrm{Nu} = \frac{htc\,L}{\lambda_f}, \quad \overline{\mathrm{Nu}} = \frac{\overline{htc}\,L}{\lambda_f} \tag{2.6}$$

where $\dot{Q}$ represents the heat flow, A is the fluid–solid area, the length L equals twice the tip clearance, and λ_f denotes the fluid thermal conductivity. Moreover, the fluid temperature T_f is usually estimated by averaging the total temperatures over the channel height, while the solid temperature T_s is taken at the fluid–solid surface. In the expression of $\overline{htc}$, $\overline{T_f}$ and $\overline{T_s}$ are calculated by averaging T_f and T_s across the seal.

Various operating conditions are written as dimensionless numbers as well. The pressure ratio π and the circumferential Mach number M_{tan} are defined as

$$\pi = \frac{p_{tot,in}}{p_{stat,out}} \tag{2.7}$$

$$M_{tan} = \frac{\omega R}{c} \tag{2.8}$$

with the outlet static pressure $p_{stat,out}$ and the speed of sound c.

2.2   Computational Fluid Dynamics

This section gives a brief review of the governing equations of fluid mechanics, turbulence modeling, and the finite volume method (FVM) for CFD [80–84].

2.2.1   Governing Equations of Fluid

The governing equations of fluid mechanics include the conservation laws for mass, momentum, and energy, which are usually expressed using the Eulerian description. Mechanical and thermodynamic constitutive equations are needed to close the system of equations. The momentum conservation law for Newtonian fluids is also known as the Navier–Stokes equations, where the stress tensor $\mathbf{T}$ is given by

$$\mathbf{T} = -\left(p + \frac{2}{3}\mu\nabla\cdot\mathbf{v}\right)\mathbf{I} + 2\mu\mathbf{D} \tag{2.9}$$

where μ denotes the dynamic viscosity, $\mathbf{v}$ represents the velocity, $\mathbf{I}$ is the identity tensor, and $\mathbf{D}$ is the strain rate tensor

$$\mathbf{D} = \frac{1}{2}\left[\nabla\mathbf{v} + (\nabla\mathbf{v})^{\mathrm{T}}\right] \tag{2.10}$$

In the Navier–Stokes equations, the symmetric stress tensor $\mathbf{T}$ is often decomposed into a volumetric stress tensor $(-p\mathbf{I})$ representing the isotropic hydrostatic pressure, and a deviatoric stress tensor $\boldsymbol{\tau}$ which describes the anisotropic viscous forces

$$\boldsymbol{\tau} = 2\mu\mathbf{D} - \frac{2}{3}\mu(\nabla\cdot\mathbf{v})\mathbf{I} \tag{2.11}$$

The unsteady equations of mass, momentum, and energy conservation are given in Eq. 2.12 to Eq. 2.14 with the density ρ, body force per unit mass $\mathbf{b}$, thermal conductivity λ, and energy source S_E. The energy conservation law is expressed in the form of total enthalpy h_{tot} to describe compressible flows. Static quantities are indicated in the following unless otherwise stated.

$$\frac{\partial\rho}{\partial t} + \nabla\cdot(\rho\mathbf{v}) = 0 \tag{2.12}$$

$$\frac{\partial(\rho\mathbf{v})}{\partial t} + \nabla\cdot(\rho\mathbf{v}\mathbf{v}) = -\nabla p + \nabla\cdot\boldsymbol{\tau} + \rho\mathbf{b} \tag{2.13}$$

$$\frac{\partial(\rho h_{tot})}{\partial t} - \frac{\partial p}{\partial t} + \nabla\cdot(\rho\mathbf{v}h_{tot}) = \nabla\cdot(\lambda\nabla T) + \nabla\cdot(\mathbf{v}\cdot\boldsymbol{\tau}) + \mathbf{v}\cdot\rho\mathbf{b} + S_E \tag{2.14}$$

The system of equations above is to be solved for $\mathbf{v}$, p, and h_{tot}. Static enthalpy h is calculated by $h = h_{tot} - (\mathbf{v}\cdot\mathbf{v})/2$. Then, static temperature T can be computed using the caloric constitutive relation of $h = h(p, T)$, which becomes $dh = c_p(T)dT$

for ideal gas. At the mean time, total temperature T_{tot} is calculated from h_{tot} using the similar relation, $dh_{tot} = c_p(T)dT_{tot}$. In addition, total pressure p_{tot} of ideal gas is evaluated with

$$p_{tot} = p \exp\left[\frac{1}{\Re} \int_T^{T_{tot}} \frac{c_p(T)}{T} dT\right] \tag{2.15}$$

The thermal equation of state is required to determine the density. For an ideal gas, this relationship is described by the ideal gas law

$$\rho = p/\Re T \tag{2.16}$$

2.2.2 Statistical Turbulence Models

By decomposing the fluid variables into averaged and fluctuating components, for example, velocity $\mathbf{v} = \overline{\mathbf{v}} + \mathbf{v}'$, the original Navier–Stokes equations are modified, resulting in the Reynolds Averaged Navier–Stokes (RANS) equations. The momentum and enthalpy transport equations thus contain turbulent flux terms adding to the molecular diffusive terms. These additional turbulent fluxes are called Reynolds stress $\rho \overline{\mathbf{v}' \mathbf{v}'}$ and Reynolds flux $\rho \overline{\mathbf{v}' h'}$, respectively. Turbulence models based on the RANS equations are known as statistical turbulence models due to the statistical averaging procedure. The equations used to model the Reynolds stresses and Reynolds fluxes define the type of turbulence model.

Eddy viscosity turbulence models are used in the current work. The eddy viscosity hypothesis assumes that the Reynolds stresses can be related to the mean flow and turbulent viscosity μ_t in a manner analogous to $\boldsymbol{\tau}$ in laminar flows. In other words, the turbulent effect can be represented as an increased viscosity with the effective viscosity $\mu_{eff} = \mu + \mu_t$. The Reynolds stresses and the Reynolds averaged momentum equations for incompressible flows become:

$$-\rho \overline{\mathbf{v}' \mathbf{v}'} = \mu_t \left[\nabla \overline{\mathbf{v}} + (\nabla \overline{\mathbf{v}})^{\mathrm{T}}\right] - \frac{2}{3}\rho k \mathbf{I} \tag{2.17}$$

$$\frac{\partial(\rho \overline{\mathbf{v}})}{\partial t} + \nabla \cdot (\rho \overline{\mathbf{v}}\,\overline{\mathbf{v}}) = -\nabla(\overline{p} + \frac{2}{3}\rho k) + \nabla \cdot \left[\mu_{eff}\nabla \overline{\mathbf{v}} + \mu_{eff}(\nabla \overline{\mathbf{v}})^{\mathrm{T}}\right] + \rho \mathbf{b} \tag{2.18}$$

with the turbulent kinetic energy k given by $k = \frac{1}{2}\overline{\mathbf{v}' \cdot \mathbf{v}'}$, the averaged pressure $\overline{p}$, and the averaged velocity $\overline{\mathbf{v}}$. For compressible flows, the averaging is weighted by density, and the $-\frac{2}{3}\mu(\nabla \cdot \overline{\mathbf{v}})\mathbf{I}$ term of $\overline{\boldsymbol{\tau}}$ is neglected by the current CFD solver which will be introduced in the next chapter.

In order to close the averaging system, μ_t has to be modeled by additional equations. This can be done by the $k-\varepsilon$, $k-\omega$, or SST turbulence models. Both the $k-\varepsilon$ and $k-\omega$ turbulence models provide two additional transport equations to compute μ_t. In the former, k and the dissipation rate of the turbulent kinetic energy, ε, are

introduced and calculated directly from the respective transport equations, while μ_t is assumed to be linked to k and ε via $\mu_t = C_\mu \rho \frac{k^2}{\varepsilon}$. The latter solves transport equations for k and the turbulent frequency ω, to which μ_t is related via $\mu_t = \rho \frac{k}{\omega}$. The SST turbulence model is a combination of $k - \omega$ model in the inner boundary layer and $k - \varepsilon$ in the outer region of the boundary layer and the main flow. Moreover, a limitation of the shear stress in adverse pressure gradient regions is implemented in the SST model. Formulations of the k and ω transport equations and the limiter are given in [85].

In high–Re models, wall functions are often used, which relate the near–wall tangential velocity to the wall shear stress τ_w by a logarithmic relation and use τ_w as a force boundary condition for the momentum equation of the tangential velocity component. Using wall functions can save the computing time substantially. It means that the first node is located in the log–law region where $30 \leq y^+ \leq 300$ and the viscous sublayer is not resolved. Wall functions are derived under the assumption that the flow between the first node and the wall behaves as in the flat–plate boundary layer flow. However, this is not satisfied in many cases. In low–Re models, details of the boundary layer are obtained by solving the adapted transport equations through the sublayer, requiring the first node to be located at $y^+ \approx 1$ and 5 – 10 nodes up to $y^+ \approx 20$ [86].

2.2.3   Finite Volume Method

The governing equations of fluids are usually discretized in space using FVM. The FVM formulations can be found in many literatures and are not repeated in this section. Instead, general remarks on FVM with respect to the current study are summarized as follows.

The spatial domain is discretized into control volumes (CV) and the differential governing equations are integrated over each CV. Then, the variables and their derivatives are evaluated by numerical approximation. Diffusive terms are often approximated using a central differencing method, while convective terms can be discretized using various schemes with pros and cons. The first–order accurate Upwind Differencing Scheme (UDS) is robust; however, diffusive discretization errors are introduced. The second–order accurate Central Differencing Scheme (CDS) is less robust and tends to cause nonphysical oscillations in regions of rapid solution variations. This represents the common dilemma of numerical approximations: high–order approximations are generally less robust in addition to increasing the computational load.

The unsteady terms can be discretized using explicit/implicit transient schemes of different order–accuracy. For example, the second–order Backward–Differencing Formula (BDF) employed in this work has the advantages of being robust, fully implicit, conservative in time, unconditionally stable, and second–order accurate in time. However, it is not bounded and may create nonphysical solution oscillations.

In comparison, its first–order counterpart is bounded, but will introduce diffusive discretization errors similar to the behavior of UDS in space.

When the CVs deform in time, the integral conservation equations must be modified by applying the Leibniz integral rule and the Space Conservation Law (SCL) must be satisfied. The SCL states that for each CV, the rate of change of volume must equal the swept volume due to the its boundary motions [87]. It is satisfied by using consistent formulations for both the control volume and swept volume calculations.

There are mainly two solution strategies for the coupled system of discretized conservation equations: the segregated and the coupled treatments. The latter exceeds the former in robustness and generality, while the former has the advantage of lower storage requirement. A well–known example of the segregated algorithm is the SIMPLE pressure–correction method. In comparison, the coupled approach solves the equations of mass and momentum conservation as a single system.

The procedures above lead to systems of algebraic equations, which are solved using iterative methods, such as the ILU methods. They start from an approximate solution and repeatedly improve it by a correction to yield a better solution of the desired accuracy. Furthermore, iterative methods can be accelerated significantly using multigrid methods, which deliver constant computing time per node as the grid is refined [88].

Last but not least, one major issue in industrial applications of CFD concerns the reliability of the results. In order to improve the quality of CFD simulations, a large number of Best Practice Guidelines (BPG) have been proposed by various groups [89, 90] to provide generic advices on how to perform high–quality CFD computations. BPGs give valuable input to the current study on avoiding common errors, generating appropriate meshes, choosing turbulence models, etc..

2.3 Computational Solid Mechanics

This section reviews the basic physical quantities and governing equations for thermoelastic material with geometric nonlinearities, as well as the key procedure of finite element discretization [91–95].

2.3.1 Governing Equations of Solid

The Eulerian (spatial) coordinates of a body are denoted by $\mathbf{x}$, and the Lagrangian (material) coordinates by $\mathbf{X}$. The Lagrangian description is most popular in solid mechanics, then the displacement is calculated by $\mathbf{u}(\mathbf{X}, t) = \mathbf{x}(\mathbf{X}, t) - \mathbf{X}$. There are mainly two formulations based on the Lagrangian description: the total Lagrangian formulation and the updated Lagrangian formulation. The derivatives and integrals are taken with respect to the initial configuration $\mathbf{X}$ in the former, and the current

configuration $\mathbf{x}$ in the latter. Moreover, the former usually uses total measures of stress and strain, and the latter often uses rate measures. The two formulations are identical regarding the underlying mechanics. The updated Lagrangian formulation can be transformed to the total Lagrangian formulation by configuration mappings and tensor transformations, and vice versa. In the following, the strain and stress are expressed in both formulations, while the conservation laws only in the updated Lagrangian formulation.

In the total Lagrangian formulation, the Green strain tensor $\mathbf{E}^{el}$ is used to account for finite strains, large rotations and deflections

$$\mathbf{E}^{el} = \frac{1}{2} \left[\nabla \mathbf{u} + (\nabla \mathbf{u})^{\mathrm{T}} + \nabla \mathbf{u} \cdot (\nabla \mathbf{u})^{\mathrm{T}} \right] \tag{2.19}$$

with $\nabla = \partial/\partial \mathbf{X}$, while the Cauchy strain tensor $\boldsymbol{\varepsilon}^{el}$ omits the nonlinear term in $\mathbf{E}^{el}$ and accounts for infinitesimal strains

$$\boldsymbol{\varepsilon}^{el} = \frac{1}{2} \left[\nabla \mathbf{u} + (\nabla \mathbf{u})^{\mathrm{T}} \right] \tag{2.20}$$

with $\nabla = \partial/\partial \mathbf{X} \approx \partial/\partial \mathbf{x}$. Note that $\boldsymbol{\varepsilon}^{el}$ only applies to small deflections and rotations, as it does not vanish in large rigid body rotations.

In the updated Lagrangian formulation, strains are measured by the strain rate tensor $\mathbf{D}^{el}$ using velocity $\mathbf{v}$ as the independent variable

$$\mathbf{D}^{el} = \frac{1}{2} \left[\nabla \mathbf{v} + (\nabla \mathbf{v})^{\mathrm{T}} \right] \tag{2.21}$$

with $\nabla = \partial/\partial \mathbf{x}$. $\mathbf{v}$ is originally defined in Lagrangian coordinates and can be expressed in terms of Eulerian coordinates by using element coordinates.

The thermal strain tensor $\boldsymbol{\varepsilon}^{th}$ takes a diagonal form and becomes a volumetric tensor for isotropic material

$$\boldsymbol{\varepsilon}^{th} = \int_{T_0}^{T} \alpha(T) dT \, \mathbf{I} \tag{2.22}$$

with the temperature–dependent coefficient of thermal expansion $\alpha(T)$ and the initial temperature T_0. The thermal strain is often defined as either the logarithmic strain or the nominal strain. When α is assumed constant, the final thermal expansion becomes

$$\mathbf{l}^{log} = \mathbf{l}_0 \exp[\alpha(T - T_0)], \quad \mathbf{l}^{nom} = \mathbf{l}_0 [1 + \alpha(T - T_0)] \tag{2.23}$$

The second Piola–Kirchhoff stress tensor $\mathbf{S}^{el}$ is conjugate in power to the Green strain rate $\dot{\mathbf{E}}^{el}$, while the Cauchy stress tensor $\boldsymbol{\sigma}^{el}$ and $\mathbf{D}^{el}$ are conjugate in power. $\boldsymbol{\sigma}^{el}$ is also called the physical stress or true stress. In constitutive laws, the Jaumann

objective stress rate should be used instead of the rate of the Cauchy stress $\dot{\boldsymbol{\sigma}}^{el}$ to account for large rotations, whereas $\mathbf{S}^{el}$ is used directly, since it is invariant in pure rotation. Thus, the Cauchy stress rate and the second PK stress become

$$\dot{\boldsymbol{\sigma}}^{el} = \mathbf{C}^{JD} : \mathbf{D}^{el} + \mathbf{W} \cdot \boldsymbol{\sigma}^{el} + \boldsymbol{\sigma}^{el} \cdot \mathbf{W}^{\mathrm{T}} \tag{2.24}$$

$$\mathbf{S}^{el} = \mathbf{C}^{SE} : \mathbf{E}^{el} \tag{2.25}$$

where the fourth–order elasticity tensor $\mathbf{C}^{JD}$ links the Jaumann objective rate to $\mathbf{D}^{el}$, $\mathbf{C}^{SE}$ relates $\mathbf{S}^{el}$ to $\mathbf{E}^{el}$, and the spin tensor $\mathbf{W}$ is defined as $\mathbf{W} = \frac{1}{2} \left[(\nabla \mathbf{v})^{\mathrm{T}} - \nabla \mathbf{v} \right]$.

For elastic material in the small strain regime, there is no distinction between the various measures of strain and stress. Thus, the constitutive law of isotropic elasticity can be expressed by the Young's modulus E and Poisson's ratio ν

$$\boldsymbol{\sigma}^{el} = \frac{E}{1+\nu} \boldsymbol{\varepsilon}^{el} + \frac{\nu E}{(1+\nu)(1-2\nu)} \varepsilon_{kk}^{el} \mathbf{I} \tag{2.26}$$

The linear elastic law can be extended to account for small strain with large rotation by substituting $\boldsymbol{\sigma}^{el}$ and $\boldsymbol{\varepsilon}^{el}$ with $\mathbf{S}^{el}$ and $\mathbf{E}^{el}$, respectively, which is called the Saint–Venant–Kirchhoff model. The isotropic Saint–Venant–Kirchhoff material law becomes

$$\mathbf{S}^{el} = \frac{E}{1+\nu} \mathbf{E}^{el} + \frac{\nu E}{(1+\nu)(1-2\nu)} E_{kk}^{el} \mathbf{I} \tag{2.27}$$

The thermal stress $\boldsymbol{\sigma}^{th}$ of isotropic linear thermoelastic material with constant α is given by

$$\boldsymbol{\sigma}^{th} = -\frac{\alpha E}{1-2\nu} (T - T_0) \mathbf{I} \tag{2.28}$$

The governing equations arise from the fundamental conservation laws of continuum mechanics. The conservation of momentum is expressed as the equation of motion, and the conservation of energy describes heat transfer. In the updated Lagrangian formulation, the conservation equations are expressed by $\boldsymbol{\sigma}$ and $\mathbf{D}$; the variables are written in terms of the Lagrangian coordinates, such as $\mathbf{v}(\mathbf{X}, t)$, but the derivatives are with respect to the Eulerian coordinates

$$\rho \dot{\mathbf{v}} = \nabla \cdot \boldsymbol{\sigma} + \rho \mathbf{b} \tag{2.29}$$

$$\rho \, \dot{e} = \boldsymbol{\sigma} : \mathbf{D} - \nabla \cdot \mathbf{q} + \rho \, \psi \tag{2.30}$$

with $\nabla = \partial / \partial \mathbf{x}$, body force per unit mass $\mathbf{b}$, internal energy per unit mass $e = c_s T$, heat flux $\mathbf{q} = -\lambda \nabla T$ for isotropic material, and heat source per unit mass ψ.

2.3.2   Finite Element Method

The finite element method (FEM) discretizes the weak form of the momentum and energy equations to obtain approximate solutions to the strong form. The weak form can be obtained either by applying the weighted–residual Galerkin method to the strong form or by differentiating the virtual work of the system. The finite element discretization of displacement and velocity vectors is written as

$$\{\mathbf{u}(\mathbf{X}, t)\} = [\mathbf{N}(\mathbf{X})]\{\mathbf{a}(t)\}, \quad \{\mathbf{v}(\mathbf{X}, t)\} = [\mathbf{N}(\mathbf{X})]\{\dot{\mathbf{a}}(t)\} \tag{2.31}$$

with the unknown nodal displacement vector $\{\mathbf{a}\}$ and the shape function matrix $[\mathbf{N}]$, thereby, the spatial dependence and the time dependence are separated.

We shall focus on the momentum equation. Its weak form is first discretized in space, resulting in the semi–discrete equations

$$[\mathbf{M}]\{\ddot{\mathbf{a}}\} + \{\mathbf{f}^{int}\} = \{\mathbf{f}^{ext}\} \tag{2.32}$$

In the updated Lagrangian formulation, the mass matrix reads $[\mathbf{M}] = \int_\Omega \rho[\mathbf{N}]^{\mathrm{T}}[\mathbf{N}]d\Omega$; the internal nodal force is written as $\{\mathbf{f}^{int}\} = \int_\Omega [\partial\mathbf{N}/\partial\mathbf{x}]^{\mathrm{T}}\{\boldsymbol{\sigma}\}d\Omega$, where the Cauchy stress tensor is converted to a vector in Voigt notation; and the external nodal force becomes $\{\mathbf{f}^{ext}\} = \int_\Omega \rho[\mathbf{N}]^{\mathrm{T}}\{\mathbf{b}\}d\Omega + \int_\Gamma \rho[\mathbf{N}]^{\mathrm{T}}\{\mathbf{t}\}d\Gamma$ with the normal surface force vector $\{\mathbf{t}\}$. The total Lagrangian formulation would also result in Eq. 2.32, except that the derivatives and integrals are taken over the initial coordinates.

The most popular and most robust method of solving Eq. 2.32 is the Newton–Raphson method. It first linearizes the term $\{\mathbf{f}^{int}\}$ by differentiating it with respect to $\{\mathbf{a}\}$, yielding the tangent stiffness matrix $[\mathbf{K}(\mathbf{a})] = \partial\{\mathbf{f}^{int}\}/\partial\{\mathbf{a}\}$, and then solves the equations iteratively. In linear cases, $[\mathbf{K}]$ is independent of $\{\mathbf{a}\}$.

Equations 2.32 need to be further discretized with respect to time, where various time integration methods can be applied. The Newmark–β time marching scheme is an implicit method that uses finite difference expansions in time to calculate $\{\mathbf{a}_{n+1}\}$ based on $\{\mathbf{a}_n\}$

$$\{\ddot{\mathbf{a}}_{n+1}\} = \{\dot{\mathbf{a}}_n\} + [(1 - \gamma)\{\ddot{\mathbf{a}}_n\} + \gamma\{\ddot{\mathbf{a}}_{n+1}\}]\,\Delta t \tag{2.33}$$

$$\{\mathbf{a}_{n+1}\} = \{\mathbf{a}_n\} + \{\dot{\mathbf{a}}_n\}\Delta t + \left[\left(\frac{1}{2} - \beta\right)\{\ddot{\mathbf{a}}_n\} + \beta\{\ddot{\mathbf{a}}_{n+1}\}\right]\Delta t^2 \tag{2.34}$$

where β and γ are integration parameters. The solution of Eq. 2.33 and Eq. 2.34 is unconditionally stable when $\beta \geq \frac{1}{4}\left(\frac{1}{2} + \gamma\right)^2$, $\gamma \geq \frac{1}{2}$. The parameters are sometimes calculated using the amplitude decay factor θ as $\beta = \frac{1}{4}(1 + \theta)^2$, $\gamma = \frac{1}{2} + \theta$. When $\beta = 1/4$ and $\gamma = 1/2$, i.e. $\theta = 0$, the results will not show any numerical damping. However, a certain level of numerical damping is usually desired and is achieved by setting $\theta > 0$.

2.4 Numerical Methods of FSI

In generic fluid–structure coupling problems, the mechanical and/or thermal quantities of the two fields are exchanged at the interface. In particular, the fluid passes forces and heat flow to the solid, while the solid sends displacements and temperatures back to the fluid.

The following mechanical and thermal boundary conditions must be satisfied on the fluid–solid interface

$$\mathbf{T} \cdot \mathbf{n}_f = -\boldsymbol{\sigma} \cdot \mathbf{n}_s, \quad \mathbf{v}_f = \mathbf{v}_s \tag{2.35}$$

$$\mathbf{q}_f = \mathbf{q}_s, \quad T_f = T_s \tag{2.36}$$

where $\boldsymbol{\sigma}/\mathbf{T}$ denote the solid/fluid stress, $\mathbf{q}$ designates the heat flux, and $\mathbf{n}$ is the unit normal vector of the interface. They imply the force balance, no–slip wall conditions for the fluid, heat flux balance, and temperature balance, respectively.

Various FSI solution strategies have been compared in section 1.3.1. An implicit partitioned approach for two–way coupling is chosen for this work, the algorithm of which is shown in Fig. 2.2. The FSI iteration is also known as the stagger iteration, and its definition is introduced in the next chapter. In each FSI iteration, the solid solver runs first, where the solid boundary conditions are updated by the fluid results obtained from the last FSI iteration; then the fluid solver runs based on the fluid boundary conditions updated by the solid solution.

The fluid mesh deforms with time in FSI problems, thus the fluid integral conservation equations need to be modified by applying the Leibniz rule. Such modification can also be interpreted as describing the conservation laws in the arbitrary Lagrangian–Euler formulation. As a result, the convective terms are corrected to account for the net convection across the moving CV boundary S, and the unsteady terms are with respect to the moving volume V

$$\frac{d}{dt} \int_V \rho \, dV + \int_S \rho (\mathbf{v} - \mathbf{v}^g) \cdot \mathbf{n} \, dS = 0 \tag{2.37}$$

$$\frac{d}{dt} \int_V \rho \mathbf{v} \, dV + \int_S \rho \mathbf{v} (\mathbf{v} - \mathbf{v}^g) \cdot \mathbf{n} \, dS = \int_S (-p\mathbf{I} + \boldsymbol{\tau}) \cdot \mathbf{n} \, dS + \int_V \rho \mathbf{b} \, dV \tag{2.38}$$

$$\frac{d}{dt} \int_V \rho \phi \, dV + \int_S \rho \phi (\mathbf{v} - \mathbf{v}^g) \cdot \mathbf{n} \, dS = \int_S \lambda_\phi \nabla \phi \cdot \mathbf{n} \, dS + \int_V S_\phi \, dV \tag{2.39}$$

where $\mathbf{v}^g$ is the velocity of the CV boundary, and the energy equation is represented by the generic transport equation of scalar ϕ with its diffusivity λ_ϕ and energy source S_E for conciseness. Moreover, the space conservations law

$$\frac{d}{dt} \int_V dV = \int_S \mathbf{v}^g \cdot \mathbf{n} \, dS \tag{2.40}$$
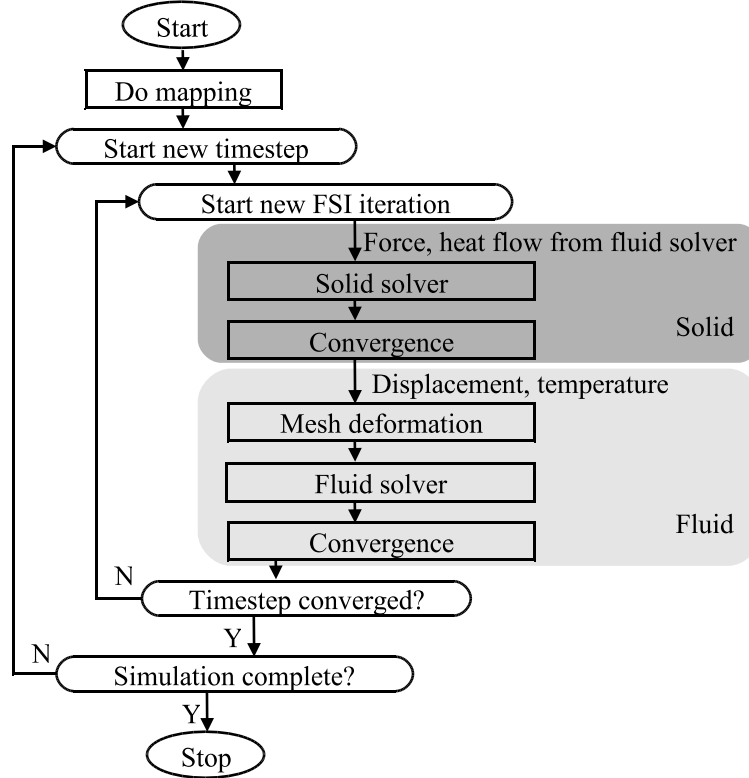
Figure 2.2: Implicit partitioned approach for two–way coupling; solid solver first

must be enforced to avoid erroneous sources of conserved quantities [87]. The equation indicates that the rate of the volume change must equal the net volume swept by the moving CV faces.

FSI simulations can either be transient or steady. Both the fluid and the solid solvers can be set to transient or steady mode, giving rise to four different combinations. The transient–transient combination models transient physics, such as the structural vibration induced by fluid forces. In the steady–steady case, the physical process moves towards an equilibrium. This approach is adequate for the steady–state heat transfer between fluid and solid. The steady solid–transient fluid version simulates transient FSI effects where the structural response to the flow variations is much faster than the evolvement of the fluid field, such that the transient effects of the solid can be neglected. Reversing the case will lead to the transient solid–steady fluid combination. Actually, all FSI effects can be solved with the transient–transient approach, but the results would be the same with the respective semi–steady or steady approaches, and the computational cost would be much higher.

Chapter 3

FSI Solutions

The ANSYS® multiphysics software package is adopted in this work, and it requires no third–party interface to couple the algebraic multigrid CFD solver ANSYS CFX® and the FEM based structural solver ANSYS Mechanical™. The particular two–way implicit FSI solver is referred to as MFX and its related information can be found in the ANSYS manuals [89, 91].

This chapter starts with introducing the main features of the fluid solver, as well as the capabilities of the structural solver. Then, it goes through detailed parameter settings of the built–in coupling interface. Finally, a brief comparison is given among several prevailing commercial FSI approaches.

3.1   CFD Code

ANSYS CFX is a general purpose CFD software capable of modeling transient turbulent flows with heat transfer. The main features are as follows:

Finite volume method: The governing equations are discretized by applying the finite volume method as described in section 2.2.3.

Unstructured grid: The code uses a non–staggered unstructured grid.

Coupled solver: The coupled solver solves for velocity and pressure simultaneously, in contrast to the pressure–correction methods.

Algebraic multigrid: The linear equations are solved iteratively using an algebraic multigrid accelerated Incomplete Lower Upper (ILU) factorization technique. In particular, the additive correction implementation of algebraic multigrid is used.

Parallel computation: A parallel computation consists of two steps: a partitioning step and a running step. Several node–based partitioners are available, most of

which employ recursive bisection methods. The Multilevel Graph Partitioning
Software partitioner, MeTiS, is very common due to its high efficiency. The
parallel communication is performed using the Parallel Virtual Machine (PVM)
or the Message Passing Interface (MPI).

In addition, there are other features of the CFD code which are indispensable in the
current work and will be referred to occasionally in later chapters, such as:

Reference pressure: The relative pressures at boundaries and a global reference
pressure can be specified by the user. The main purpose of using a reference
pressure in translation between the absolute and relative pressure is to avoid
round–off error problems when the pressure change is much smaller than the
absolute pressure. For compressible flows, the pressure level set by the reference
pressure affects the results. Therefore, the absolute pressure is referred to in
this thesis unless otherwise stated.

Boundary conditions: The inlet and outlet boundaries can be set in terms of ve-
locity, static/total pressure, or mass flow. In $k-\varepsilon$ and $k-\omega$ turbulence models,
the inlet turbulence quantities are specified, such as turbulence intensity and
length scale, while a constant gradient constraint is imposed at the outlet. When
heat transfer is involved, it requires the inlet static/total temperature or total
enthalpy. Moreover, a translational or rotational speed can be specified for wall
boundaries.

Steady simulation: The solver applies a false timestep to under–relax the equa-
tions for steady problems. There are two iteration levels: the outer (false)
timestep iteration and the inner coefficient iteration. For steady state, each
outer iteration contains only one inner iteration.

Transient simulation: First/second–order implicit schemes are applied to transient
simulations. In contrast to steady cases, multiple inner iterations are performed
at each timestep. In addition, there is another iteration level between the outer
and the inner iterations in transient two–way FSI analysis, which is called the
stagger iteration. Each timestep consists of one or more stagger iterations;
within a stagger iteration, each field solver runs once for multiple inner itera-
tions.

Convection term: Available convection schemes are as follows: 1) First–order Up-
wind Differencing Scheme (UDS); 2) Central Difference Scheme (CDS); 3) Blend-
ing scheme between UDS and CDS; 4) *High resolution scheme*, which is actually
second–order bounded UDS.

Turbulence models: The flow solver provides various turbulence models: RANS
models (including eddy viscosity models and Reynolds stress models), Large

Eddy Simulation (LES) models, and RANS–LES hybrid models. For two–equation eddy viscosity models, there are the standard $k - \varepsilon$ model, RNG $k - \varepsilon$ model, standard $k - \omega$ model, Shear Stress Transport (SST) model, and so on.

The boundary layer flow can be modeled with wall functions or the low–Re near–wall approach. An alternative near–wall treatment for $k - \omega$ based models is included in the solver, which is called the *automatic wall treatment*. It allows for a smooth shift from a low–Re formulation to wall functions. Similarly, a modified wall function approach known as the *scalable wall function* is implemented for models based on the ε–equation, in order to overcome the prediction inconsistencies when refining the near–wall mesh.

Convergence criteria: The solver provides two types of residual measurements, i.e. the Root Mean Square (RMS) and the maximum (MAX) normalized residuals. The residuals are monitored for the mass/momentum/energy transport equations only, excluding the turbulent transport equations. In addition, the conservation of mass, momentum, and energy at the boundaries are also checked for convergence. The percentage imbalance of certain quantity is defined as (Total In - Total Out)/Total In. The iteration is terminated and the solution is considered converged when both the residual target and the imbalance target are met.

Mesh deformation: The displacements received by the fluid solver on domain boundaries are diffused to other mesh points inside the domain by solving the displacement diffusion equation $\nabla \cdot (\Gamma_{disp} \nabla \boldsymbol{\delta}) = \mathbf{0}$, where $\boldsymbol{\delta}$ denotes displacements relative to the previous mesh locations. The mesh diffusivity, Γ_{disp}, is also referred to as the *mesh stiffness*. It determines how stiffly the mesh deforms in different regions. The solver provides several options for calculating Γ_{disp}. For example, Γ_{disp} for *increase near boundaries* is defined as $\Gamma_{disp} = \left(\frac{1}{d}\right)^{C_{stiff}}$, where d indicates the distance from the nearest boundary. Γ_{disp} for *increase near small volumes* is defined as $\Gamma_{disp} = \left(\frac{1}{V}\right)^{C_{stiff}}$, where V refers to the control volume size. One can decide how quickly Γ_{disp} increases by specifying the exponent C_{stiff}. Alternatively, it is allowed to define other expressions for Γ_{disp}. The RMS residual is used to measure the convergence level of the mesh displacement equation. In addition, the Space Conservation Law for moving grids [87] is satisfied by the code.

3.2 CSM Code

ANSYS Mechanical is general purpose software for finite element analysis of mechanical problems. Its capabilities range from linear static to nonlinear transient analysis. The key features related to this work are presented below:

Geometric nonlinearity: The solver applies the updated Lagrangian method to simulate geometric nonlinearities. Finite displacement and rotation effects can be included in both static and transient analyses. This feature is applied in order to account for large deflections with small strains as in the case to be discussed in chapter 4 and centrifugal growths as in the case to be discussed in chapter 6.

Element types: The element library of the code consists of several element types, such as 3D first/second–order beam/solid elements with structural and thermal DOFs at each node.

Transient scheme: The Newmark–β time integration method is used for implicit transient analysis. The integration parameters can be either from direct inputs, or indirect correlations with the user–defined amplitude decay factor.

Convergence control: In nonlinear analyses, three different vector norms are used as convergence controls, which are the L^2 norm checking the square root sum of the squares of variable imbalances, the L^1 norm checking the sum of the absolute values of imbalances, and the infinite norm checking the imbalances of each DOF at each node.

Centrifugal effects: Centrifugal effects can be applied to structures with specified rotational velocities. The inertial effects are incorporated either by activating geometric nonlinearity or by subtracting a spin softening matrix from the structural stiffness matrix. This feature is only applicable to some element types.

Thermal analysis: The temperature distribution and related thermal quantities are obtained from thermal analysis. Material properties are allowed to be either constant or temperature–dependent. Thermal load types supported by the code include constant temperatures, convections, and heat fluxes. When using convective boundaries, heat transfer coefficient and surrounding fluid temperature also need to be specified. Heat flux boundary conditions are used when the amount of heat transfer across a surface is known.

3.3   FSI Interface

The implicit partitioned method for two–way FSI is adopted in the current study. According to the previous discussion in section 1.3.1, this approach has higher accuracy and is more stable than others, with which the individual physical fields can be solved more effectively and efficiently. This section focuses on the coupling between the CFD and the CSM solvers. The list below discusses coupling–related settings in FSI models.

Solution sequence: The CFD and the CSM codes can be run simultaneously or sequentially during each stagger iteration. The latter is more commonly used and requires specifications of solver orders in stagger iterations.

Coupling variables: The variables allowed transferring across the fluid–solid interface include mechanical variables, such as displacement, force, and force flux, and thermodynamic variables, such as temperature, heat flow, and heat flux.

Mapping interpolation schemes: An interpolation scheme is necessary for data mapping across mismatched meshes from the two solvers at FSI interfaces. There are two types of interpolation, which are the *profile preserving* scheme and the *conservative* scheme. The former takes the variable profile from one mesh and maps it onto the other, regardless of quantity conservations across the surface as ensured in the latter scheme. In practice, displacement and temperature are always interpolated using the former scheme, while force and heat flow always follow the latter one.

FSI convergence criteria: The convergence criteria use the L^2 norm of each variable ϕ, which is defined as $\|\phi\|_2 = \sqrt{\sum \left(\frac{\phi_{new} - \phi_{old}}{\phi_{new}} \right)^2}$. Note that the sum is taken over all nodes on the coupling surface. The variable ϕ is considered to be converged when $\|\phi\|_2$ is reduced below the convergence target.

FSI under–relaxation factors: These are the relaxation values applied to the variables transferring across the coupling surface. It is possible to specify different under–relaxation factors to different variables.

FSI timestep: In transient FSI analysis, the fluid timestep must equal the FSI timestep, while a smaller value can be used for the solid timestep. This so–called sub–cycling is sometimes required to improve stability.

3.4 Comments on Prevailing Commercial FSI Solutions

In recent years, there is a boom of commercial FSI solvers. However, it is important to realize that the solutions can vary greatly in the degree of sophistication. For example, some are capable of strongly coupled transient FSI problems, while some only perform post–processing–like FSI analysis by purely passing data from one solver to the other at the end of the simulation. In addition, partitioned approaches seem to be preferred among software suppliers, as there is no commercial monolithic approach known to the author.

ANSYS provides several FSI solutions which do not require third–party interfaces. For example, the MFX solver introduced above offers implicit solutions of two–way FSI problems [96], which is the most stable and accurate version of partitioned approaches. In contrast, another FSI capability is also available in the most recent release, where ANSYS FLUENT® and ANSYS Mechanical are coupled to perform one–way FSI [97]. The surface temperatures or surface forces obtained using the CFD solver is transferred to the structural solver based on post–processing.

The introduction of external interfaces makes coupling among many CFD and CSM software possible. For example, the standard code coupling interface MpCCI has attracted growing interests in the past years, as it provides adapters for several commercial codes, such as ANSYS Mechanical, ABAQUS®, ANSYS FLUENT, and Star–CD®. The two CFD codes can be coupled with the two CSM codes arbitrarily to perform one–way and two–way FSI simulations. However, since data exchange within timesteps is not supported by these codes, the coupling can only be explicit. In strongly coupled cases, such explicit approaches can easily lead to diverging solutions [98].

Chapter 4

FSI Benchmark and Parallel FSI

This chapter consists of two parts. The first one is studying and verifying the numerical FSI approach introduced in chapter 3 against the well–known unsteady FSI benchmark proposed by Turek and Hron (2006) [51]. The second one is investigating the parallel performance of the approach.

4.1 Benchmark Definition

The 2D benchmark test case focuses on the interaction between an incompressible laminar flow and an elastic structure. The geometries of the fluid and the solid domain are shown in Fig. 4.1 [99]. The benchmark configuration is an adaptation of the classic *flow around a cylinder* problem, where an elastic beam is attached to the downstream side of the rigid cylinder. Both the cylinder and the beam are submerged in the flow. With the given inlet velocity and fluid/solid material properties, the fluid pressure will induce a periodic oscillation of the beam. Moreover, the cylinder is intentionally positioned unsymmetrically in y–direction so that the onset of the oscillation will not be affected by numerical errors.
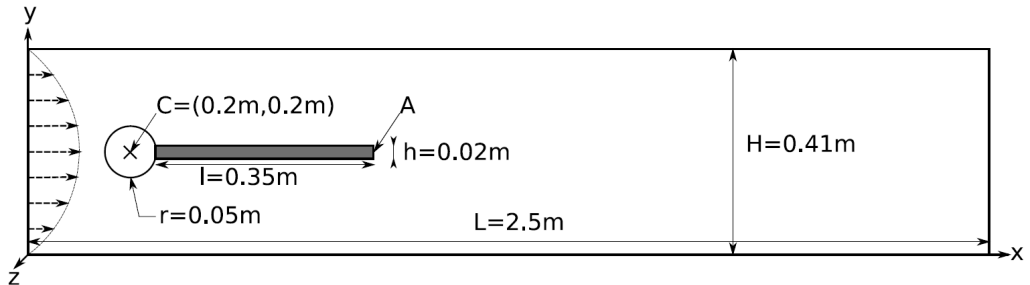

Figure 4.1: Geometric design of the benchmark (Becker et al., 2009)

The flow has a Reynolds number of 200, where the characteristic length is taken

as the cylinder diameter and the velocity as the inlet mean velocity. The fluid is considered to be Newtonian with the properties listed in Tab. 4.1. In particular, the large kinematic viscosity helps to maintain a low Reynolds number in the laminar regime. Moreover, the large fluid density and the low solid stiffness allow significant structural deformations. A parabolic velocity profile is specified at the inlet:

$$v_f(0,y) = 1.5\bar{v}_f \frac{y(H-y)}{(\frac{H}{2})^2} = 71.39y(0.41-y) \tag{4.1}$$

where $\bar{v}_f = 2$ m/s represents the inlet mean velocity and H denotes the channel height.

The beam is subjected to large deflections, while the material properties stay in the elastic range. Thus, the St. Venant–Kirchhoff constitutive law for finite deformation is applied.

Table 4.1: Material properties

Structure	Density	Poisson's ratio	Young's modulus
	10^3 kg/m^3	0.4	5.6×10^6 Pa
Fluid	Density	Kinematic viscosity	
	10^3 kg/m^3	10^{-3} m^2/s	

In the model verification, drag and lift forces exerted on the combination of the cylinder and the beam in the fully developed flow are compared with reference values, and displacements in x and y directions are compared with the reference at point A on the beam (Fig. 4.1).

4.2   Numerical Models

4.2.1   Laminar Flow

For this 2D test case, a thickness of 0.01 m is specified in z direction as to be used in the 3D CFD model, and the front/back faces are modeled as symmetric boundaries. The inlet velocity profile is given by Eq. 4.1. The pressure level can be set to an arbitrary value in incompressible flows. However, it can influence the fluid force acting on the FSI surface and consequently the structural deformation. Therefore, the absolute outlet pressure in this study is kept at zero to set the pressure level, which is consistent with the numerical benchmark case [51]. No–slip wall condition is prescribed at all other boundaries and the fluid–structure interface.

A timestep of 0.001 s is used here, which has been verified in earlier CFD works [51]. A more in–depth study on impacts of the timestep size in FSI simulations is

discussed in section 4.3.3.

Table 4.2: Detailed settings of the fluid model

Boundary conditions	Parabolic velocity profile at inlet
	$p_{stat,out} = 0$ at outlet
	No–slip walls at $y = 0$, $y = 0.41$ m, cylinder, and beam
	Symmetry at $z = 0$ and $z = 0.01$ m
Convection scheme	Central Differential
Convergence criterion	RMS residuals of all governing equations $< \varepsilon$
Transient scheme	Second–order backward differencing
Timestep size	0.001 s
Mesh for parallel computations	Hexahedral
	Fine mesh = 999,424 elements
	Medium mesh = 249,856 elements
	Coarse mesh = 62,464 elements

Figure 4.2: Coarse mesh for the fluid field, every second grid line is plotted

4.2.2 Elastic Beam

The beam model employs the element type named *SOLID45*, which represents 3D 8–node structural element with three DOFs at each node. A mesh density study is presented in section 4.3.2, based on which the mesh with 21 elements in x direction, 4 in y direction, and 2 in z direction is selected for this beam problem.

In addition to the fixed left end, the z–displacements of nodes located at $z = 0$ and $z = 0.01$ m are constrained to zero.

Geometric nonlinearity is included by applying finite stress/strain formulations considering arbitrarily large deflections and rotations. The transient process is solved

with a time marching scheme using the Newmark–β method. In particular, the numerical parameters in Eq. 2.33 and Eq. 2.34 are chosen as $\gamma = 0.6$ and $\beta = 0.3$, which introduce a little numerical dissipation and guarantee unconditionally stable transient solutions.

4.2.3   FSI Settings

The x– and y–components of displacements and forces are exchanged at the beam surface. While it is necessary to keep the under–relaxation factor for displacements less than 0.1 in order to avoid divergence, there is no such stringent rule required for the forces. The main reason is that the pressure peak caused by the abrupt change in geometry can result in significant structural deformation, which usually leads to diverged solutions within a few timesteps. The FSI convergence criterion of 10^{-3} is tested to be sufficient for all coupling variables. The mesh deformation scheme and the timestep size are studied in section 4.3.3.

Table 4.3: FSI parameters

Coupling variables	U_x, U_y	F_x, F_y
Transfer direction	Solid $\rightarrow$ fluid	Fluid $\rightarrow$ solid
Interpolation scheme	*Profile preserving*	*Conservative*
FSI convergence criterion	10^{-3}	10^{-3}
Under–relaxation factor	0.1	$0.75 \sim 1.0$

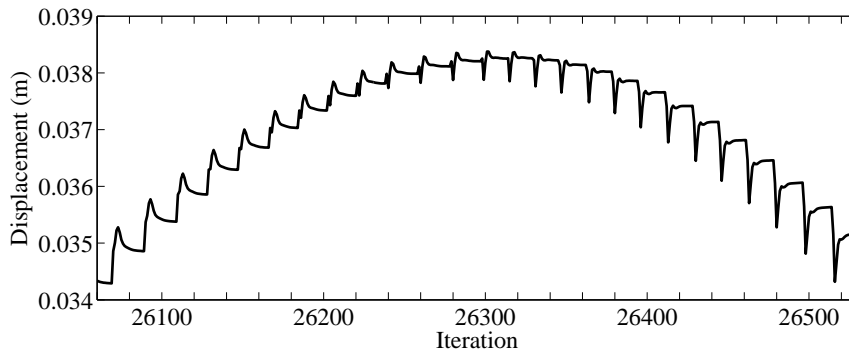Figure 4.3: Convergence behavior of U_y at point A over FSI iterations

A typical convergence history of U_y at point A is plotted against FSI iterations in Fig. 4.3. Each peak represents the start of a new timestep, and each timestep contains about twenty FSI iterations. In each timestep, the monitored variable changes steeply in the first several iterations and then gradually converges to a constant value.

4.3   Verification and Discussion

4.3.1   Fluid Model

In this section, only the transient flow is computed with no structural deformation involved. The boundary conditions described in section 4.2.1 are applied.

First, the mesh dependency is studied as shown in Fig. 4.4 and Tab. 4.4, where the amplitudes of drag and lift forces are computed on different meshes. The meshes used here have one element in z direction. In Tab. 4.4 the quantities are in terms of amplitude and mean value. In particular, the former one is defined as half of the difference between the maximal and minimal values, and the latter one is defined as the average of the maximum and the minimum.

Figure 4.4: CFD mesh density study in respect of force amplitudes

Table 4.4: CFD verification on different meshes with respect to drag/lift forces expressed as mean value $\pm$ amplitude (N)

	No. elements	Drag	Lift
	25,720	451.09 ± 4.8720	-45.450 ± 390.03
Present CFD	49,980	451.58 ± 6.1785	-23.558 ± 466.74
	121,644	448.85 ± 5.8185	-18.704 ± 432.19
Reference		439.45 ± 5.6183	-11.893 ± 437.81

Then, the drag and lift forces on the fine mesh are verified against the numerical reference values [51] as shown in Fig. 4.5 and Tab. 4.4 with a time duration of 0.6 s. Good agreements can be found in predicting the oscillation period and force amplitude between the two. However, the model tends to over–predict the average drag/lift forces.
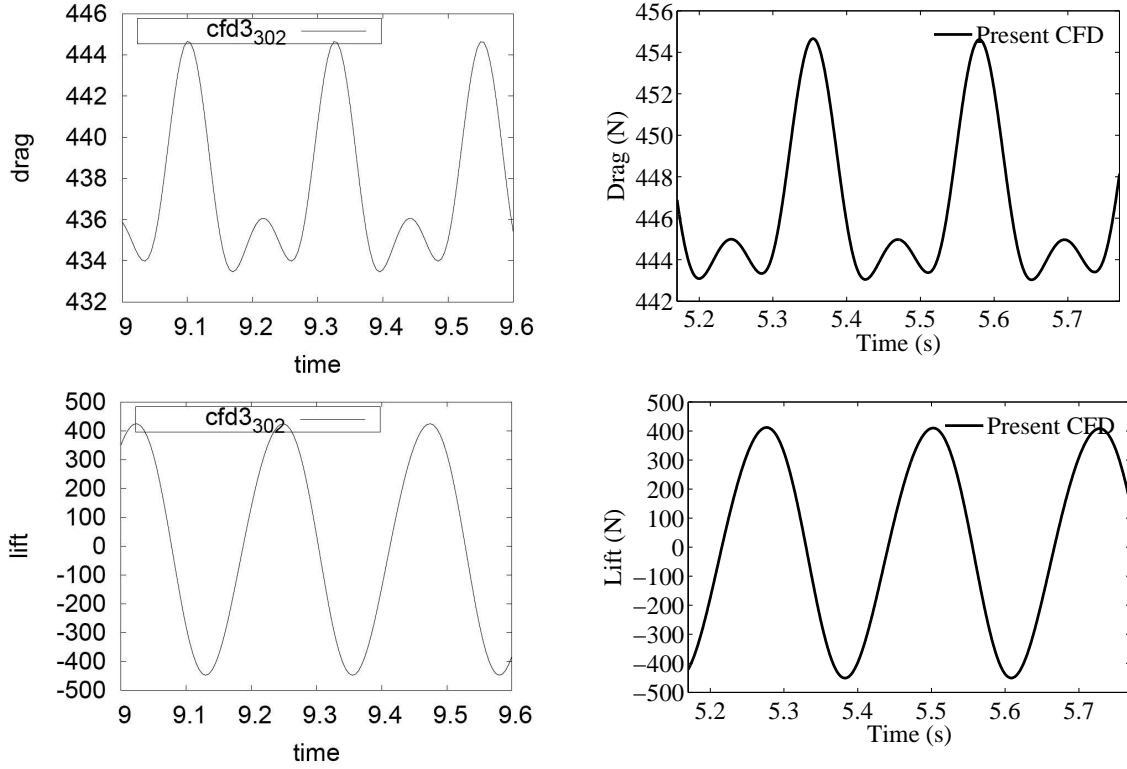
Figure 4.5: Drag/lift forces obtained by CFD simulations on the fine mesh (right) compared with reference results (left)

Due to different scaling in the thickness, the computed forces are first amplified by 100 times and then compared with reference values. In addition, the timestep is 0.001 s in the present model and 0.005 s in the reference.

4.3.2   Solid Model

The CSM model is verified in a transient analysis with initial undeformed configuration, excluding the fluid domain. A sudden body force load of 2 m/s^2 is applied to the beam. The timestep equals 0.02 s as verified in [51].

First, a mesh density study is conducted (Fig. 4.6 and Tab. 4.5), showing that the amplitude increases with the number of elements. The mesh described in section 4.2.2 corresponds to the medium mesh and is sufficient to deliver accurate results. The other two meshes are obtained by coarsening/refining the medium mesh in both x– and y–directions twice.

Then, the transient response of displacements at point A is verified (Fig. 4.7) on the chosen mesh. The numerical results show good agreement with reference values (Tab. 4.5). Note that the Young's modulus used for the present CSM tests is 1.4×10^6 Pa, which is different from that used in the FSI setup (Tab. 4.1).
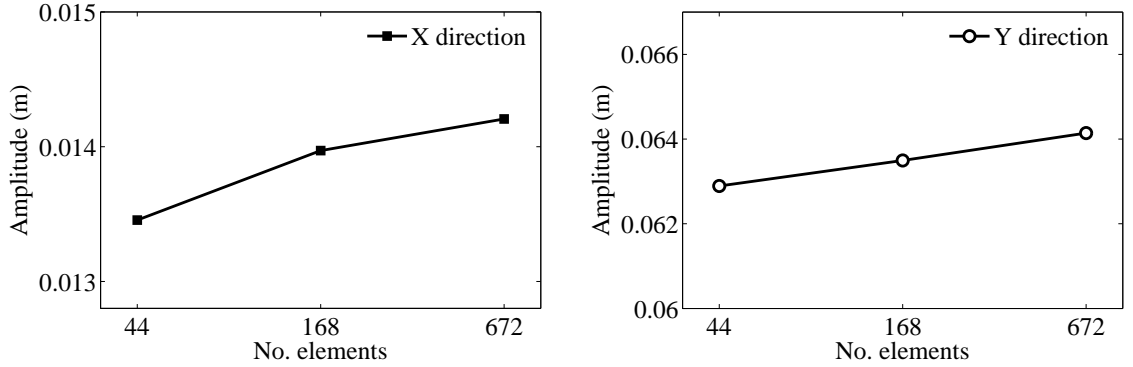
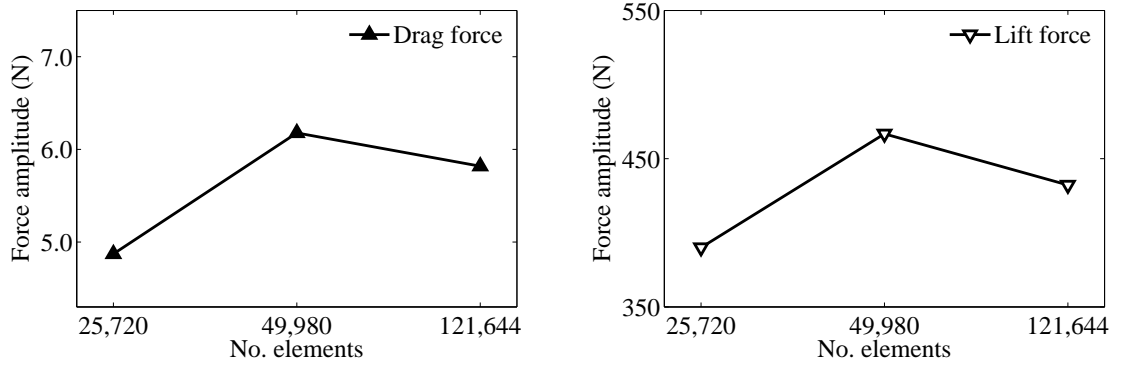Figure 4.6: CSM mesh density study in respect of amplitudes

Table 4.5: CSM verification on different meshes with respect to U_x/U_y of point A expressed as mean value $\pm$ amplitude (mm)

	No. elements	U_x	U_y
	44	-13.456 ± 13.456	-62.073 ± 62.891
Present CSM	168	-13.973 ± 13.972	-63.515 ± 63.495
	672	-14.207 ± 14.206	-64.089 ± 64.141
Reference		-14.404 ± 14.408	-64.371 ± 64.695

4.3.3 FSI Model and Mesh Deformation

As discussed in section 3.1, the current FSI approach involves a wide choice of mesh stiffness models, which will result in different mesh deformations.

Since it is critical to preserve good mesh qualities throughout the simulation process, the mesh stiffness model chosen for this particular problem must not lead to large distortions. Moreover, there is no universal optimal mesh stiffness model, as the choice depends on both the geometry and the mesh.

Various mesh stiffness models are applied to the deformed fluid domain where point A is displaced by 0.08 m in y–direction, and the local mesh distortions are observed. The overall mesh deformation is similar for different models as shown in Fig. 4.8 (a). For the *increase near boundaries* model, the mesh obtained using $C_{stiff} = 1$ is of the best quality, while C_{stiff} of 5 and 10 result in mesh distortions in areas away from boundaries due to excess of the upper limit set by the code. As all exceeding values will be reset to the limit, it finally leads to the case that the mesh is deformed uniformly inside the region and abruptly outside the region. For the *increase near small volumes* model, C_{stiff} of 2 is more favorable than C_{stiff} of 0.5, as larger mesh distortions are observed at the beam end in the latter case. In addition,
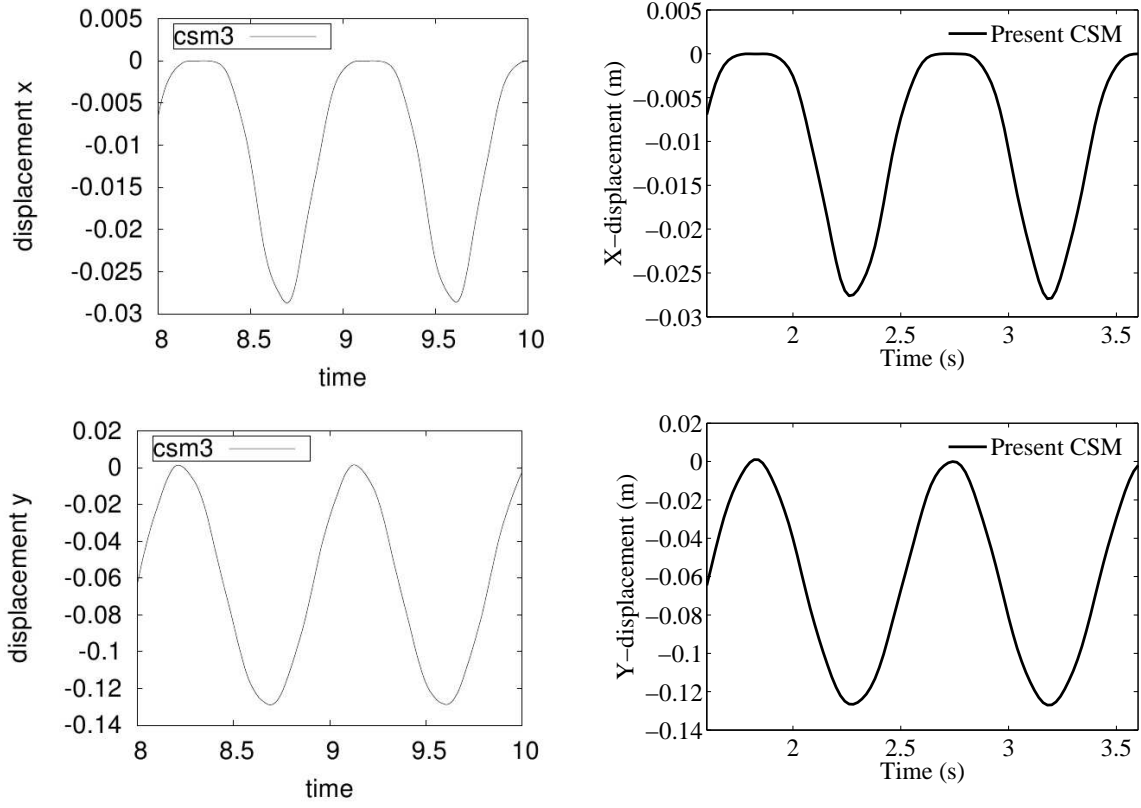
Figure 4.7: U_x/U_y of point A obtained by transient CSM simulations on the medium mesh (right) compared with reference results (left)

the constant mesh stiffness model is worse than the other two models concerning the mesh distortion around the beam end. Finally, the *increase near boundaries* model with $C_{stiff} = 1$ is chosen for this study.

The timestep dependency study is carried out in terms of displacement amplitudes. It clearly shows in Fig. 4.9 that the solutions converge when the timestep is less than 0.001 s.

Furthermore, the dependency of amplitudes on the fluid mesh is shown in Fig. 4.10 and Tab. 4.6, where the structural mesh is set to the chosen one (section 4.3.2). The fluid meshes have one element in z direction. The timestep is set to 0.001 s. It is found that the fine fluid mesh leads to large displacement amplitudes in both x and y directions. The medium and fine fluid meshes lead to very close results.

For verification, U_x and U_y of point A obtained on the medium fluid mesh are compared with reference values. In Fig. 4.11, displacements of the fully developed oscillation are plotted for a time span of 0.5 s. It turns out that both the period and the displacement are in good agreements between model predictions and reference values. For example, the amplitudes of U_y is over–predicted by 6.8% (Tab. 4.6).
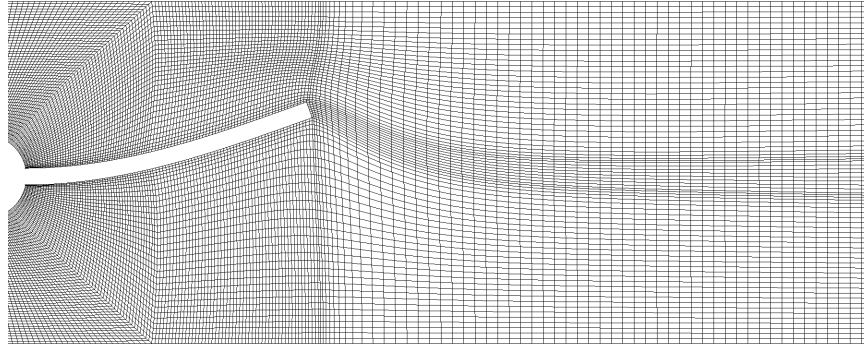
(a) Overview of mesh deformation

$C_{stiff} = 10$ $C_{stiff} = 5$ $C_{stiff} = 1$
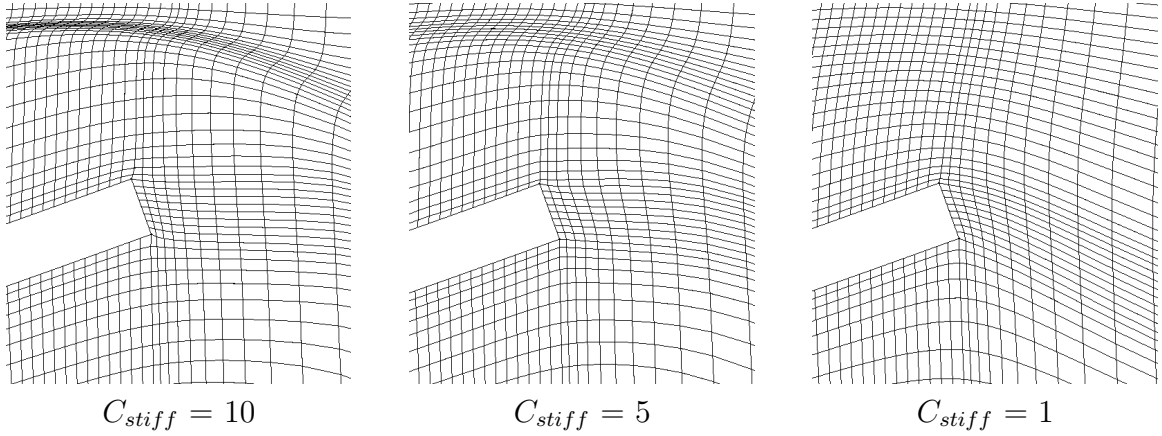
(b) *Increase near boundaries*

$C_{stiff} = 2$ $C_{stiff} = 0.5$
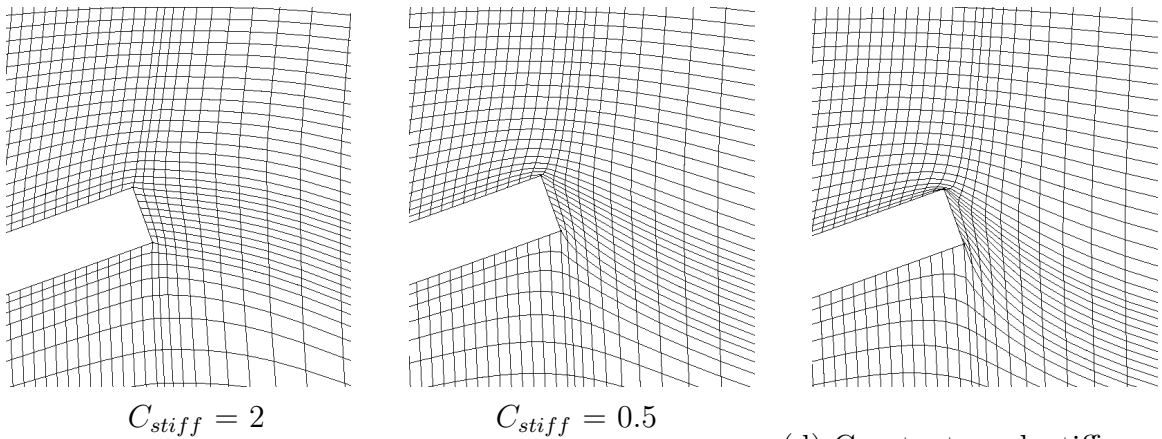
(d) Constant mesh stiffness

(c) *Increase near small volumes*

Figure 4.8: Influence of various mesh stiffness models on mesh deformation
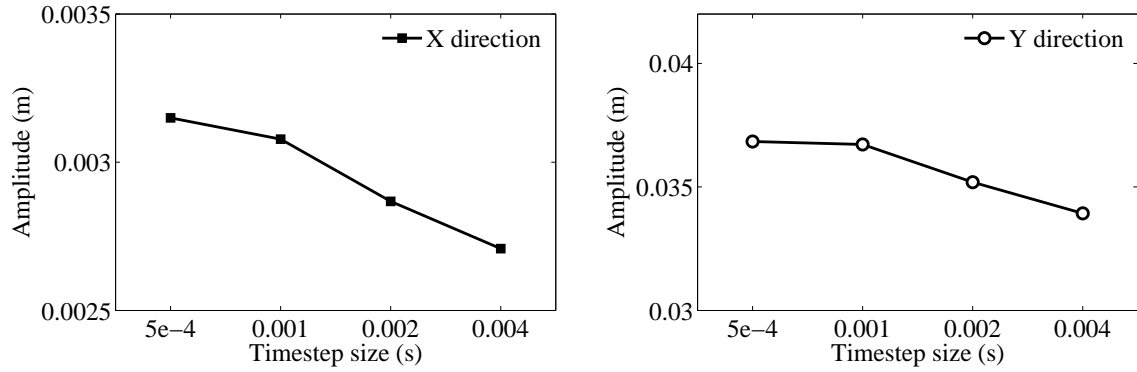
Figure 4.9: FSI verification of timestep size in respect of amplitudes
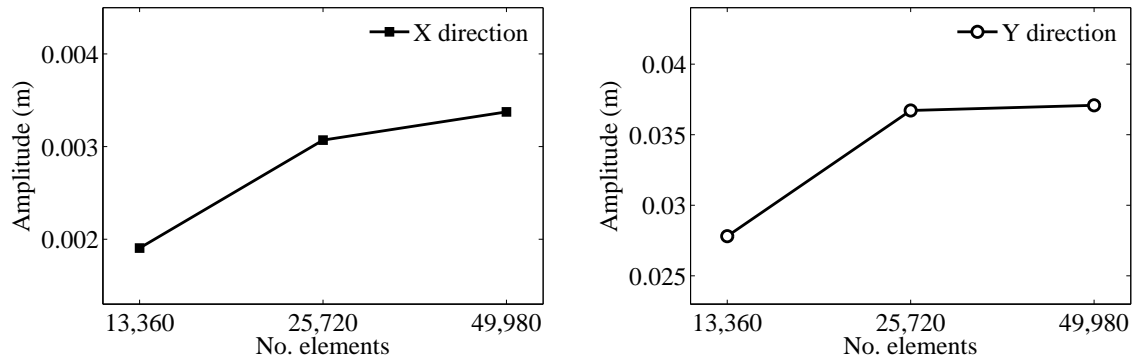
Figure 4.10: FSI verification of fluid mesh dependency in respect of amplitudes (timestep = 0.001 s)

Table 4.6: FSI verification on different fluid meshes with respect to U_x/U_y of point A expressed as mean value $\pm$ amplitude(mm)

	No. elements	U_x	U_y
	13,360	-2.00 ± 1.90	1.69 ± 27.81
Present FSI	25,720	-3.24 ± 3.07	1.75 ± 36.72
	49,980	-3.52 ± 3.37	2.48 ± 37.09
Reference		-2.69 ± 2.53	1.48 ± 34.38
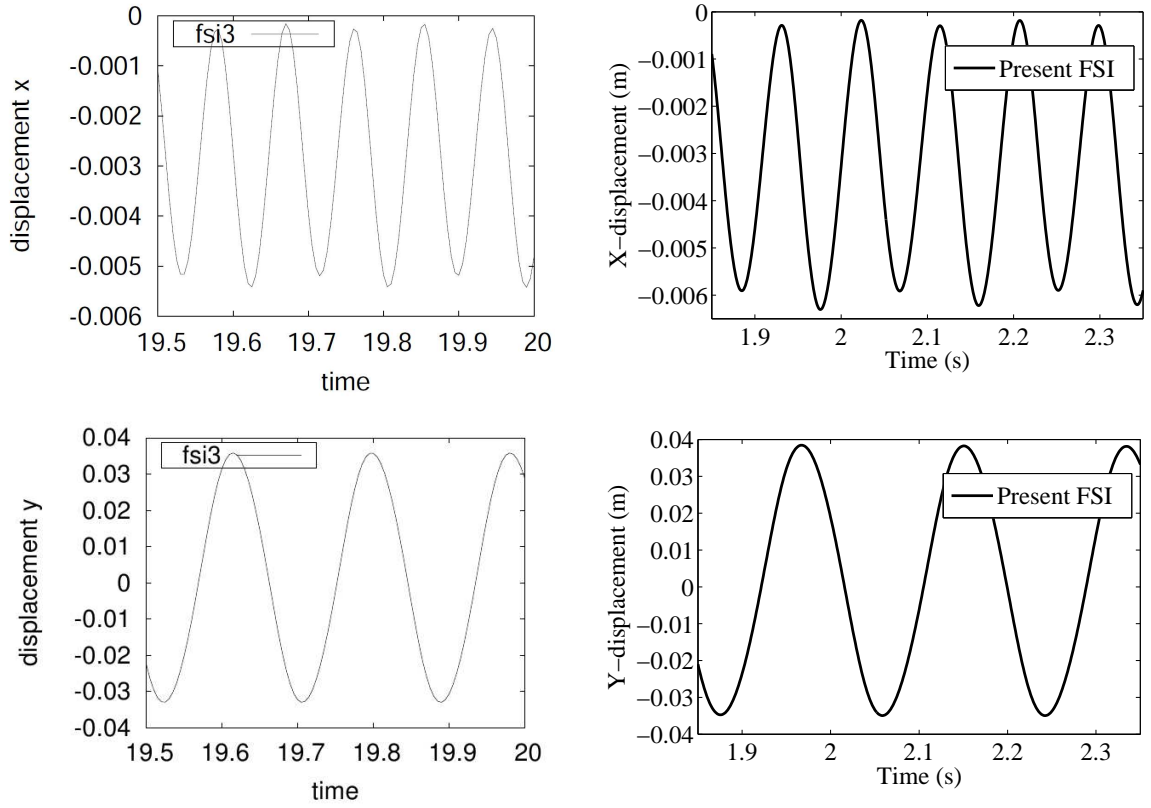
Figure 4.11: U_x/U_y of point A obtained by the current FSI approach on the medium fluid mesh (right) compared with reference results (left)

4.4 Parallel FSI Study

4.4.1 Overview

The aim of this section is studying the parallel performance of the FSI approach. In particular, parallel performance refers to parallel speed–up, parallel efficiency, parallel scalability, and parallel multigrid acceleration. In this section, the fluid field with various meshes is computed in parallel using algebraic multigrid (AMG) and single grid (SG) schemes, while the solid field and the rest are computed serially. A complete summary for the parallel study can be found in Tab. 4.7. The fine/medium/coarse meshes are defined in Tab. 4.2. All following computations are performed over an oscillation period of 0.2 s using a timestep of 0.001 s.

Regarding the parallel environment, the computations are conducted on an IBM p 575 SMP cluster with POWER6 nodes.

Table 4.7: Overview of parallel computations

Parallel performance	Mesh	No. processors	Multigrid
Parallel speed–up Parallel efficiency	Fine	1,2,4,8,16,32	AMG
Parallel scalability	Fine Medium Coarse	32 8 2	AMG
Multigrid acceleration	Fine	1,2,4,8,16,32	AMG, SG

4.4.2   Partitioning

The fluid mesh is partitioned automatically using the MeTiS partitioner (see section 3.1). The partitioning of various meshes on 2, 8, and 32 processors is demonstrated in Fig. 4.12. Despite the miscellaneous shapes of the partitions, each partition contains approximately the same amount of elements as shown in Tab. 4.8. Therefore, it is assumed that the computational workload is evenly distributed across the processors to achieve optimal resource utilization.

Table 4.8: Partition size in terms of percentage of the total number of elements

	Smallest partition	Largest partition
Fine mesh on 32 proc.	3.06%	3.22%
Medium mesh on 8 proc.	12.3%	12.7%
Coarse mesh on 2 proc.	49.7%	50.3%

4.4.3   Parallel Performance

Figure 4.13 shows that the wall clock computational time is reduced significantly as the number of processors increases. The behavior of accelerated computation is usually assessed by the speed–up and the efficiency.

The parallel speed–up is defined as the serial computational time divided by the parallel computational time. The ideal parallel speed–up which equals the number of processors usually cannot be reached. In reality, the reduction in computational time is always less than the increase in number of processors (Fig. 4.14).

The parallel efficiency is defined as the serial computational time divided by the total CPU time of the parallel computations. Accordingly, the efficiency of serial computations is 100%, and the efficiency of parallel computations can never reach
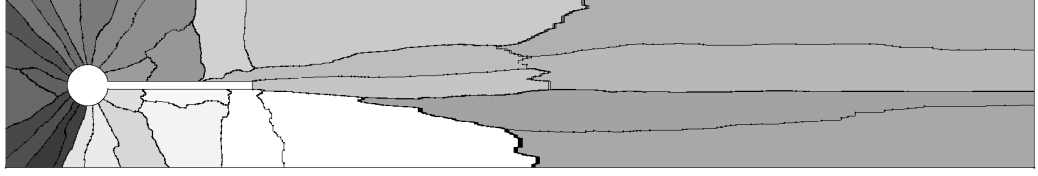
(a) Fine mesh on 32 processors
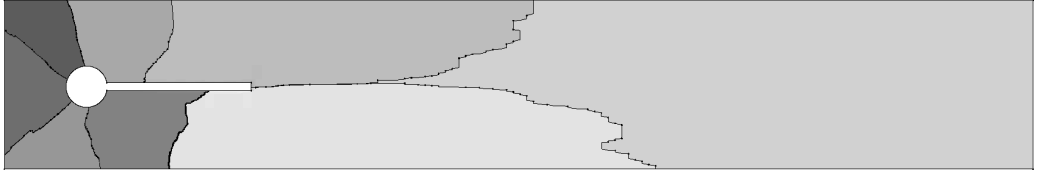
(b) Medium mesh on 8 processors

(c) Coarse mesh on 2 processors

Figure 4.12: Partitioning of the fluid mesh
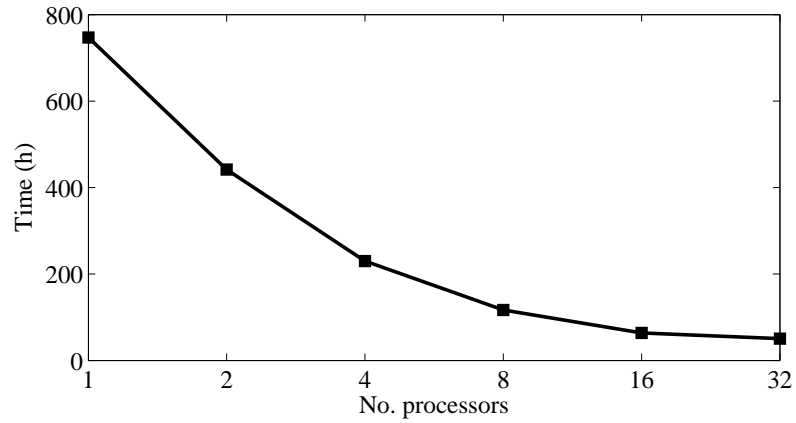
Figure 4.13: Wall clock computational time

100%. It can be seen in Fig. 4.15 that the parallel efficiency decreases gradually with the increase of number of processors. However, there is a clear drop in parallel efficiency from 16 to 32 processors, suggesting that further increasing the number of
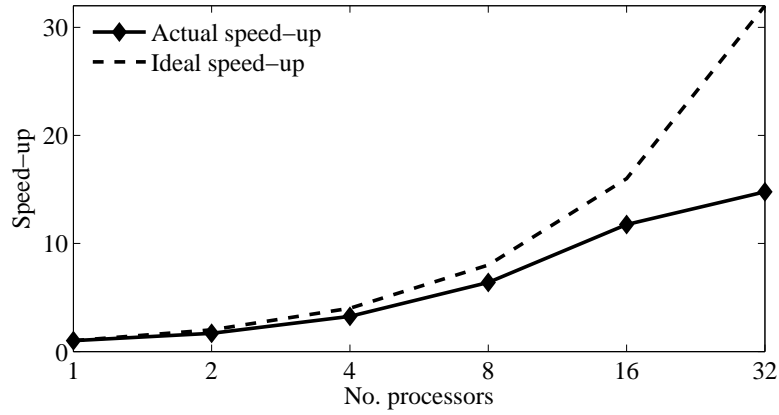
Figure 4.14: Parallel speed–up in terms of serial computational time divided by parallel computational time

processors will bring even less speed–up and the parallel computation becomes less efficient. Therefore, the optimal parallel performance for the present case is achieved on no more than 16 processors with a minimum of 62,500 elements per partition.
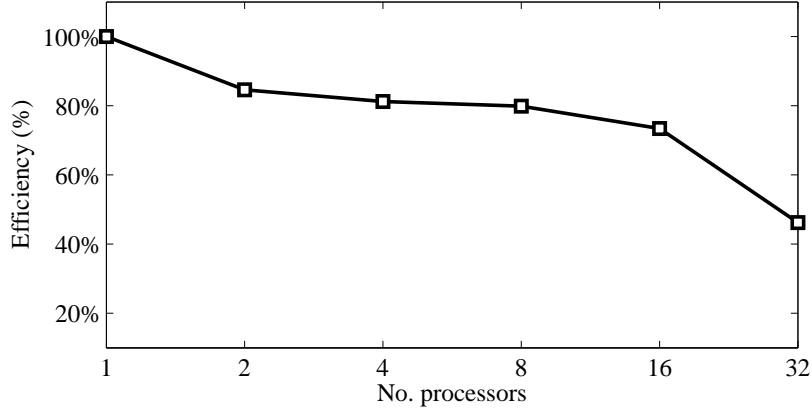
Figure 4.15: Parallel efficiency in terms of serial computational time divided by total CPU time

The wall clock time of computations should be similar for cases with the same ratio of mesh size to number of processors. This performance is defined as the parallel scalability, which indicates that at certain computational costs, larger problems can be solved by using proportionally more processors. In the present case, the constant ratio is achieved by distributing the coarse/medium/fine mesh on 2/8/32 processors, respectively. A good parallel scalability performance can be recognized in Fig. 4.16.

The fluid solver uses a multigrid strategy to solve the equations rapidly. All the results above are obtained using the AMG scheme. The acceleration of AMG over
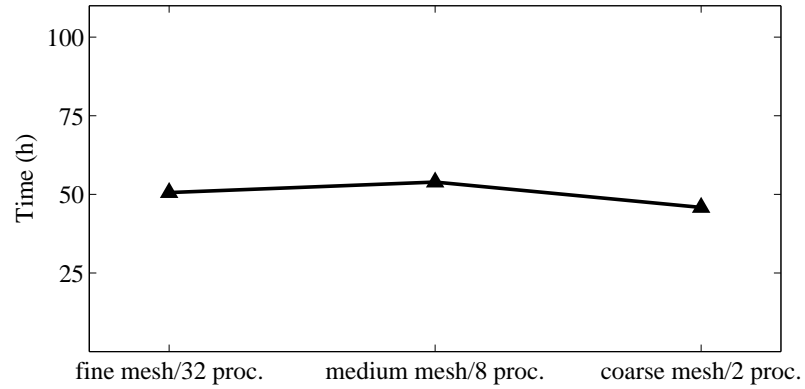
Figure 4.16: Parallel scalability in terms of wall clock computational time at constant no. elements/no. processors ratio

SG is shown in Fig. 4.17. AMG accelerates the computation by a factor of four. Moreover, SG has a similar parallel speed–up performance.
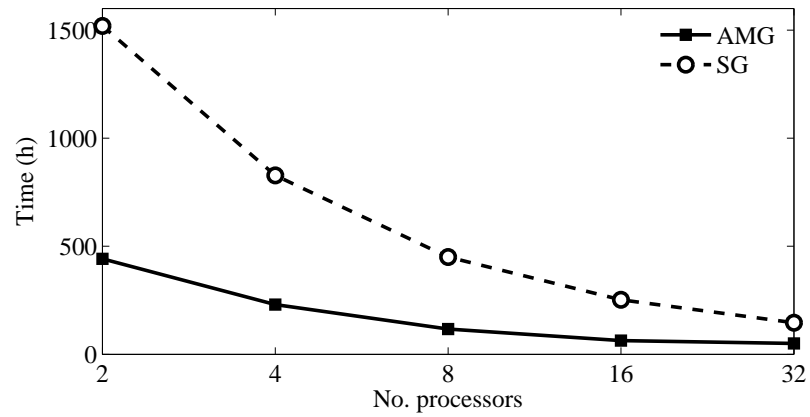
Figure 4.17: Comparison of wall clock computational time of parallel AMG and parallel SG

4.5 Summary

In the first part of this chapter, the numerical FSI approach is verified against the benchmark of unsteady FSI between an incompressible laminar flow and an elastic structure. In the CFD verification, the mesh density is studied, and then the oscillation periods and amplitudes of the lift/drag forces predicted by the present simulation are found to agree well with reference values, while the mean values of the forces are

over–predicted. Based on the mesh sensitivity study, the transient response of the CSM model shows good agreement with the reference. In the FSI verification, various mesh stiffness models are studied regarding local mesh distortions, followed by dependency studies of fluid mesh and timestep size. At last, the displacement results of FSI simulations are compared with reference values. The oscillation of the displacements highly resembles the reference with consistent period, while the amplitudes and mean values are little over–predicted. In conclusion, the current FSI approach shows a relatively good accuracy based on the benchmark study.

In the second part, the parallel performance of the FSI approach is investigated in various respects. A significant parallel speed–up is observed, and an optimal parallel efficiency is reached with a minimum of 62,500 elements per partition with excellent parallel scalability. It turns out that the computation can be accelerated by four times when introducing the algebraic multigrid scheme. Finally, an evenly distributed workload across the processors is also achieved in the partitioning. In sum, the studies above suggest that the current FSI approach provides good parallel performance.

Chapter 5

FSI Case I – Fluid Force Induced Vibration

In this chapter the fluid force induced vibration of a non–rotating, room temperature, straight–through labyrinth seal is presented. Here we focus on the mechanical FSI effects, hence the coupling surface is treated as a movable adiabatic wall. Due to the strongly coupled nature of the problem, an implicit approach is adopted for the two–way transient FSI, in which the flow and the structure are modeled in 3D.

The outline of this chapter is as follows. First the numerical models of the fluid and the seal structure are defined and the coupling interface is set up. Then, the model is verified and detailed discussion on the leakage behavior and flow features are shown. On the structural side, modal analysis reveals the natural frequencies and mode shapes of the rotor. Finally, results of the mechanical FSI are presented, including studies of the dependency on initial conditions and the influence of pressure ratio and mass flow on the vibration amplitude. It is also demonstrated that the vibrations are entirely induced by fluid forces.

5.1 Numerical Models

5.1.1 Fluid Field

The geometry and boundary conditions of the fluid model shown in Fig. 5.1 [100] are based on a steady, room temperature, non–rotating experiment [11] of a four–tooth straight–through labyrinth seal conducted on the test rig as in Fig. 1.2. Detailed settings of the CFD model are listed in Tab. 5.1. The inlet total temperature $T_{tot,in}$ is set at room temperature 297 K. Since the gas and the test rig are at room temperature, heat transfer at walls can be neglected, thus the stator and the rotor are modeled as adiabatic walls, which is a common practice in CFD simulations of labyrinth seals [4, 35]. Both inlet total pressure $p_{tot,in}$ and outlet static pressure $p_{stat,out}$ are varied

to yield a pressure ratio π ranging from 1.7 to 3.8.
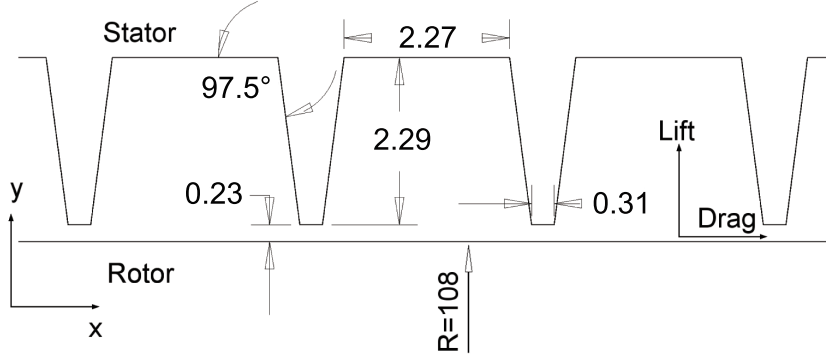
(a) Cross–sectional view (mm)
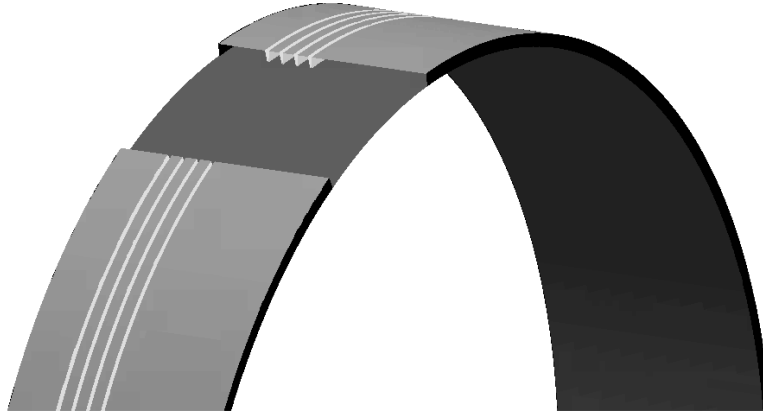
(b) 3D view

Figure 5.1: Fluid domain of the four–tooth straight–through labyrinth seal

The validity of the standard $k-\varepsilon$ turbulence model for straight–through labyrinth seals has been repeatedly demonstrated in references [28–30]. $k-\varepsilon$ models with logarithmic wall functions require proper near–wall element sizes. Hence, y^+ must be approximately in the range from 30 to 300 [83]. However, it is extremely difficult to maintain the proper y^+ everywhere in labyrinth seals due to the wide velocity range and hexahedral meshes as in this case. Therefore, the *scalable wall function* is applied, which switches off the logarithmic wall function when y^+ is smaller than 11.06 and solves for the velocity profile across the viscous sublayer. The sensitivity of near–wall element sizes is discussed separately in section 5.2.

To ensure convergence, critical global variables such as mass flows are monitored in addition to the RMS and imbalance criteria. The solution is considered to be converged when the changes of the global variables are within a fixed tolerance. The convergence history of mass flow over iterations is shown in section 5.2.

Table 5.1: Settings of the CFD model

Fluid type	Air, ideal gas
Boundary conditions	Inlet: $T_{tot,in} = 297$ K, $p_{tot,in}$
	Outlet: $p_{stat,out}$
	No–slip smooth adiabatic walls
Turbulence model	Standard $k - \varepsilon$ with *scalable wall function*
Convection scheme	*High resolution* (second–order)
Convergence criteria	RMS residuals of all conservation equations $< \varepsilon$
	Imbalances of mass, momentum, and enthalpy $< 1\%$
	Global variables do not change over iterations
Transient scheme	Second–order backward differencing
Timestep size	5×10^{-6} s
Mesh	Hexahedral, 1.7 million elements

The FSI effect requires both the fluid and the solid analysis to be transient. In addition, it is shown that the fluid requires a much smaller timestep size than the solid. Hence, in order to balance between computational efficiency and stability, it is critical to determine a suitable timestep size based on the fluid requirement. It is shown by means of numerical tests that the optimal timestep is 5×10^{-6} s.

5.1.2 Rotor

Since this work focuses on the rotor vibration, modeling of the stator is neglected. The rotor is simplified as a disk fixed in the middle of a thin wall shaft (Fig. 5.2) to represent the fundamental characteristics of a rotor. The disk is surrounded by the fluid domain. The small deformation justifies a linear structural analysis with a linear elastic material law. The material is steel with density 7806 kg/m^3, Young's modulus 2.078×10^{11} Pa, and Poisson's ratio 0.3.

Numerical tests reveal that the deformation of the rotor disk is negligible compared to that of the shaft, hence the rotor disk is treated as rigid body to reduce computational time. Furthermore, considering that mesh displacements normal to the area are not allowed at the inlet, the axial displacement of the disk is constrained. The two ends of the shaft are clamped. The shaft is modeled with the second–order thin wall pipe element *PIPE16*. As convergence criteria, the L^2 norm of all DOFs are kept below 10^{-3}. The Newmark–β time integration method is used for transient term discretization.
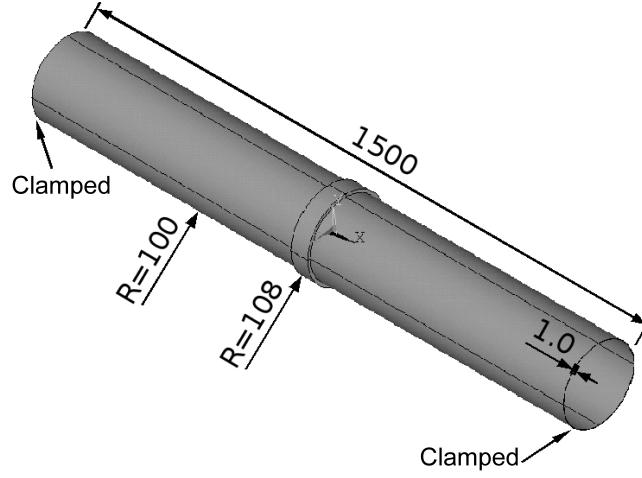
Figure 5.2: A rotor disk fixed on a clamped–clamped thin wall shaft (mm)

5.1.3   FSI Parameters

Forces and displacements are transferred across the fluid–solid surface as shown in Fig. 5.3. There are two reasons to use two–way implicit coupling in this problem. First, the one–way coupling cannot take the displacement of the coupling surface into account. Second, the explicit coupling usually has stability problems for strongly coupled physics. The FSI parameters of this test case are listed in Tab. 5.2. As we focus on the mechanical FSI, no thermodynamic variables are considered here. The convergence criterion of 10^{-3} turns out to be strict enough and is used in the model. There is no need to involve under–relaxation. The mesh stiffness model is chosen as *increase near small volumes* with $C_{stiff} = 1$ and its convergence criterion RMS $< 10^{-4}$. The FSI and the fluid timesteps are equal.
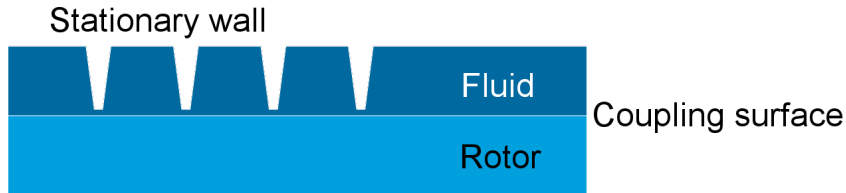
Figure 5.3: FSI coupling surface

    The fluid field computation requires much more computer resources than the combination of the solid field computation and FSI interpolation/controlling. Therefore, the fluid solver is run in parallel on 16 processors, while the rest are run on a single processor. All the simulations are carried out on an IBM p 575 SMP cluster with POWER6 nodes.

Table 5.2: FSI parameters

Coupling variables	Displacement	Force
Transfer direction	Solid $\rightarrow$ fluid	Fluid $\rightarrow$ solid
Interpolation scheme	*Profile preserving*	*Conservative*
FSI convergence criterion	10^{-3}	10^{-3}
Under–relaxation factor	1.0	1.0

5.2 CFD Verification

The CFD model sensitivity is first examined with respect to the mesh density and the near–wall element size at various locations as marked in Fig. 5.4. Figure 5.5 shows the dependency of mass flow $\dot{m}$ and lift force F_{lift} on the mesh. The number of elements at position x is labeled as nx and the near–wall element size is referred to as normalized sx. The difference is defined against the result with the smallest near–wall element size and the largest number of elements. The dimensionless near–wall element size is normalized with the largest near–wall element size used.
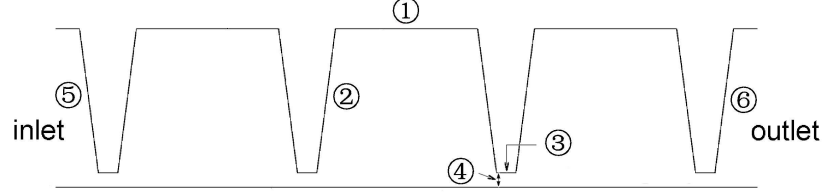
Figure 5.4: Regions of the labyrinth seal

The study clearly shows that $\dot{m}$ is more sensitive to the mesh than F_{lift}. Therefore, the mesh is chosen according to its influence on $\dot{m}$. To ensure a relative error of less than 0.1% for $\dot{m}$, it requires a total of 1.7 million hexahedral elements in the model, as shown in Fig. 5.6. In addition, the mass flow has been monitored as one of the convergence criteria. It is observed that the mass flow is well converged when the other two criteria are satisfied. The typical convergence history of the mass flow in a steady CFD analysis controlled by the other two criteria is plotted in Fig. 5.7.

Compared with experimental measurements, it turns out that numerical simulations tend to over–predict the leakage by 10% [101]. To compensate for this discrepancy and the lack of CFD studies by other researchers, we compare the numerical results with the calculations based on a KTK (knife-to-knife) code [102]. In the test data source [11] the KTK code is used to calculate the leakage through the seal, and the predicted $\dot{m}$ is also 10% larger than experimental results. Since KTK method is
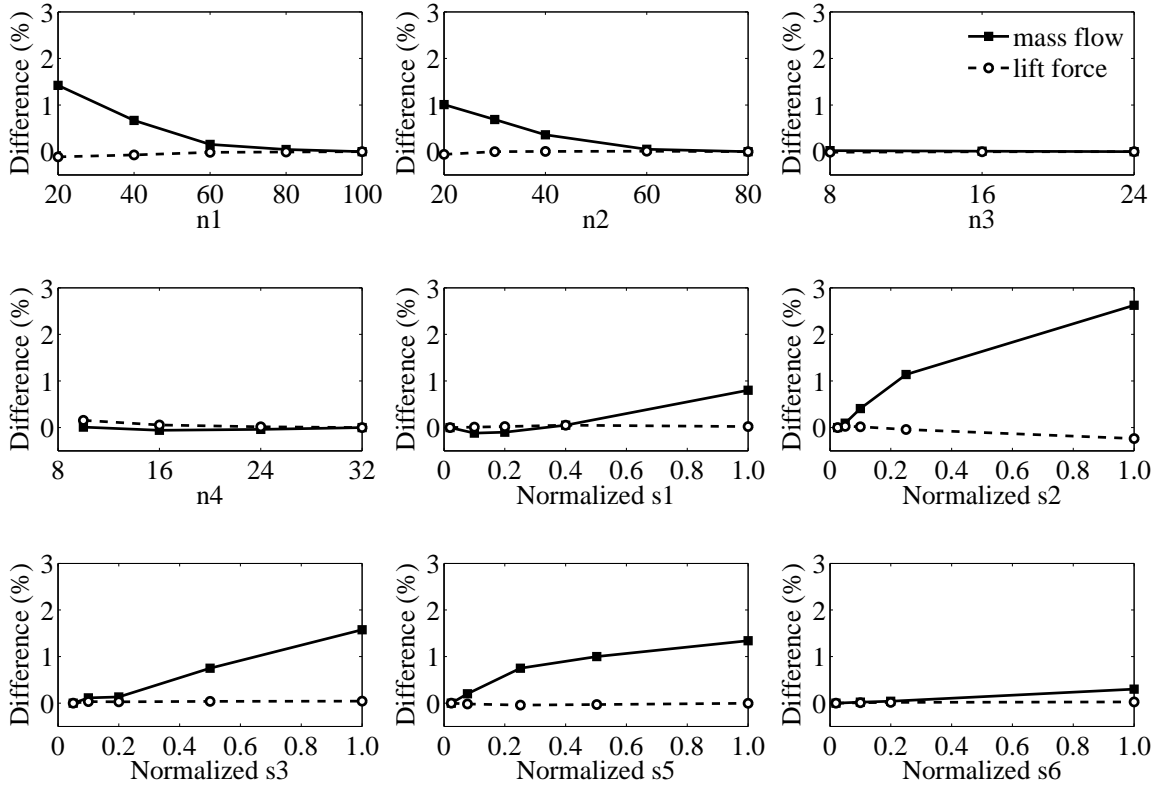
Figure 5.5: Mesh dependency study of the CFD model with respect to near–wall element size and mesh density at various locations
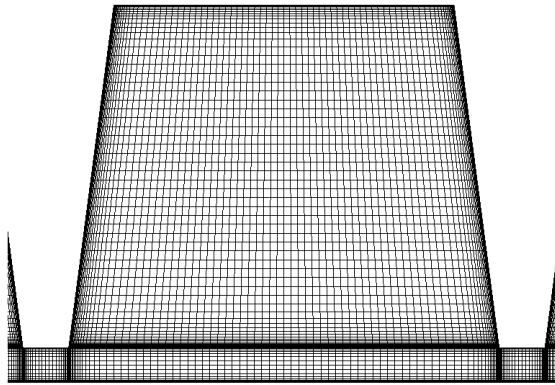
Figure 5.6: Mesh after dependency study

proved to be reliable within its calibration range for basic quantities in simple seal geometries, such as $\dot{m}$ in straight–through labyrinth seals, the numerical results are acceptable.
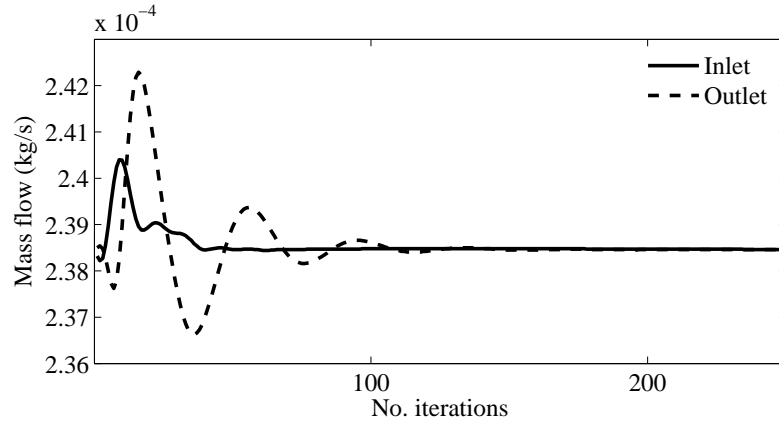
Figure 5.7: Convergence history of mass flow in a steady CFD analysis

5.3 Results and Discussion

5.3.1 Flow Features

Figure 5.8 shows the leakage performance under various pressure ratios (see Eq. 2.7). The flow factor defined in Eq. 2.2 remains constant when the pressure ratio increases beyond a critical value, suggesting that the flow is choked.
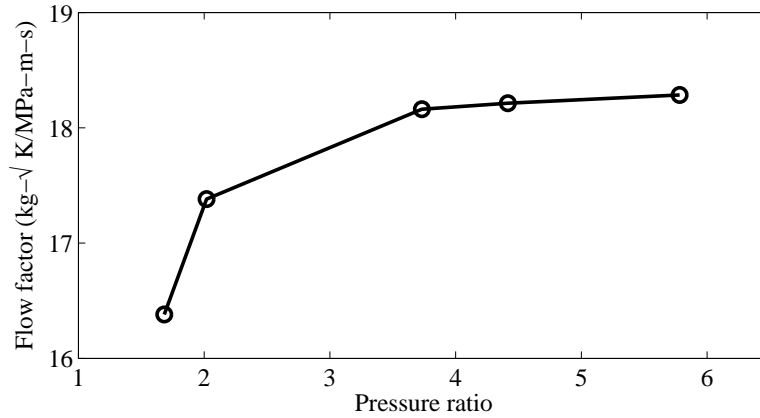
Figure 5.8: Leakage performance of the labyrinth seal

Based on the fluid fields shown in Fig. 5.9, the following features can be recognized: 1) there is a major vortex structure in each cavity; 2) the Mach number increases across the seal and reaches its maximum after the last tip; 3) the static pressure is homogeneously distributed in each cavity; 4) the static pressure and the density decrease as the flow accelerates; 5) the flow is strongly compressible as the density varies at a factor of four.
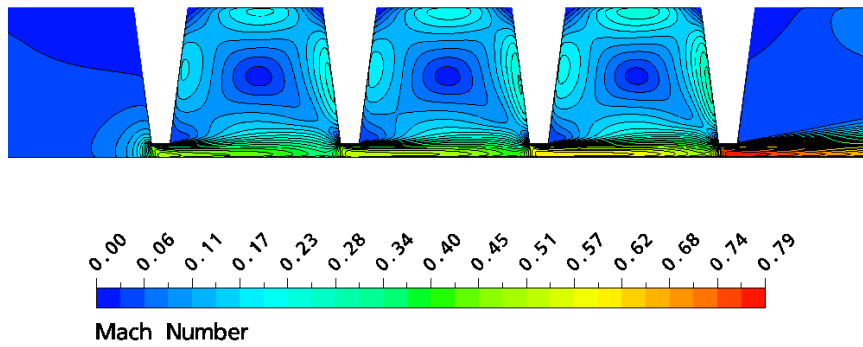
(a) Mach number distribution
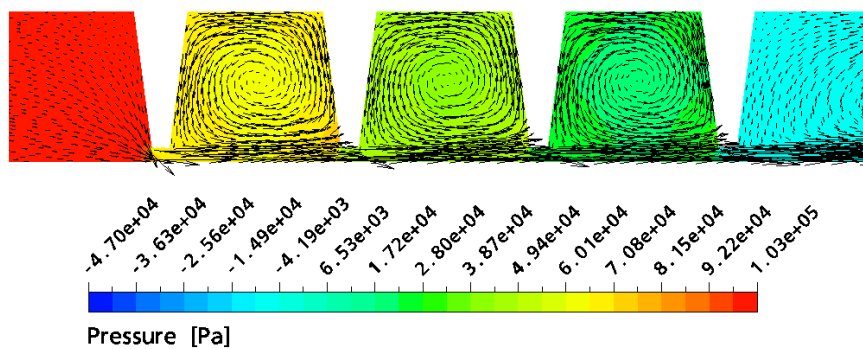
(b) Static pressure field and velocity vector field
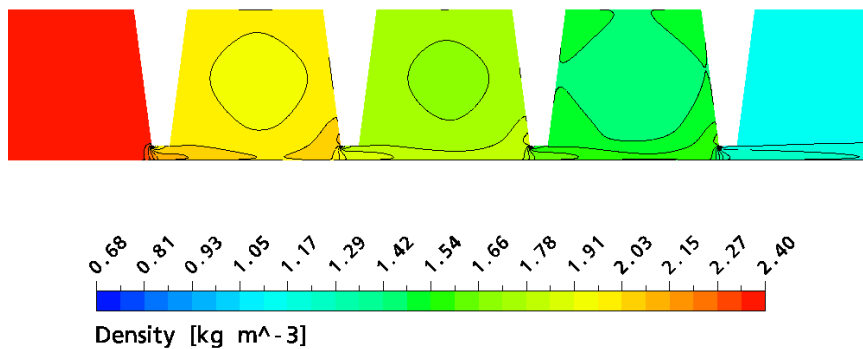
(c) Density distribution

Figure 5.9: Fluid field of the labyrinth seal (pressure drop = 103 kPa)

5.3.2   Modal Analysis of the Rotor

A modal analysis is conducted to determine the natural frequencies and mode shapes of the disk–shaft system. As the disk is attached to the middle of the shaft, the mode shapes are symmetric (Fig. 5.10). Every two adjacent modes share the same natural frequency and the same mode shape.
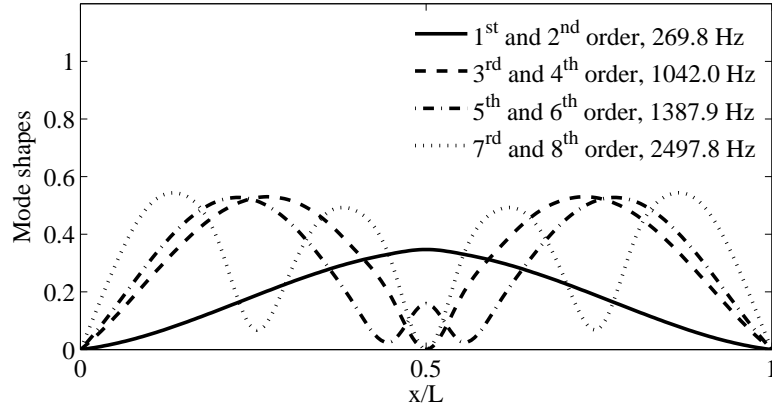
Figure 5.10: The first eight natural frequencies and mode shapes of the disk–shaft system

5.3.3 FSI Initial Condition Study

It will take a long time to reach the fully developed vibration status from an initially axisymmetric fluid field and an undeformed structure. In order to accelerate the vibration development, it is necessary to introduce some imbalance in the initial conditions in terms of the following:

1. Specify an eccentricity ec to the rotor disk;

2. Send the displacement to the fluid solver and deform the mesh;

3. Compute the non–axisymmetric fluid force F_f^{ec};

4. Remove ec.

However, in some cases, a dependency has been observed between final results and initial conditions. Since this relationship is apparently nonphysical, such initial conditions must be avoided. The causes of the dependency are as follows. First, a large eccentricity ec yields a large F_f^{ec}. Then, in the first FSI iteration of the first timestep, this leads to a large structural displacement d. Since the initial displacement is zero, a large d means large acceleration, which is equivalent to a large inertial force F_s^d in the structure. When F_s^d is too large, a problem occurs: from the next timestep on, the structural vibration is dominated by structural inertial forces rather than by fluid forces; in other words, it is no longer a real FSI analysis, and the calculated displacement will be too large. In sum, an appropriate initial condition requires ec to be adequate so that the fluid force dominates the vibration.

The arguments above are demonstrated in Fig. 5.11. The fluid forces received by the rotor in the FSI simulations are applied as loads in a finite element analysis

(FEA) of the rotor. It is expected that the structural displacements obtained by FSI and FEA are consistent. If the initial condition is proper, as shown in Fig. 5.11 (a), the FSI and FEA results are almost coincident. In contrast, if the initial condition is improper, i.e. ec is too large, as shown in Fig. 5.11 (b), the two sets of results deviate obviously, as the vibration obtained by FSI is not fully induced by fluid forces.
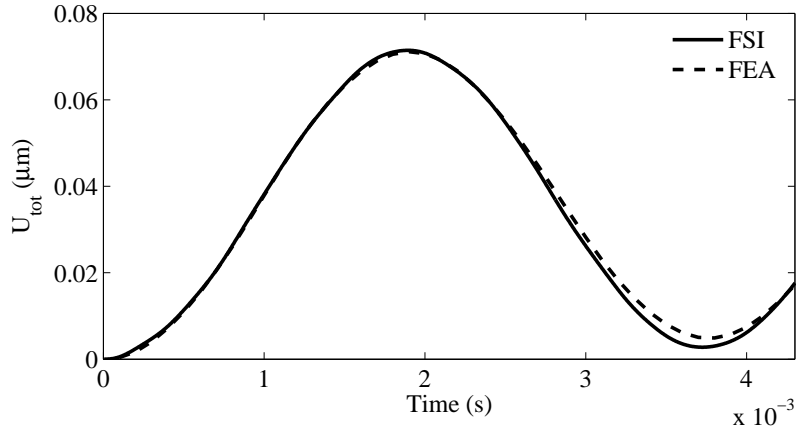
(a) Proper initial condition
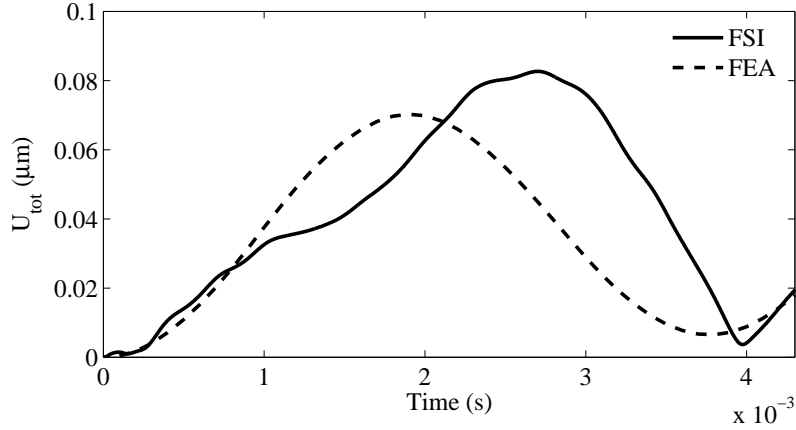
(b) Improper initial condition

Figure 5.11: Structural displacements obtained with FSI and FEA

Since F_f^d and F_s^d are unknown in advance, the recommended practice is to try various values of ec and determine the critical value. Any ec smaller than the critical value can serve as an appropriate initial condition. In this case, ec of 1% of the tip clearance and smaller lead to a constant amplitude (Fig. 5.12). Therefore, it is advised to start the trial from a small ec and then gradually reduce its value.
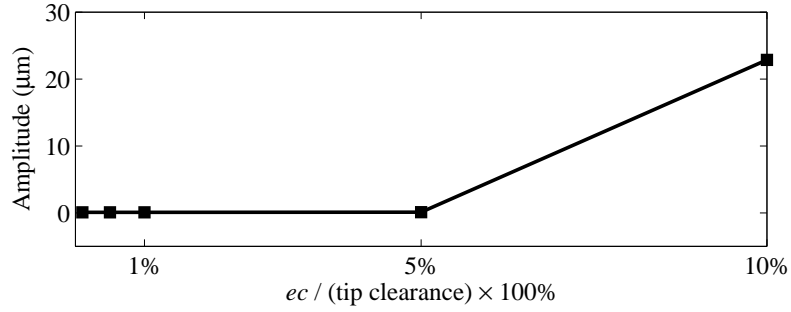
Figure 5.12: Influence of the magnitude of *ec* on the amplitude

5.3.4 FSI Amplitude Study

The deformed fluid domain and the mesh displacements are illustrated in Fig. 5.13. It can be seen that the displacements received from the rotor at the coupling surface are diffused into the inner domain.

Figure 5.14 shows the transient responses of the rotor displacement and the lift force on the coupling surface. A periodic vibration can be clearly recognized. The rotor vibrates at a frequency of 274 Hz, which is almost the same as its first–order natural frequency. The amplitude is about 0.03% of the tip clearance.
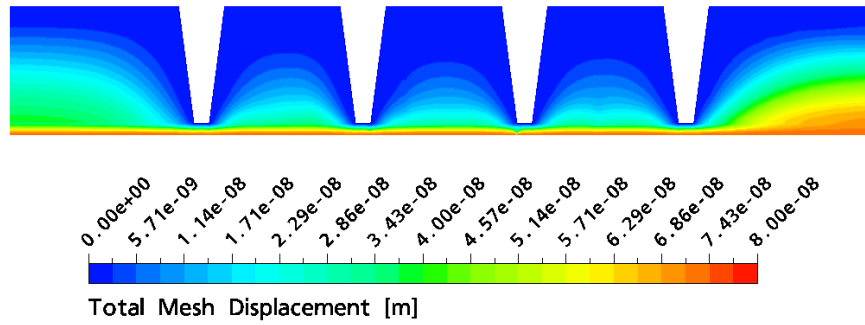
Figure 5.13: Mesh displacement distribution at a certain time ($\pi = 2.0$, $\dot{m} = 0.138$ kg/s)

The dependency of the amplitude on the pressure ratio π and mass flow $\dot{m}$ are shown in Fig. 5.15 and Fig. 5.16, respectively. In Fig. 5.15, $p_{stat,out}$ is fixed to the atmospheric pressure and $p_{tot,in}$ is varied to obtain various π. In Fig. 5.16, π is maintained at 2, whereas $p_{tot,in}$ and $p_{stat,out}$ are varied proportionally to obtain various $\dot{m}$. The amplitude increases linearly with π and $\dot{m}$. The maximum amplitude is about 0.05% of the tip clearance.
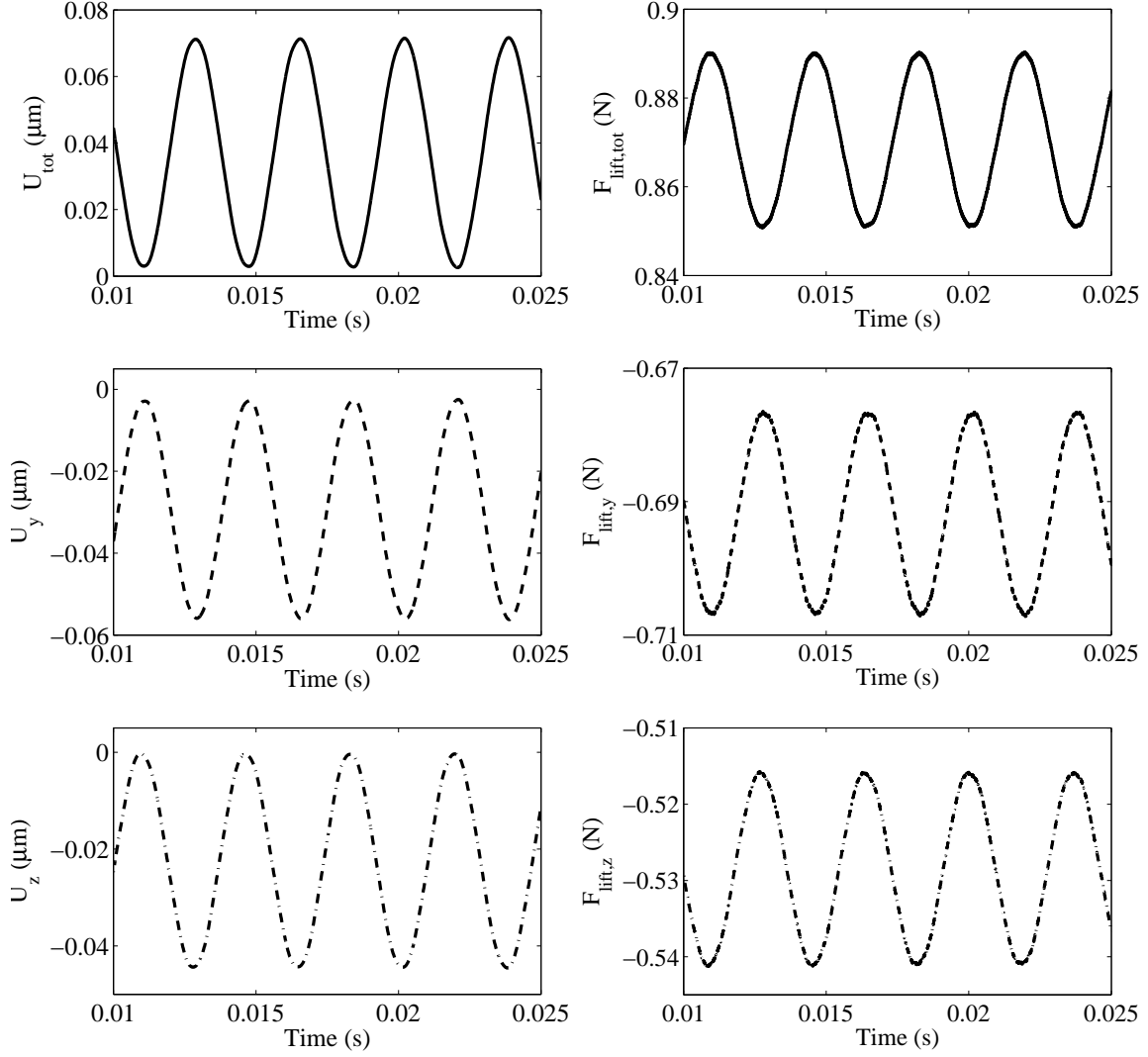
Figure 5.14: Displacement history (left) and lift force history (right) ($\pi = 3.8$, $\dot{m} = 0.088$ kg/s)

5.3.5   Discussion of the FSI Results

The rotor instability induced by fluid forces has been of great interest to turbo-machinery engineers. However, there are few experiments available for quantitative comparison. The reason for the lack of data has been pointed out by other researchers [17] that as the forces in labyrinth seals are rather small, only minimal experimental data is available for the comparison and validation of calculations. As compensation, it is demonstrated in this numerical work that the vibration is, as expected, completely caused by the fluid forces (Fig. 5.11).

To study the fluid force induced vibration, the two–way, transient, and 3D nature of the FSI simulations means that the computation is very expensive. The current
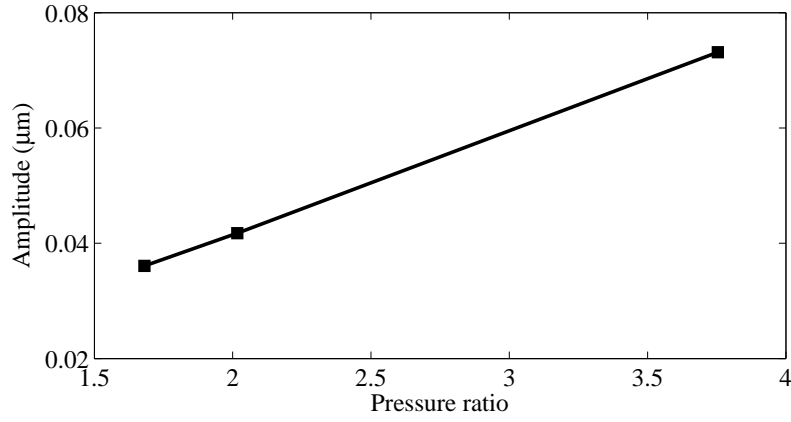
Figure 5.15: Influence of pressure ratio on the amplitude of rotor vibration ($p_{stat,out}$ = 101.325 kPa)
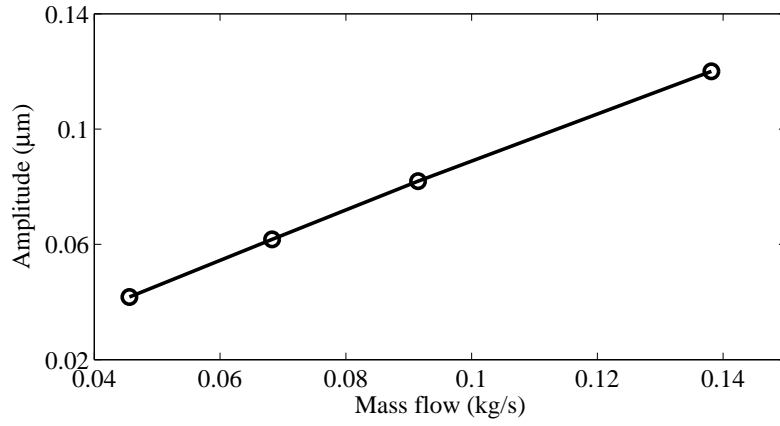
Figure 5.16: Influence of mass flow on the amplitude of rotor vibration ($\pi = 2$)

work is an attempt to apply the numerical simulation of FSI to labyrinth seals, given that employing FSI in industrial cases is now a trend, and the academia has been discussing about FSI in labyrinth seals for a long time. The purpose of this work is not necessarily to persuade all researchers to use FSI in labyrinth seals, but to provide experiences and some reference results. The methodology is established here, the dependency on initial conditions is explored, and the FSI simulations of the close–to–reality seal configuration reveal periodic vibrations of the rotor. The amplitudes turn out to be small, thus other researchers are well advised to consider the necessity of including such FSI effects into their numerical models.

In this study the rotor is modeled as a clamped–clamped beam with a disk, where bearings are omitted compared to a real rotor. Nevertheless, the most fundamental characteristics of a rotor are represented by the current model. Moreover, this simplified modeling helps to keep focus on the FSI implementation.

5.4 Summary

In this chapter, a 3D transient mechanical FSI study of a straight–through labyrinth seal is investigated. The fluid force induced vibration of the rotor is simulated by a two–way implicit coupling of the turbulent flow and the structure. Thus the structural displacements are obtained without rotordynamic models or other empirical assumptions, in which aspect exceeds single fluid or solid analysis.

Linear relationships between the vibration amplitude and pressure ratio/mass flow are well observed. The vibration frequency approximates the first–order natural frequency of the rotor. To excite the vibration more quickly, it is advantageous to use non–axisymmetric initial conditions. However, inappropriate initial conditions can lead to over–predicted amplitudes. Therefore, it is recommended to always conduct a prior dependency test. In addition, the vibrations are proved to be entirely induced by fluid forces instead of structural inertial forces.

The amplitudes computed using FSI are small. Considering that the seal design and operating conditions are based on experiments that are close to reality, it implies that the rotor vibration caused by fluid forces is not critical under the considered conditions.

The FSI procedure established in this chapter performs well for labyrinth seals and can be applied to the FSI simulation of entire turbines.

Chapter 6

FSI Case II – Thermal and Centrifugal Effects

In this chapter, the thermal and centrifugal effects of a 2D axisymmetric, high temperature, rotating stepped labyrinth seal is studied using two–way implicit FSI approaches.

This test case focuses on: 1) comparison between CFD and FSI predictions in respect of primary dimensionless numbers in labyrinth seals; 2) comparison of various FSI models; 3) heat transfer behavior across fluid–structure surfaces.

This chapter is organized in the following way. After introducing the fluid and the solid models, various FSI approaches with elastic/rigid structures for one–way/two–way coupling are defined. Then, both CFD and CSM models are verified and validated sufficiently. In the results and discussion section, flow features are shown in detail, followed by comparisons of various FSI approaches. After that, the optimal FSI models are chosen for further comparison with CFD simulations. Furthermore, the results of thermal FSI simulations are presented in terms of Nusselt numbers at the gas–rotor/stator interfaces and temperature/displacement distributions in the structures.

6.1   Numerical Models

Both fluid and structural models are based on room temperature rotating experiments done by Denecke et al. (2005) [4]. The test rig used in their experiments is shown in Fig. 1.3.

6.1.1   Fluid Field

In Fig. 6.1, the geometric parameters of the fluid domain are defined. Detailed settings of the CFD model are listed in Tab. 6.1. The outlet static pressure $p_{stat,out}$ is

kept constant, while the inlet total pressure $p_{tot,in}$ and total temperature $T_{tot,in}$ are varied. Nonadiabatic wall boundary conditions are applied in thermal FSI simulations. Turbulence models and mesh dependency will be discussed in more detail in section 6.2.1. The *automatic wall treatment* for SST turbulence model enables an automatic switch from low–Re near–wall formulations to wall functions. Thus, it allows a flexible grid resolution near the wall. Nevertheless, y^+ is maintained below 1 at most locations. The convergence criteria are similar to case I, except that the imbalance criterion is more rigorous and more global variables are monitored (see section 6.2.1). The false timestep size in steady–state simulations can reach a maximum of 10^{-5} s without causing instability. Since the numerical model is axisymmetric, one element is used in circumferential direction.
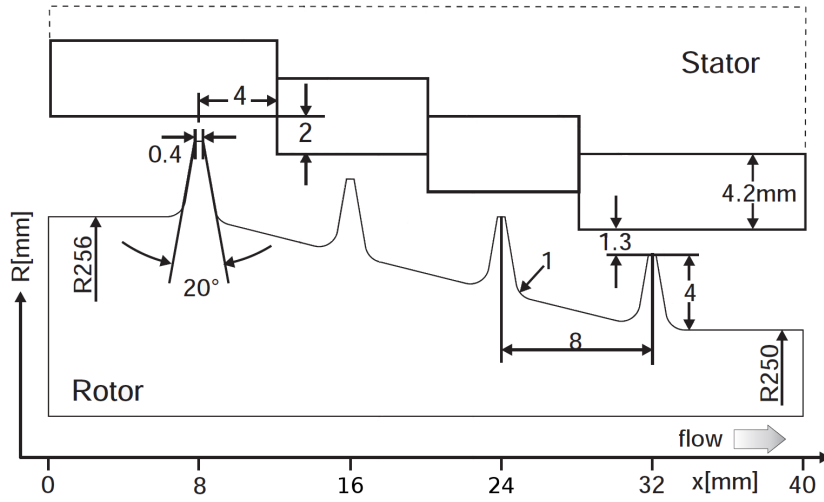
Figure 6.1: Stepped labyrinth seal geometry (Denecke et al., 2005)

6.1.2   Rotor and Stator

In experiments, both rotor and stator consist of titanium alloy. In accordance, the titanium alloy Ti6Al4V, which is commonly seen in aeronautics, is applied in this study. Thermal property dependencies on temperature are shown in Tab. 6.2. In addition, the mean coefficient of thermal expansion (CTE) is chosen.

Both rotor and stator are modeled using the second–order 3D coupled–field element, *SOLID*226. Each node has four DOFs: structural displacements U_x, U_y, U_z, and temperature T. The centrifugal effect is also enabled for this element type.

In the model, both mechanical and thermal boundary conditions (Fig. 6.2) are set close to experiments. Axisymmetric conditions are specified at the front and back surfaces. The upper end of the stator and the lower end of the rotor are clamped

Table 6.1: Description of the CFD model

Fluid type	Air, ideal gas
Boundary conditions	Inlet: various $T_{tot,in}$, $p_{tot,in}$
	Outlet: $p_{stat,out} = 2 \times 10^5$ Pa
	No–slip smooth walls
Turbulence model	SST with *automatic wall treatment*
Convection scheme	*High resolution* (second–order)
Convergence criteria	RMS residuals of all conservation equations $< \varepsilon$
	Imbalances of mass, momentum, and enthalpy $< 0.1\%$
	Global variables do not change over iterations
False timestep size	10^{-5} s
Mesh	2D axisymmetric
	102,000 hexahedral elements

and set at 288 K in order to generate a temperature gradient across the rotor and the stator for the heat transfer calculations. The left and right boundaries of the stator are insulated. All surfaces of the rotor, other than the FSI interface and the lower end, are immerged in cooling air, and are modeled as convective walls with a heat transfer coefficient (film coefficient) of 50 W/m^2 K and a surrounding fluid temperature (bulk temperature) of 288 K [103].

Table 6.2: Material properties of the rotor and stator

Material properties	300 K	600 K
Thermal conductivity	7.3 W/m K	10.9 W/m K
Specific heat capacity	560 J/kg K	640 J/kg K
Secant thermal expansion	8.6×10^{-6} /K	9.2×10^{-6} /K
Density	4430 kg/m^3	
Young's modulus	1.138×10^{11} Pa	
Poisson's ratio	0.342	
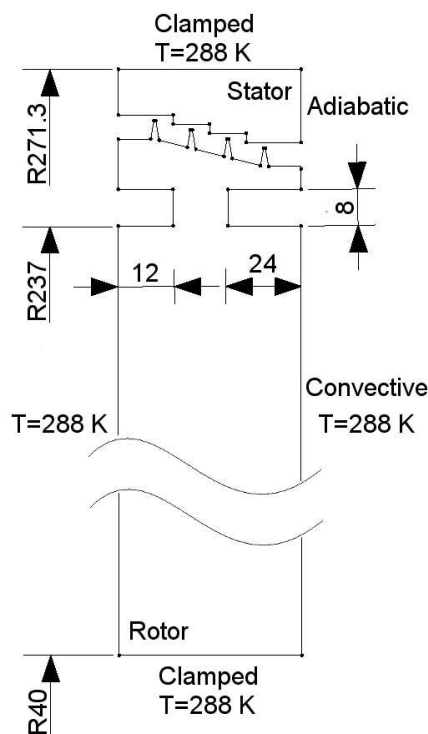
Figure 6.2: Geometry and boundary conditions of the rotor and stator (mm)

6.1.3   FSI Models

FSI variables are exchanged at the fluid–rotor and fluid–stator interfaces shown in Fig. 6.3. The coupling variables include mechanical quantities, i.e. displacement and force, as well as thermal quantities, i.e. temperature and heat flow. Table 6.3 shows detailed settings of the coupling variables.

Four different FSI models are employed here. They are distinct from each other in terms of FSI effects and coupled variables. A brief overview is given in Tab. 6.4. Two models are designed to study the thermal FSI effects (TFSI), while the other two focus on the centrifugal FSI effects (CFSI). Furthermore, the two TFSI models differ in their structural coupling behavior. In a TFSI analysis with rigid structure, only thermal variables are coupled. Such approach is also known as Conjugate Heat Transfer (CHT) as available in some CFD software. In contrast, the TFSI model with elastic structure couples mechanical variables in addition to thermal ones and is hence more realistic. In both one–way and two–way CFSI models, only mechanical quantities are exchanged. They are distinguished from each other by including or excluding the influence of fluid forces on the structure. Compared to the one–way model, which is equivalent to running a structural finite element analysis and deforming the fluid domain accordingly, the two–way model is more representative of the reality. Similar

approaches can be found in some CFD studies, where the fluid mesh is modified in order to account for the rotation induced inertial effects of the structure [104]. However, averaged structural displacements are usually used in such studies other than actual local deformations, in order to relieve the mesh modification. It is also worth to point out that, in comparison to the method of accounting for the centrifugal displacements by modifying the fluid domain, the CFSI model saves the effort of altering the geometry and remeshing, which can be extremely expensive for complex geometries and non–uniform centrifugal deformations.

In the present work, steady FSI simulations are applied for parameter studies.

The fluid mesh is deformed using the *increase near small volumes* mesh stiffness model with $C_{stiff} = 0.5$ and RMS $< 10^{-4}$. It is also checked that variations of the mesh stiffness model and C_{stiff} value have little influence on the results. A deformed mesh and the local mesh distortion are shown in section 6.3.2.
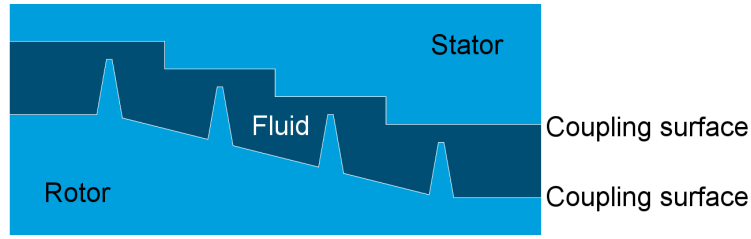
Figure 6.3: FSI coupling surfaces

Table 6.3: FSI coupling variables

Coupling variable	Displacement (DISP)	Temperature (T)	Force (F)	Heat flow (HF)
Under–relaxation factor	0.1	0.1	1.0	0.1
Transfer direction	Solid $\rightarrow$ fluid		Fluid $\rightarrow$ solid	
Interpolation scheme	*Profile preserving*		*Conservative*	
FSI convergence criterion	10^{-3}		10^{-3}	

6.2 Verification and Validation

In this section, the fluid model is verified and validated with respect to turbulence models and meshes. Velocity profiles and various dimensionless numbers show good agreements with test data. The centrifugal and thermal responses of the structural model are also well validated. The experimental results are obtained from the dissertation of Denecke (2007) [1].

Table 6.4: Various FSI models

FSI effect	Abbreviation	Sub–model	Coupled variables
Thermal	TFSI	Rigid structure	T, HF
		Elastic structure	T, HF, DISP, F
Centrifugal	CFSI	One–way	DISP
		Two–way	DISP, F

6.2.1   Fluid Model

First, various turbulence models are validated. Compared to case I, the fluid domain of the current stepped labyrinth seal is more complex. It is known that the standard $k - \varepsilon$ is less accurate when there are flow separation and recirculation [105]. In Fig. 6.4, the results using standard $k - \varepsilon$, RNG $k - \varepsilon$, and SST are compared with respect to the discharge coefficient at growing pressure ratio. It is shown that both SST and RNG $k - \varepsilon$ lead to less than 3% deviation from the test results, and the former is slightly better. Therefore, SST, which is widely acknowledged for predicting flows with separation, is applied in the following study.
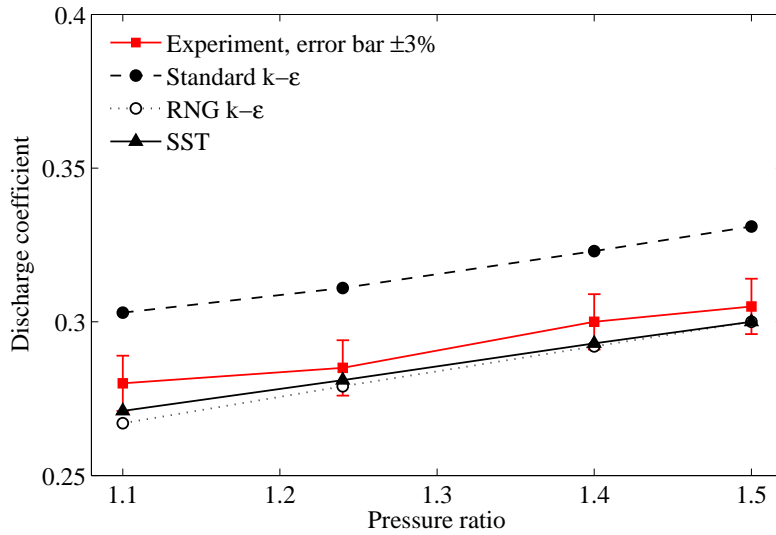
Figure 6.4: Validation of various turbulence models regarding leakage prediction (non–rotating, $T_{tot,in} = 300$ K)

Similar observations can be found in [26]. Wang et al. (2004) used three alternative $k - \varepsilon$ models to predict leakage in stepped labyrinth seals: the standard $k - \varepsilon$ and its two variants, RNG $k - \varepsilon$ and realizable $k - \varepsilon$. The predictions based on RNG $k - \varepsilon$

and realizable $k - \varepsilon$ are found to be in good agreements with the measurements with less than 3% discrepancies, whereas the predictions obtained using standard $k - \varepsilon$ have larger gaps.

Second, the mesh is validated. Since SST uses low–Re formulations at walls, the near–wall grid resolution should be sufficiently fine. In the mesh dependency study, y^+ is kept below 2 at all locations. The influences of the mesh density on the discharge behavior, windage heating, and outlet swirl are plotted in Fig. 6.5. All numerical results are within experimental uncertainties. The dimensionless numbers are rather insensitive to the mesh resolution. The mesh of medium density is finally chosen for the rest of the studies (Fig. 6.6).
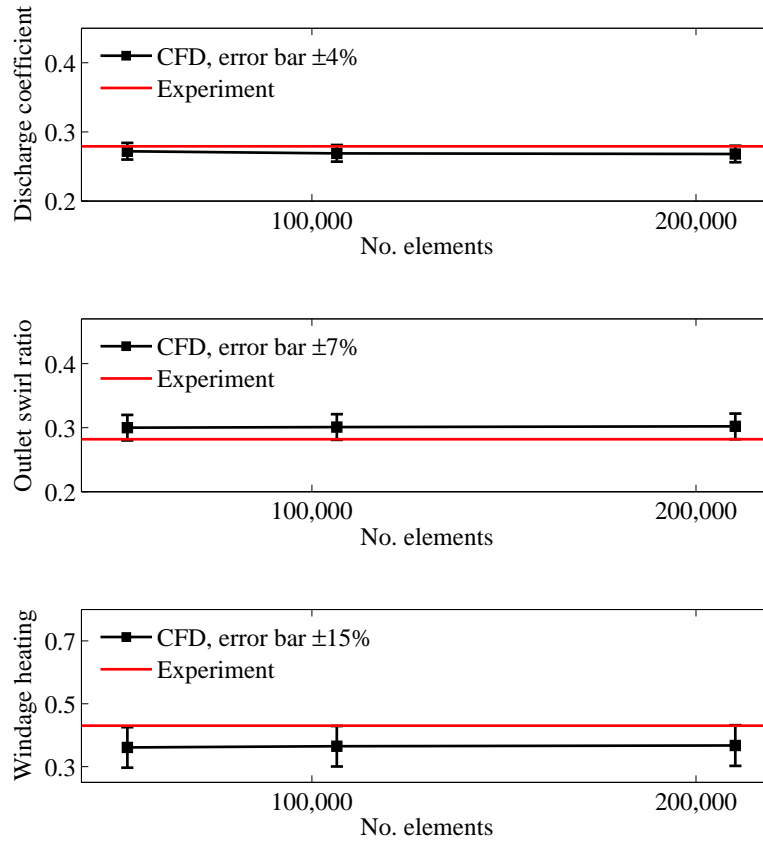
Figure 6.5: Mesh dependency study of the fluid model with respect to discharge coefficient C_D, outlet swirl ratio K_{out}, and windage heating coeeficient σ ($\pi = 1.05$, $n = 6{,}000$ rpm, $T_{tot,in} = 300$ K)

As one of the convergence criteria, the changes of critical global variables must be within a given tolerance. The convergence history of mass flow, outlet circumferential velocity, and outlet static temperature are shown in Fig. 6.7. All curves become flat as the solution converges.
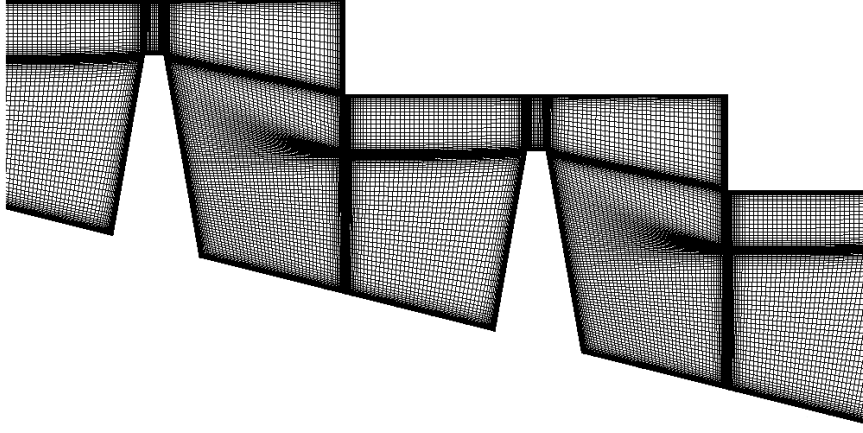
Figure 6.6: Validated mesh for the SST turbulence model

(a)   (b)   (c)
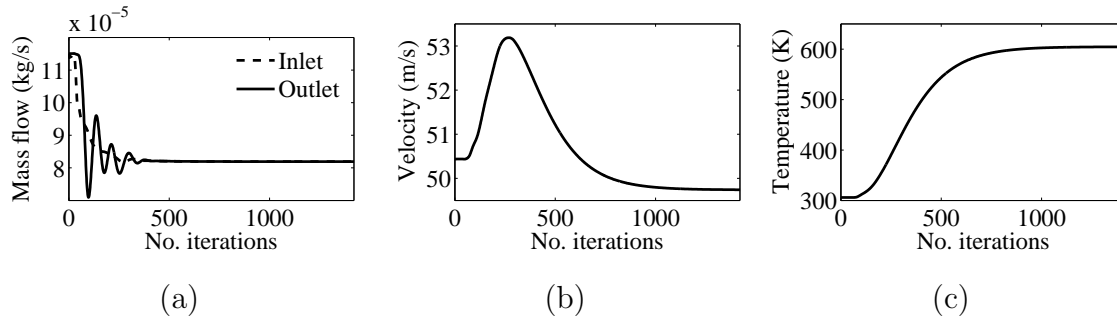
Figure 6.7: Convergence history of critical variables: (a) mass flow; (b) circumferential velocity at the outlet; (c) static temperature at the outlet

Based on the validated turbulence model and mesh, velocity profiles at $x = 3$ mm, upstream of the first tooth, are compared with test results. Figure 6.8 shows the distribution of dimensionless axial and circumferential velocity along radial direction. The actual velocities are divided by the rotor surface speed, while the radial position is normalized by the channel height. Clearly, the simulation results and test measurements are in excellent agreement.

Finally, the windage heating coefficient is validated against test results under growing circumferential Mach number (see Eq. 2.8) at given pressure ratio and inlet total temperature (Fig. 6.9). The inlet total temperature is used instead of the local temperature to calculate the speed of sound in Eq. 2.8, so that the circumferential Mach number is actually proportional to the rotational speed. Since the measurement uncertainty is about 20% according to reference [4], the numerical results are well validated despite the discrepancy. In addition, the present numerical study is compared with the CFD study done by Denecke et al. (2005) [4]. Although different CFD codes, turbulence models, and meshes are used in the two studies, the present
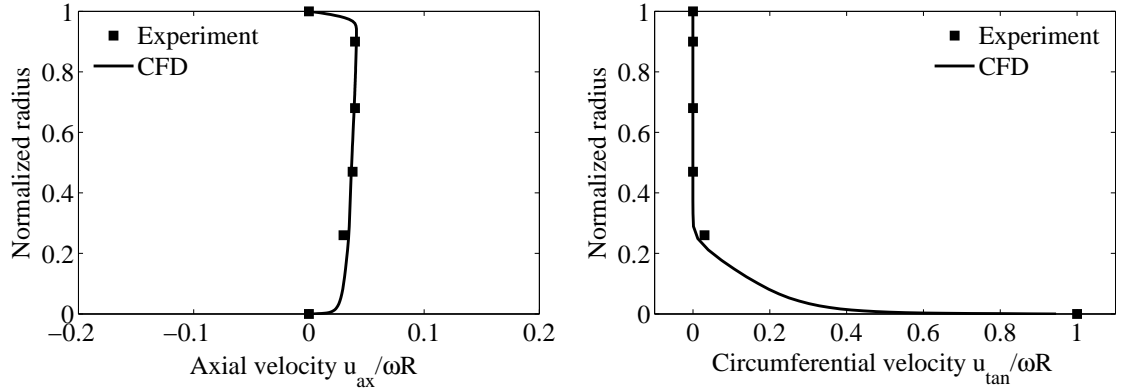
Figure 6.8: Axial and circumferential velocity profiles at $x = 3$ mm ($\pi = 1.05$, $n = 6{,}000$ rpm, $T_{tot,in} = 300$ K)

results and Denecke's results are close to each other.

In their experimental study [4], Denecke et al. explained that the measurement uncertainty is mainly due to the radial seals installed at the entrance and the exit of the stepped labyrinth seal, which act as an undesired heat source. Such parasitic heat entrains the rotor and can account for up to 20% of the total temperature rise measured across the seal at current pressure and temperature conditions. Moreover, the total temperature increases only about 10 K, the small magnitude of which further elevates the percentage uncertainty. Last but not least, the temperature was measured at one single point, while the numerical results are averaged over the channel height.

6.2.2 Structural Model

In the model, the centrifugal growth is validated by comparing the radial displacement of the second tooth with experimental results at growing rotational speed (Fig. 6.10). The FEA predictions show good agreement with measurements. Moreover, comparing the displacements of various teeth shows a uniform centrifugal growth of the rotor.

There is few experimental data available to validate the thermal response of the coupled model. Instead, a simplified theoretical model is introduced as analytical reference. Compared to the rotor shown in Fig. 6.2, the rotor in the theoretical model is represented by a rectangular block, where the throat and the teeth are omitted. Presuming a temperature gradient from top to bottom, the thermal expansion of the block can be calculated analytically. The solution is then compared with the numerical results based on the original rotor at various temperature gradients (Fig. 6.11). Good agreements have been found between the two sets of results.
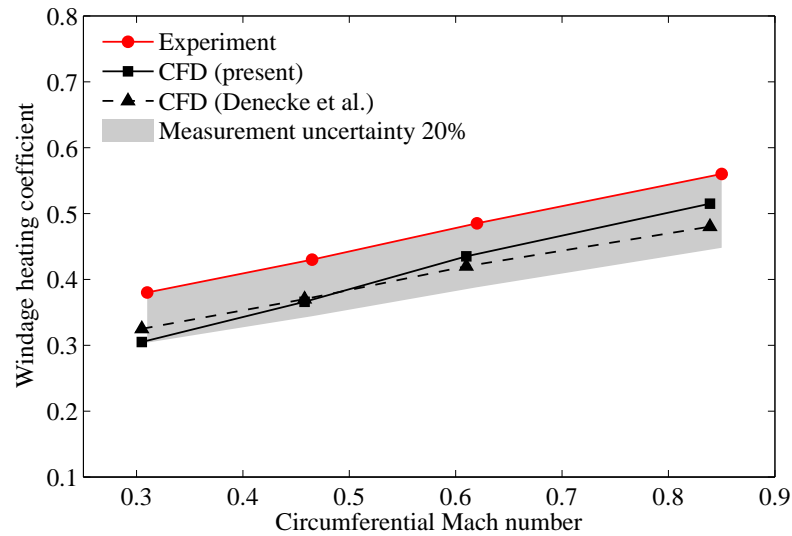
Figure 6.9: Validation of the fluid model with respect to windage heating prediction under various rotational speeds ($\pi = 1.05$, $T_{tot,in} = 300$ K)
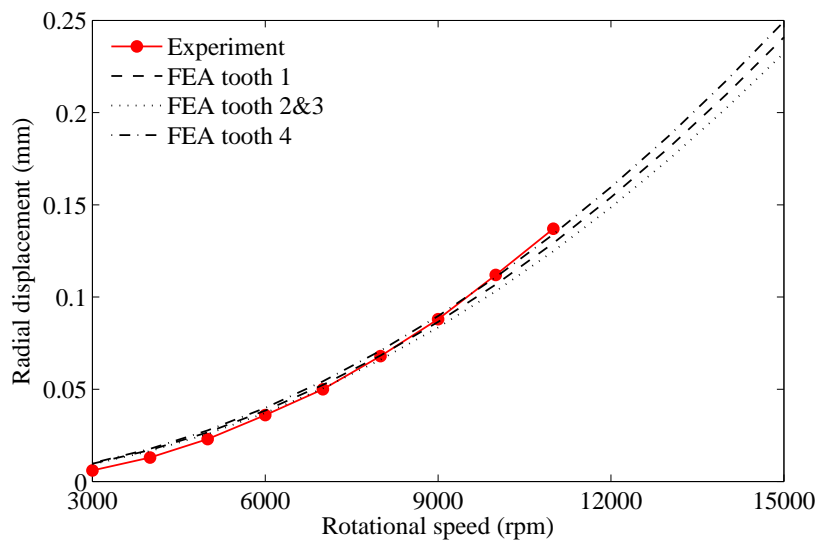
Figure 6.10: Radial centrifugal displacements at the rotor teeth obtained in experiments and finite element analysis

6.3   Results and Discussion

6.3.1   Flow Features

Detailed flow features are presented in Fig. 6.12. First, a large vortex between the teeth can be recognized in the axial–radial velocity vector field shown in Fig. 6.12 (a).
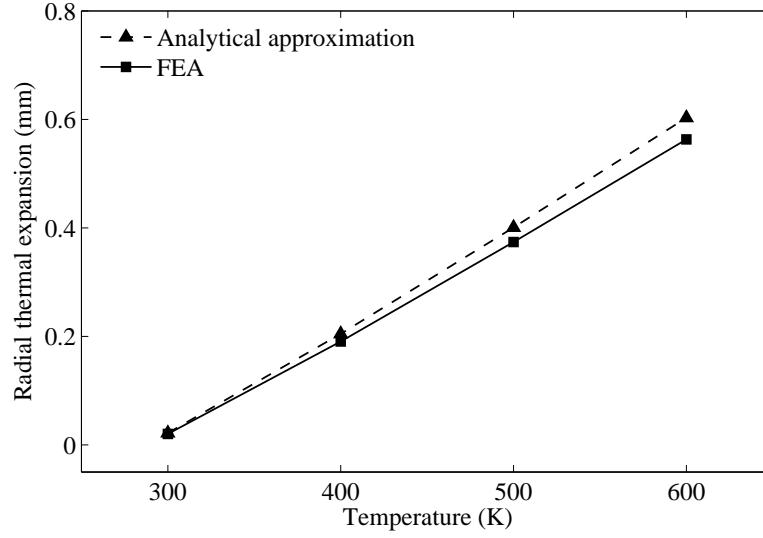
Figure 6.11: Radial thermal expansion of the rotor obtained by analytical approximation and finite element analysis

Above the vortex, there is a major and a secondary recirculation zone behind and in front of the step, respectively. Second, Fig. 6.12 (b) shows that the circumferential velocity increases from zero at the upper stationary wall to its maximum at the lower rotating wall. Third, the static temperature is raised across the seal as shown in Fig. 6.12 (c), which is mainly due to flow frictions. Last, it is found in Fig. 6.12 (d) that the static pressure decreases along the flow direction and varies very little within each cavity.

6.3.2 Comparison of Various FSI Models

Before comparing different FSI models, the mesh displacement of the fluid domain is shown in Fig. 6.13, where the lower boundary is moved upwards by 10% of the tip clearance. It demonstrates clearly that the deformation propagates from the boundary to the internal fluid domain and the mesh distorts most at tooth corners. A good mesh quality is preserved.

The major difference observed between one–way and two–way CFSI is the structural displacement, while the predictions for discharge coefficient, windage heating coefficient, and outlet swirl ratio are consistent. In Fig. 6.14 (a), the centrifugal growth of the fourth tooth is compared at various rotational speeds. It is found that the displacements obtained by two–way CFSI are a little smaller than that with one–way CFSI. In Fig. 6.14 (b), the deformed rotor profiles of one–way/two–way CFSI are compared. Specifically, the solid line denotes the profile by taking the average of

(a) Axial–radial velocity

(b) Circumferential velocity

(c) Static temperature

(d) Static pressure
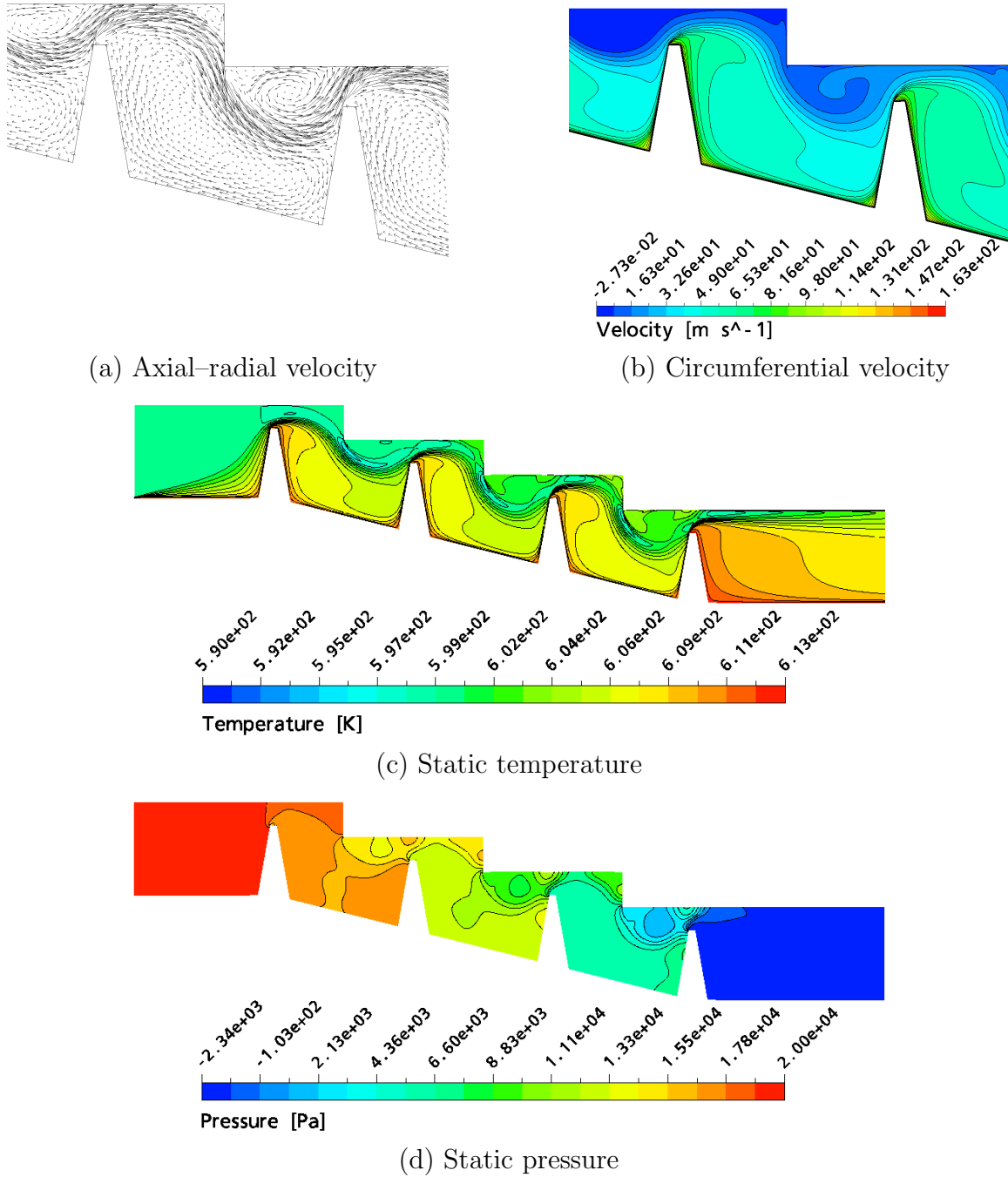
Figure 6.12: Flow features of the stepped labyrinth seal obtained using CFD simulations ($\pi = 1.1$, $n = 6,000$ rpm, $T_{tot,in} = 600$ K)

the displacements across the seal. This averaged value is used to deform the rotor uniformly, which is similar to the concept of fluid mesh modification used in some CFD studies of labyrinth seals [104]. Since both methods result in similar rotor deformations and require equivalent computational costs, they will be referred to as CFSI without further distinction in later sections.
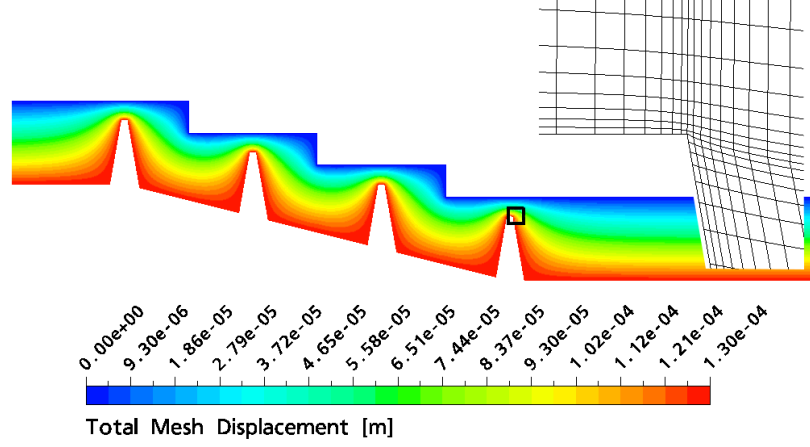
Figure 6.13: Mesh displacement distribution and local mesh distortion

(a) Displacement at the fourth tooth   (b) Deformation across the labyrinth seal
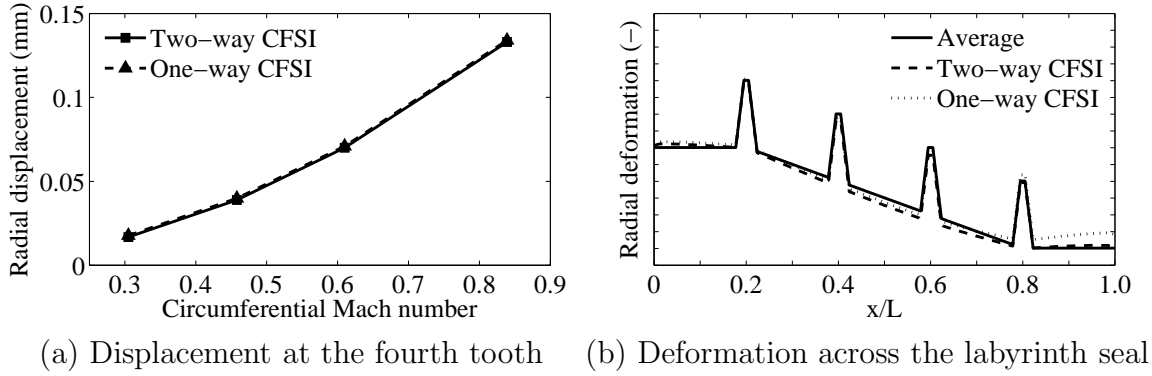
Figure 6.14: Comparison of the radial centrifugal displacement obtained with one–way/two–way CFSI ($\pi = 1.05$, $T_{tot,in} = 300$ K)
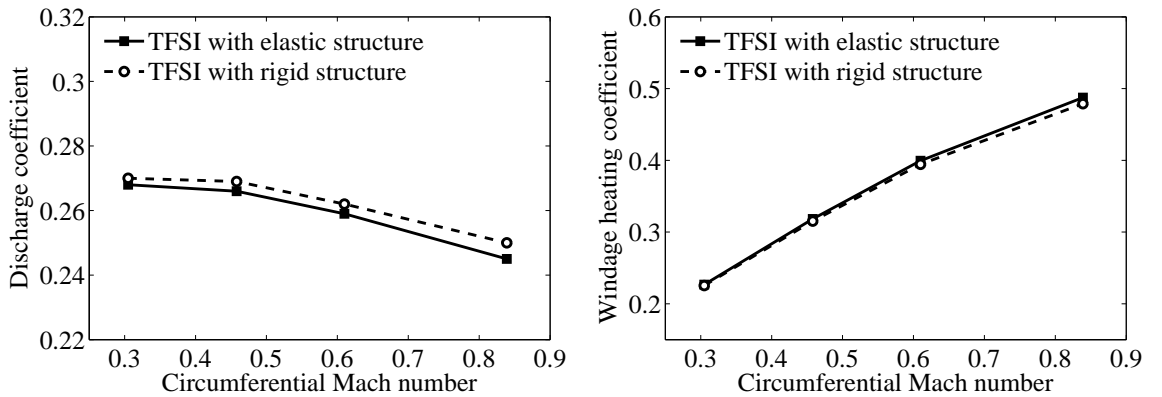
Figure 6.15: Comparison of the discharge coefficient and the windage heating coefficient obtained by TFSI with elastic/rigid structures ($\pi = 1.05$, $T_{tot,in} = 300$ K)

TFSI models with elastic/rigid structures are compared in Fig. 6.15, regarding discharge behavior and windage heating at growing rotational speed. Under given

pressure ratio and room temperature conditions, the two models lead to a difference of about 2% in discharge coefficient and a slighter difference in windage heating coefficient. In addition, their computational costs are comparable. Although TFSI with elastic structure is closer to reality, the rigid case (i.e. the CHT model) is more preferable in industrial applications for its simplicity. Therefore, both TFSI models will be further studied and compared.

6.3.3   Comparison between FSI and CFD

In this section, a series of parameter studies is conducted in order to compare FSI and CFD systematically. In particular, the structural displacement, temperature, and various dimensionless numbers are calculated using CFD and various FSI models at different pressure ratios, rotational speeds, and inlet total temperatures. Note that FSI models of coupled centrifugal and thermal effects can be obtained by superposition of CFSI and TFSI results, as indicated by numerical tests. In other words, the centrifugal thermal FSI result can be approximated by adding the corrections of CFSI and TFSI to the baseline CFD result and is therefore omitted in this study.

The influence of pressure ratio π at the rotational speed $n = 6,000$ rpm and inlet total temperature $T_{tot,in} = 300$ K/600 K is shown in Fig. 6.16. The radial displacement at the fourth tooth of the rotor is chosen to represent the rotor deformation. In comparison, the stator deformation is trivial and thus can be omitted. The tooth temperature is presented in two ways: 1) the static temperature at the first tooth is plotted against π; 2) the static temperature distribution across all the teeth is compared at various π.

First, the discharge coefficient C_D is plotted versus pressure ratio. To calculate C_D, the ideal mass flow (see Eq. 2.1) is always obtained from the undeformed tip clearance for CFD and FSI simulations. Therefore, the C_D here is also an indicator for the mass flow change due to the change of the tip clearance. C_D is found to increase with π, which accords with previous research. For both $T_{tot,in}$ conditions, the CFSI and the TFSI approach with elastic structure result in smaller C_D values than those from CFD calculations. This is mainly attributed to the reduction of tip clearance due to centrifugal growth and thermal expansions. Based on the parallel curves, the gap between CFSI and CFD predictions is independent of π, which can be explained by the constant change of tip clearance.Furthermore, it is found that C_D increases with $T_{tot,in}$ in CFD and CFSI cases, and decreases with $T_{tot,in}$ in TFSI cases with elastic structure. The cause of the former phenomenon is to be explored. At $T_{tot,in} = 600$ K, the thermal expansion becomes significant, and the TFSI with elastic structure yields the minimum C_D. In addition, results from the TFSI approach with rigid rotor agree well with results from CFD at low $T_{tot,in}$ and deviate at high $T_{tot,in}$.

Turning now to the windage heating coefficient σ, it indicates the total temperature increase across the seal due to the transfer of rotational speed from the disk to

the flow, which is a consequence of the near wall surface friction. As can be seen from the chart, σ decreases with the increase of π. Since the power input of the rotor is constant, the large mass flow due to large pressure ratio indicates less power per unit mass, which leads to a small total temperature increase. CFSI leads to slightly higher σ values than CFD at both $T_{tot,in}$ conditions. It is mostly due to the decrease in tip clearance and the consequent decrease in mass flow, which raises the power per unit mass, resulting in larger total temperature increase. Moreover, the CFD and CFSI curves of σ are parallel, which again suggests that the difference is not affected by π. The σ predicted by CFD and CFSI are smaller at high $T_{tot,in}$ than at low $T_{tot,in}$. Besides, when $T_{tot,in} = 300$ K, both TFSI models are coincident with each other and lead to a low σ, since the heat generated by flow friction is in part deducted by the solid. However, in TFSI simulations at high fluid temperature, the heat loss becomes so significant that the temperature decreases across the seal, and thus σ becomes negative, which makes it an improper measure of heat transfer.

The outlet circumferential velocity is measured by the outlet swirl ratio K_{out}. In general, K_{out} decreases with the increase of π. The reason for the decrease of σ also applies to K_{out}. Since less power is available per unit mass at high pressure ratios, the fluid acceleration is less significant in the circumferential direction. The results of TFSI simulations with elastic structure at high $T_{tot,in}$ deviate significantly from other results. This can be attributed to the tip clearance reduction. The fluid thus accelerates more in the circumferential direction owing to the rotating wall. In addition, the K_{out} values obtained by CFD, CFSI, and TFSI with rigid structure at high $T_{tot,in}$ are slightly smaller than those at low $T_{tot,in}$.

The radial displacement is caused by the centrifugal growth and thermal expansion. As shown in the chart, the centrifugal growth is larger than the thermal expansion at $T_{tot,in} = 300$ K. The thermal expansion dominates the radial displacement at $T_{tot,in} = 600$ K and leads to a slight increase of radial displacement at high π, because large pressure ratio results in large Reynolds number and thus large Nusselt number, which suggests that more thermal energy enters the structure.

According to the numerical results, the tooth temperatures happen to equal the static temperature of the fluid at the tooth tips. Different trends are recognized for different models. In both $T_{tot,in} = 300$ K and 600 K cases, it is observed that the tooth temperature decreases with π in the CFD model, but increases in TFSI models. The former can be explained by the increase of Mach number, while the latter can be attributed to the heat transfer inside the rotor. It is also worth to point out that at $T_{tot,in} = 600$ K, the results from TFSI models are evidently lower than those from CFD and CFSI, as the heat is partially absorbed by the solid. It can be seen from the last two charts in Fig. 6.16 that the temperature decreases consequently from tooth 1 to 4 in TFSI models. However, in CFD and CFSI cases, the temperature stays almost constant at various teeth. The effects of π on tooth temperatures are also demonstrated in these two charts.
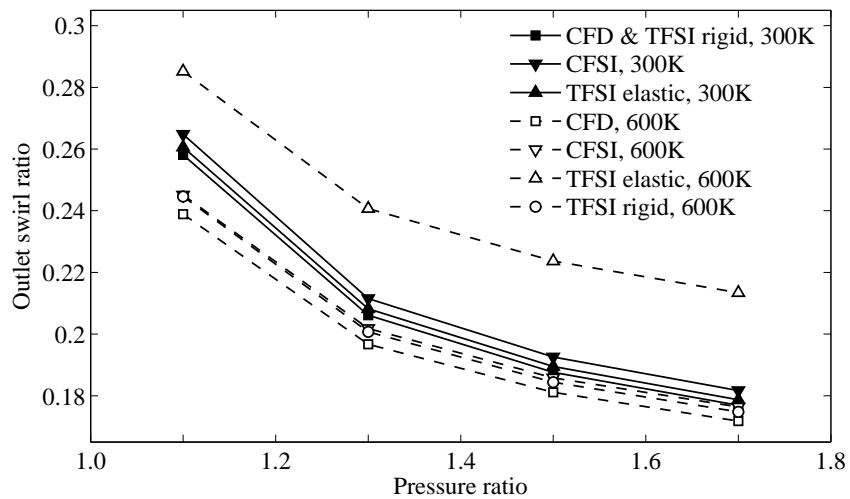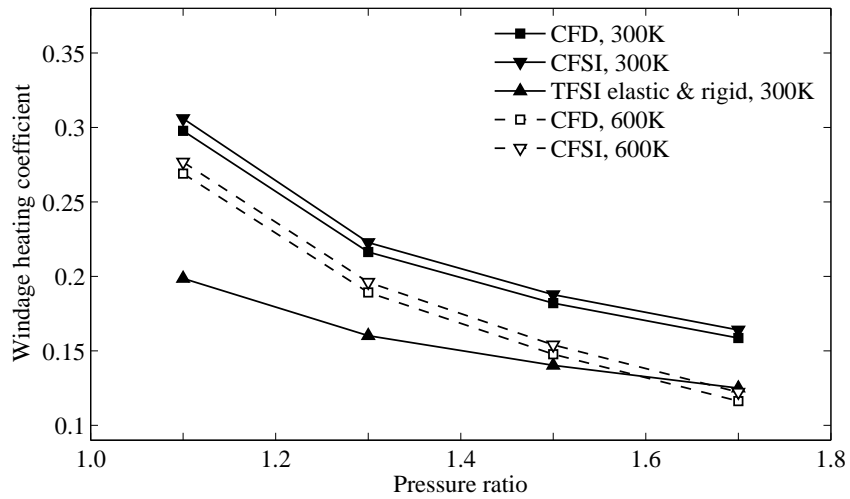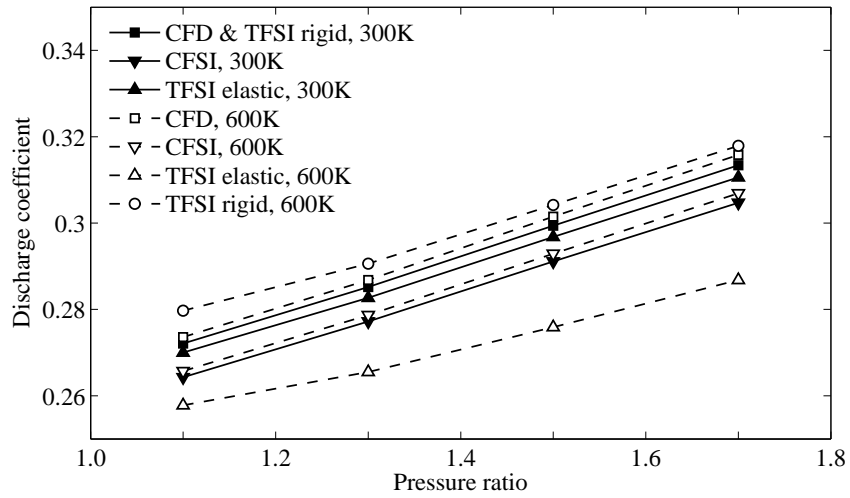
(continues on the next page)

Figure 6.16: Influence of pressure ratio on discharge coefficient, windage heating coefficient, outlet swirl ratio, rotor deformation, and tooth temperature ($n = 6{,}000$ rpm, $T_{tot,in} = 300$ K/600 K)

Figure 6.17 shows the impacts of the circumferential Mach number M_{tan} considering $\pi = 1.5$ and $T_{tot,in} = 300$ K/600 K. Note that M_{tan} is an indicator of the rotational speed.

As shown in the first chart, M_{tan} does not affect C_D in either CFD or TFSI simulations with rigid structure. However, when using the CFSI model, there is a significant decrease in C_D as M_{tan} increases. The main reason is that at high rotational speed, the tip clearance reduces as the centrifugal growth increases. Likewise, the slight decrease in C_D at high M_{tan} using the TFSI method with elastic structure is attributed to the increases of power input, which leads to the increase of fluid total and static temperatures, i.e. larger thermal expansions. Similar trends are observed as those found in the pressure ratio study above. Besides, the minimum C_D values always occur in TFSI models with elastic structure due to the significant thermal expansions.

The chart below shows that σ increases with rotational speed. It can be explained as follows. On the one hand, the power input of the rotor increases with rotational speed. On the other hand, the mass flow either remains constant or decreases. Thus, the power per unit mass increases, leading to higher total temperature increase. σ predictions of CFD and CFSI models at high fluid temperature are larger than those at low fluid temperature. TFSI results are smaller than CFD and CFSI results, which agrees well with the relative behavior from the pressure ratio study. However, the curves of CFD and CFSI are not parallel, since the tip clearance in CFSI simulations is affected by the rotational speed.

K_{out} increases with M_{tan} as expected. Furthermore, the TFSI model with elastic structure at high $T_{tot,in}$ yields the maximum K_{out} values. At low rotational speeds, all models except TFSI with elastic structure result in almost identical K_{out}. As the rotational speed increases, the results deviate from model to model and the second largest K_{out} is found to associate with the CFSI case.

It can be seen from the chart of the radial displacement, that the centrifugal growth increases with M_{tan} as one expects. In contrast, the thermal expansion increases slightly with the rotational speed, which supports the explaination above for the decrease of C_D. This finding is consistent with the literature, where Waschka et al. (1992) [7] showed quantitatively that the clearance decreases with increasing rotational speed, while the thermal expansion is less sensitive to the rotational speed.

Unlike the weak influence of the pressure ratio, as the rotational speed increases, the flow frictions also magnify and lead to significant increase of tooth temperatures in all cases. At low $T_{tot,in}$, results are consistent among different models. However, at high $T_{tot,in}$, the tooth temperatures predicted by both TFSI models are obviously lower than by the other models due to the heat loss from fluid to solid. The tooth temperature distribution across the seal does not vary much at $T_{tot,in} = 300$ K for all models, while distinguishable lower values for both TFSI models are found at $T_{tot,in} = 600$ K.
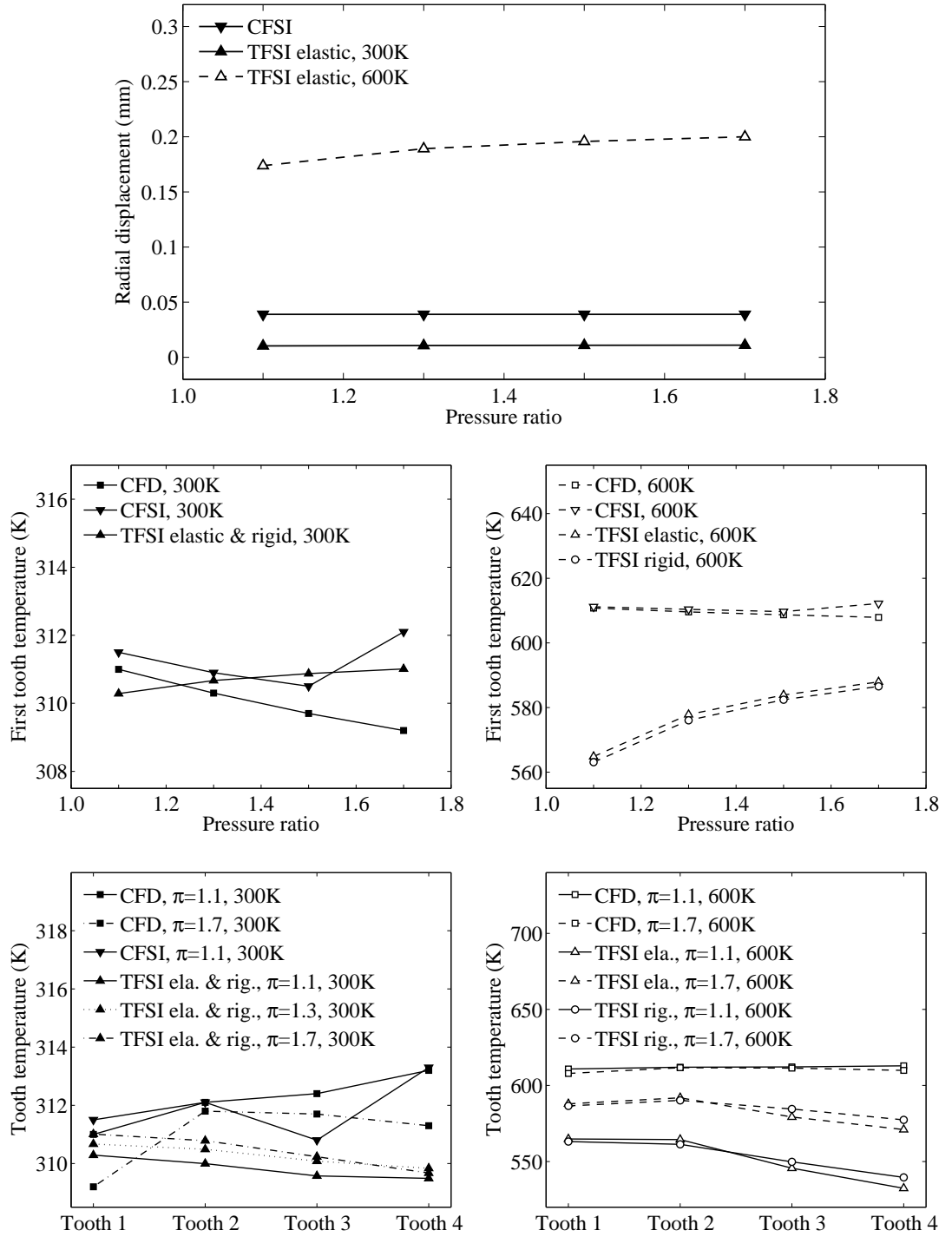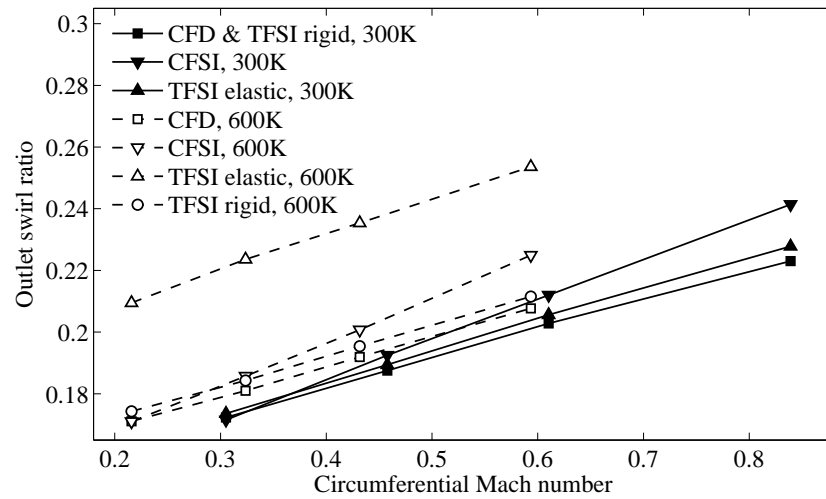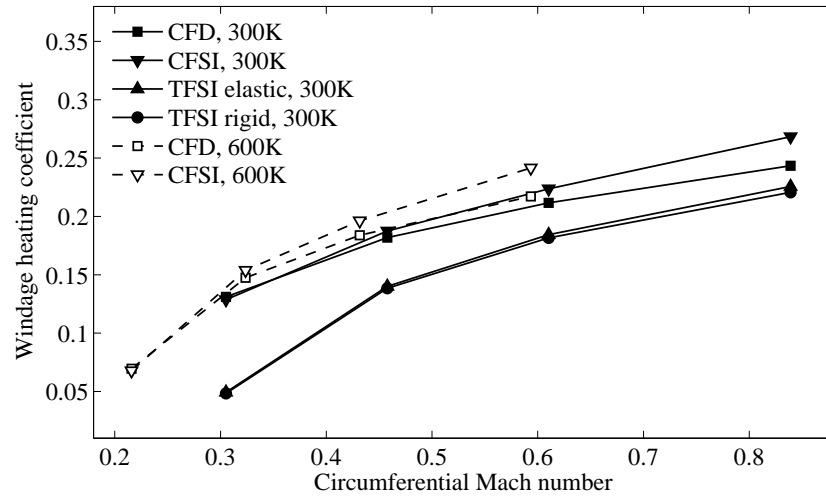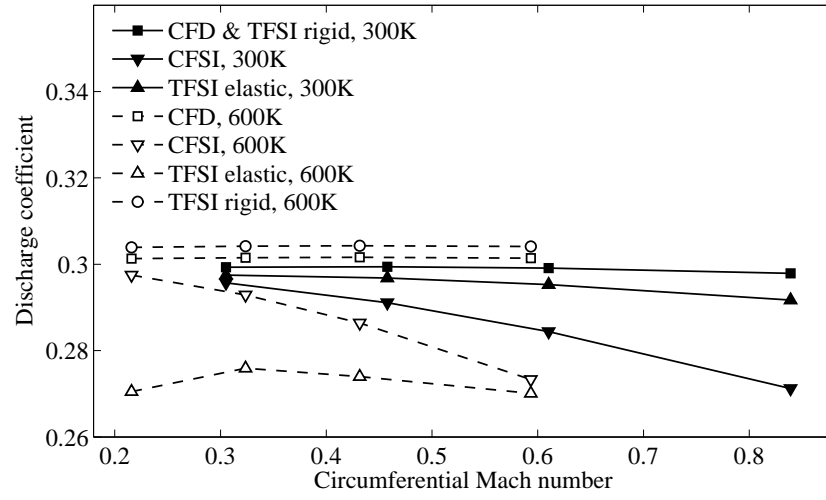
(continues on the next page)

Figure 6.17: Influence of rotational speed on discharge coefficient, windage heating coefficient, outlet swirl ratio, rotor deformation, and tooth temperature ($\pi = 1.5$, $T_{tot,in} = 300$ K/600 K)

Figure 6.18 presents the influence of the inlet total temperature $T_{tot,in}$ at modest conditions of π and n.

The chart of C_D versus $T_{tot,in}$ shows that the C_D predicted by CFD, CFSI, and TFSI with rigid structure increases slightly with $T_{tot,in}$, whereas the C_D predicted by TFSI with elastic structure decreases obviously with the increase of $T_{tot,in}$ due to reduced tip clearances. The relationships among various models are in agreement with earlier studies. Moreover, it is apparent that there is a growing deviation between TFSI with elastic structure and CFD at increasing $T_{tot,in}$.

There is a clear trend of decreasing σ as $T_{tot,in}$ rises. Both the real mass flow and the power input decrease with $T_{tot,in}$, where the reduction of power input is due to the decreased fluid density [42]. However, the cause of the windage heating reduction is still to be explored. Further experimental and numerical research on windage heating at high temperatures is expected. The curves of CFD and CFSI are parallel, indicating that the difference between the two models is independent of $T_{tot,in}$.

The outlet swirl ratio increases significantly with $T_{tot,in}$ in TFSI simulations with elastic structure and decreases slowly in other simulations. Again, the reduction of tip clearances explains the former case.

The radial displacements calculated by CFSI are independent of $T_{tot,in}$, as the centrifugal growth is irrelevant to fluid temperatures. At the same time, the radial displacement predicted by TFSI, i.e. the thermal expansion, increases with $T_{tot,in}$.

The tooth temperature increases with $T_{tot,in}$ for all models. Moreover, the increase is flattened a little when using the TFSI models due to heat losses of the fluid. The tooth temperature distribution varies a little bit across the seal. At $T_{tot,in} = 300$ K, results from different models can hardly be distinguished. However, at $T_{tot,in} = 600$ K, TFSI predictions depart from CFD/CFSI predictions. Finally, at $T_{tot,in} = 800$ K, one can observe the difference between two TFSI models.

To summarize, it is shown that results from CFD, CFSI, and TFSI models can be either similar or deviated, depending on the variable of interest and the operating condition. Generally, FSI models with elastic structures can better represent the real physics and thus result in more accurate predictions, especially at high temperature and high rotational speed. However, in the cases where FSI effects are less critical, CFD models can still be safely adopted. In brief, the systematic comparison above helps to choose the most appropriate model for the specific case.

6.3.4 Heat Transfer across Fluid–structure Surfaces

This section focuses on the heat transfer across the fluid–solid interfaces. TFSI models with elastic/rigid structures are both applied and compared.

Figure 6.19 illustrates the structural temperature field and radial thermal expansion at $T_{tot,in} = 300$ K and 600 K. It can be recognized that the rotor temperatures are obviously higher than the stator temperatures due to power input, which elevates
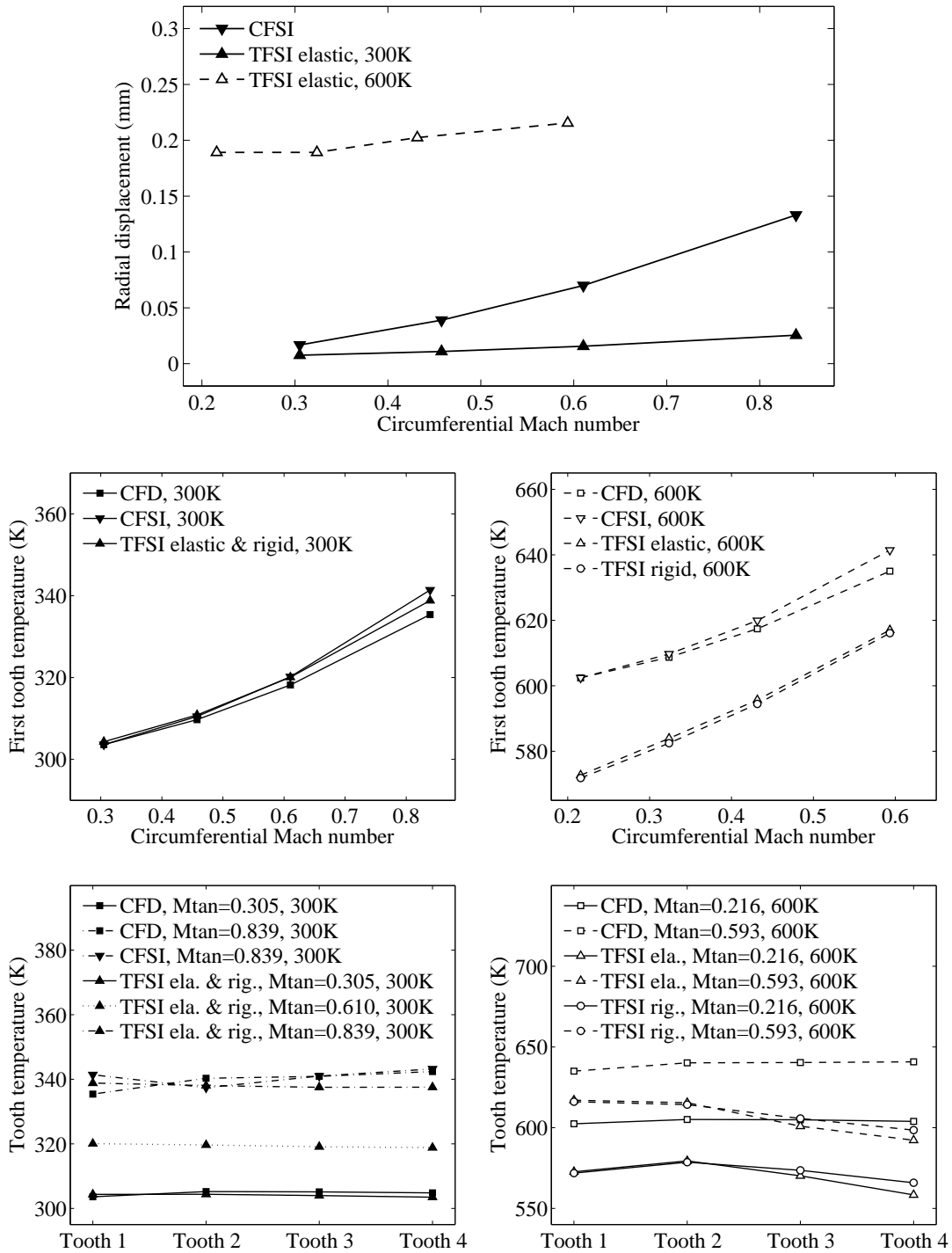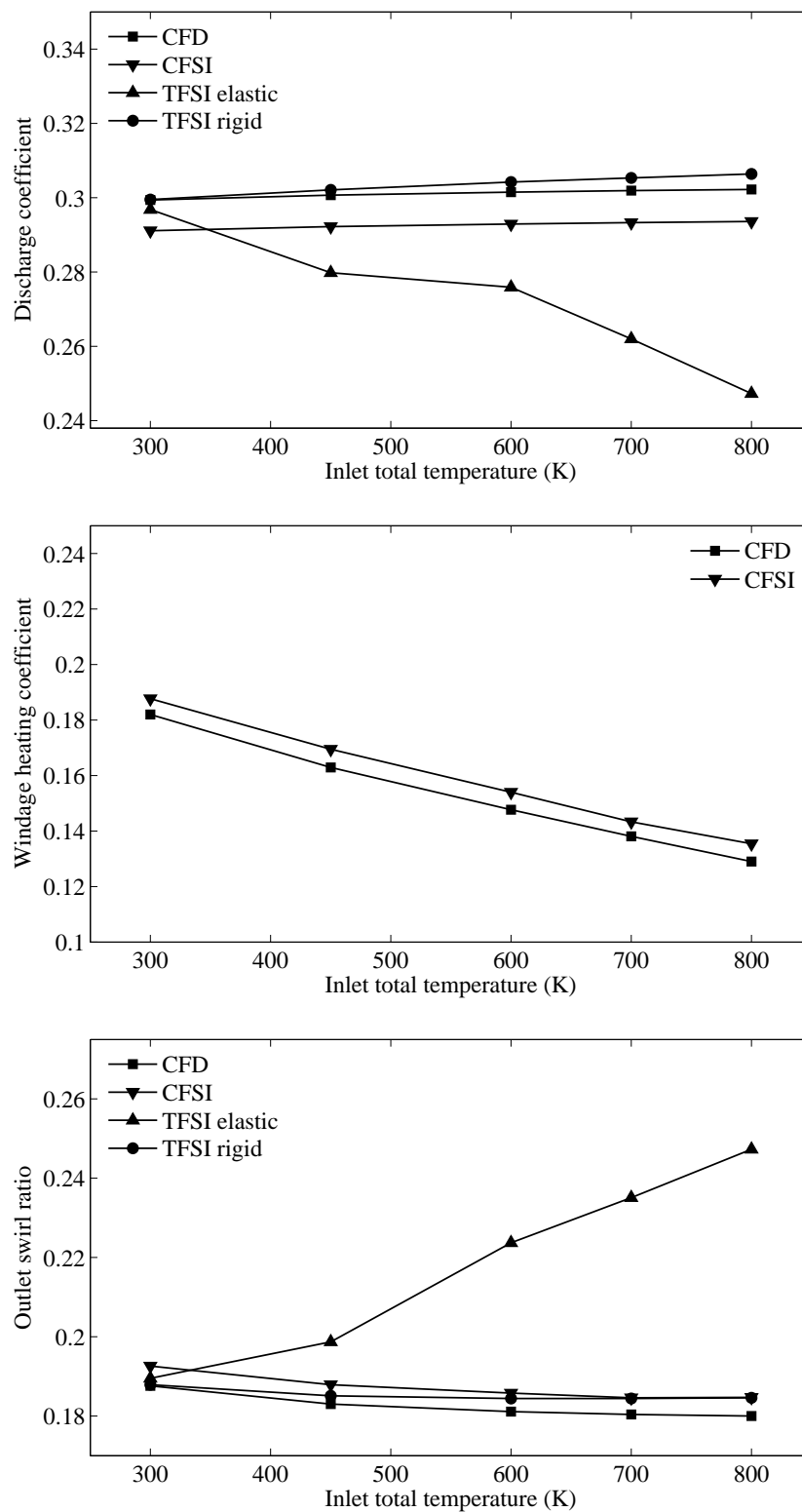
(continues on the next page)
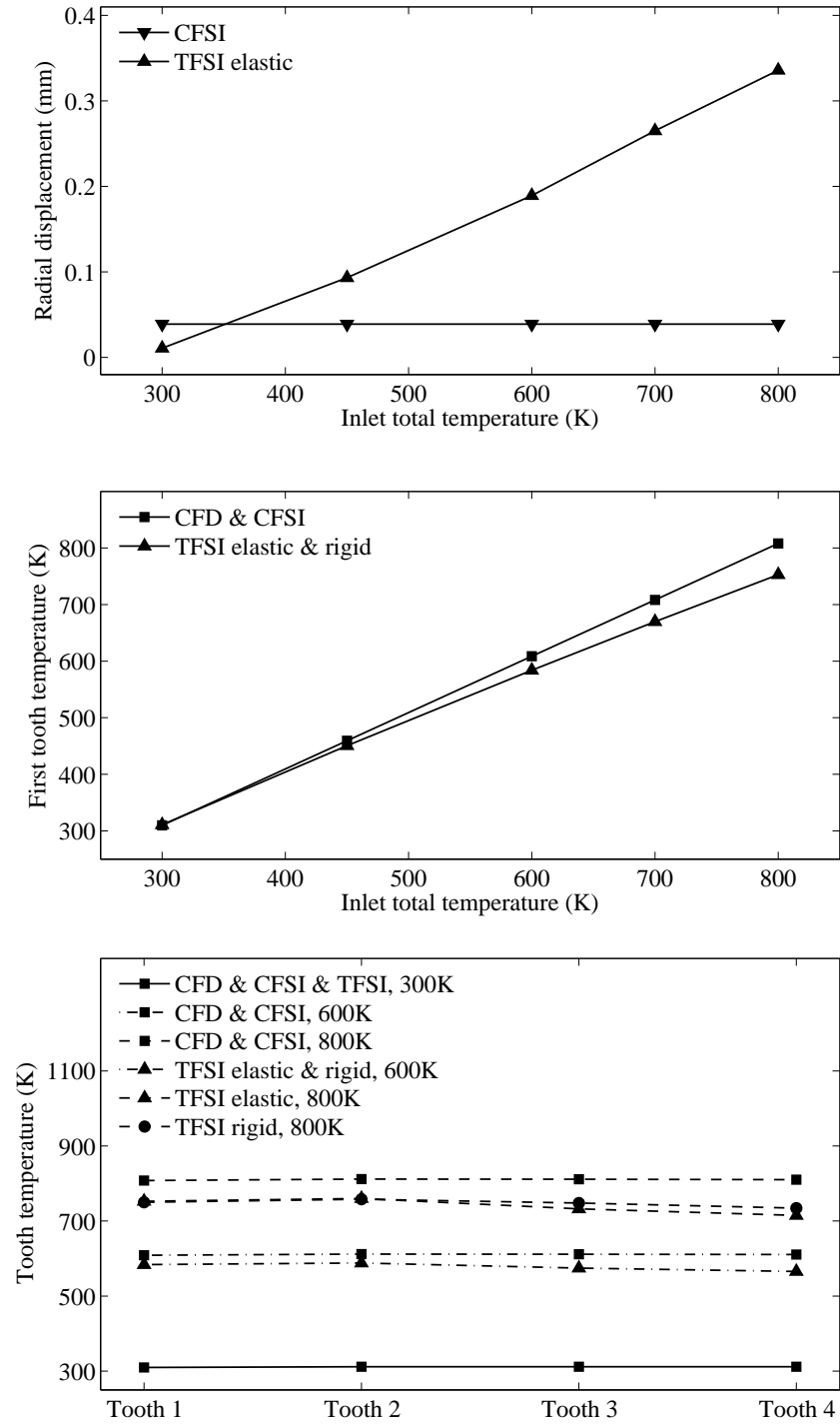
Figure 6.18: Influence of inlet total temperature on discharge coefficient, windage heating coefficient, outlet swirl ratio, rotor deformation, and tooth temperature ($\pi = 1.5$, $n = 6{,}000$ rpm)

the local total and static temperature of the fluid. In particular, the maximum temperature always occurs at the rotor teeth. Furthermore, the figures indicate that the thermal expansion of the stator is negligible compared to the rotor. The temperature and displacement distributions at low $T_{tot,in}$ and high $T_{tot,in}$ are qualitatively similar.

(a) $T_{tot,in} = 300$ K   (b) $T_{tot,in} = 600$ K
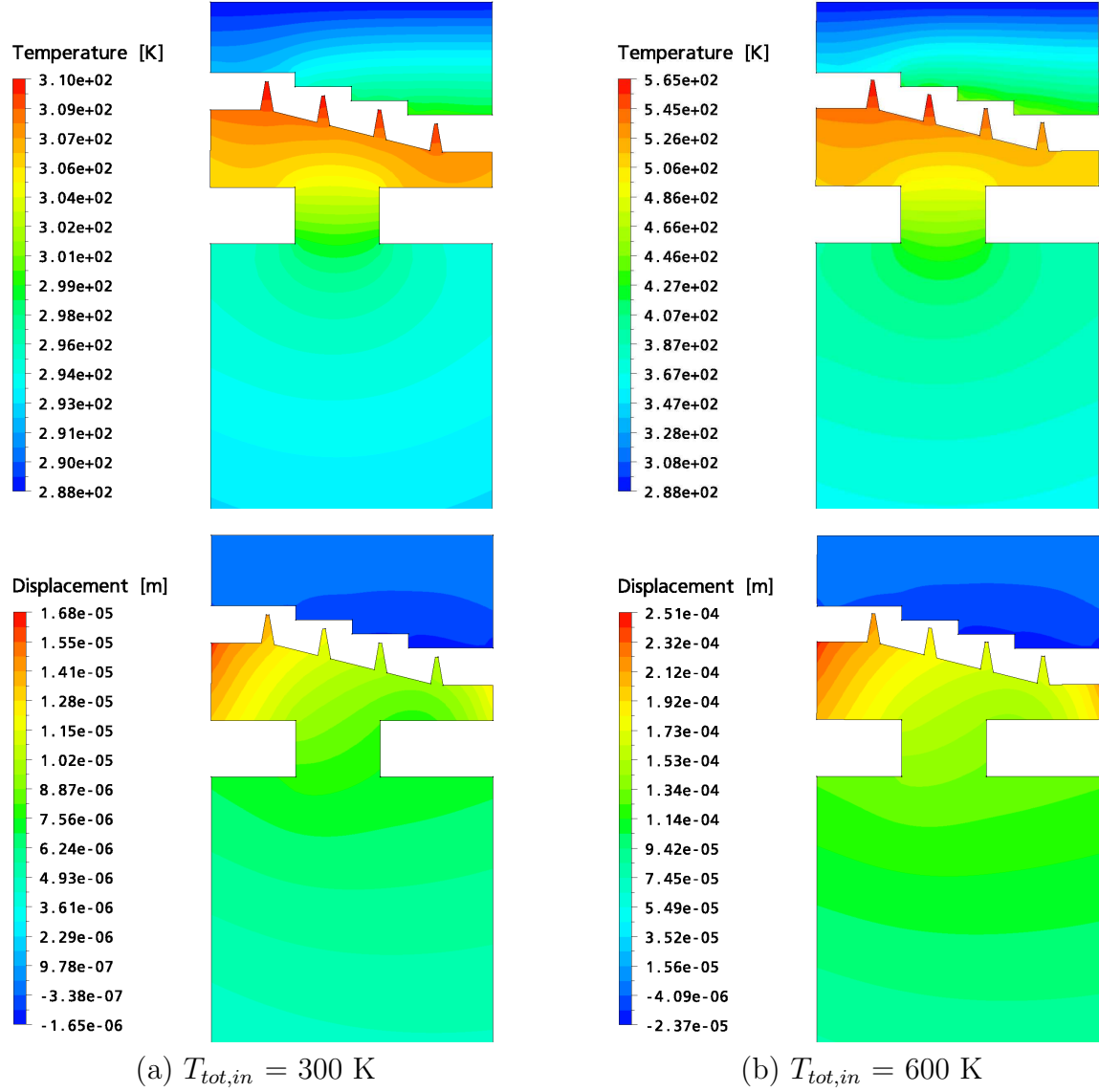
Figure 6.19: Temperature distribution and radial thermal expansion of the rotor and the stator ($\pi = 1.1$, $n = 6{,}000$ rpm)

In Fig. 6.20 and Fig. 6.21, the structural temperature and the mean Nusselt number at FSI surfaces are demonstrated for the rotor and the stator, respectively. The temperature distribution is obtained using TFSI with elastic structure, while the mean Nusselt number $\overline{\mathrm{Nu}}$ is computed and compared using both TFSI models. The thermal behaviors are studied in terms of the pressure ratio, rotational speed, and

inlet total temperature. When calculating $\overline{\mathrm{Nu}}$ using Eq. 2.5 and Eq. 2.6, the mean fluid temperature is taken as the averaged total temperature of the fluid domain, and the mean solid temperature as the averaged structural temperature of the fluid–rotor and fluid–stator surfaces.

Apparent temperature peaks are found at the tips of rotor teeth. The peak values decrease from the second tooth to the fourth tooth. Compared to the rotor, the temperature in the stator is lower by about 100 K, since there is no power input of the stator. Sudden increase in temperature can be recognized at each step, i.e. at locations of $x = 12$ mm, 20 mm, and 28 mm.

Generally, high pressure ratio leads to high Reynolds number and hence high Nusselt number, suggesting more heat is transferred from the hot air to the structures. It can be used to explain the increase of structural temperature and mean Nusselt number under growing π shown in Fig. 6.20 (a) and Fig. 6.21 (a).

Both the rotor temperature and the mean Nusselt number at the fluid–rotor interface are found to increase with rotational speed significantly, owing to the increasing power input of the rotor. In particular, the heat exchange between the fluid and the rotor becomes stronger, resulting in larger Nusselt number; and the total temperature of the fluid is raised, which leads to higher static temperature of the fluid and thus higher rotor temperature. In comparison, the stator temperature is less sensitive to rotational speed. The $\overline{\mathrm{Nu}}$ at the fluid–stator interface decreases slightly with rotational speed. It might be due to the temperature dependency of the fluid properties.

High inlet total temperature results in high structural temperatures as expected. However, the inlet total temperature plays only a minor role in the heat transfer across the fluid–structure boundaries. Growing $T_{tot,in}$ leads to a slight decrease in the fluid–rotor $\overline{\mathrm{Nu}}$ and has almost no influence on the fluid–stator $\overline{\mathrm{Nu}}$. The former could be explained by the temperature dependency of the fluid properties and the improvement in accuracy at increasing temperature gradient in the structure.

In addition, the trend that TFSI with rigid structure always leads to small $\overline{\mathrm{Nu}}$ can be explained by examining each term in Eq. 2.5. Although the mean heat fluxes at fluid–solid interfaces from both TFSI models are close to each other, the rigid model tends to predict higher mean fluid temperatures. As a result, the temperature difference obtained from the rigid model is larger than that from the elastic case, which leads to a smaller $\overline{\mathrm{Nu}}$.

To sum up, TFSI simulations are necessary to understand the fluid–solid heat transfer. Moreover, TFSI models with elastic and rigid structures lead to different mean Nusselt numbers. As the elastic version is closer to the real physics, it is recommended over its rigid counterpart.

(a) Influence of pressure ratio ($n = 6,000$ rpm, $T_{tot,in} = 600$ K)
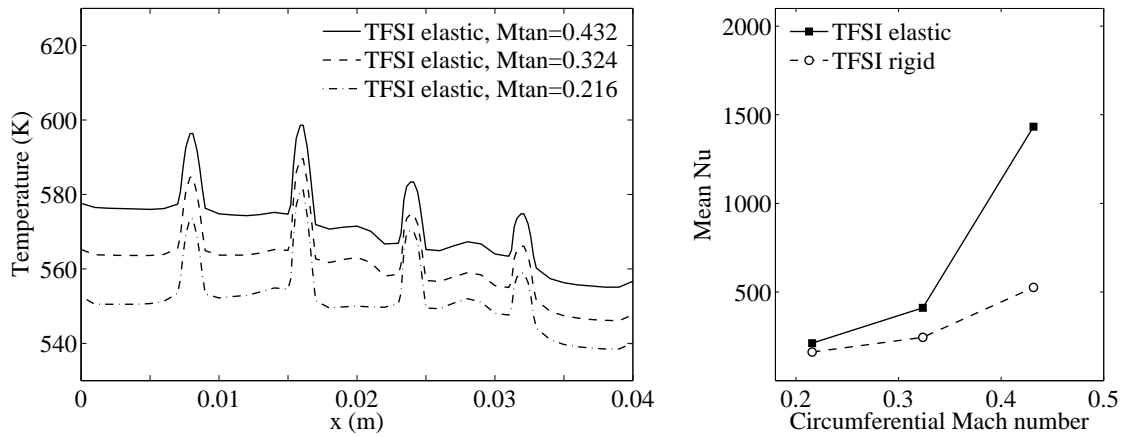
(b) Influence of rotational speed ($\pi = 1.5$, $T_{tot,in} = 600$ K)
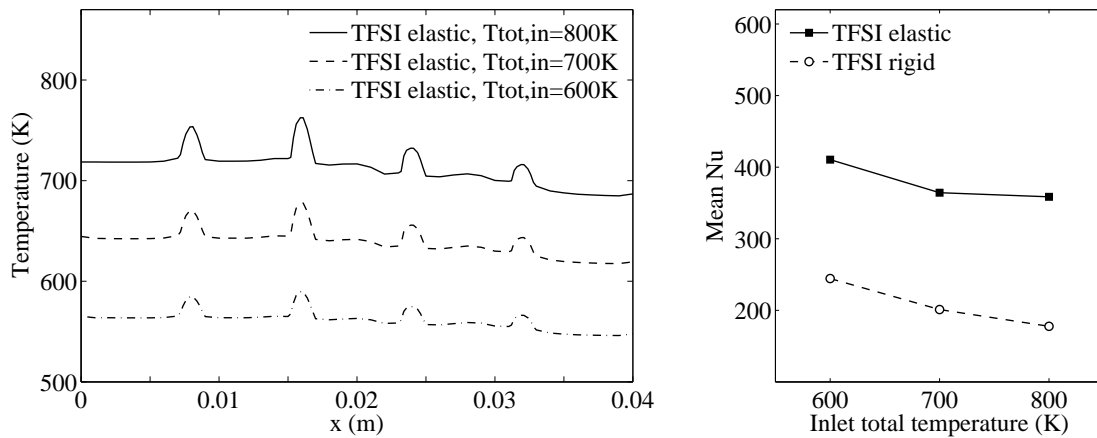
(c) Influence of inlet total temperature ($\pi = 1.5$, $n = 6,000$ rpm)

Figure 6.20: Structural temperature distribution across the labyrinth seal (left) and mean Nusselt number (right) of the rotor
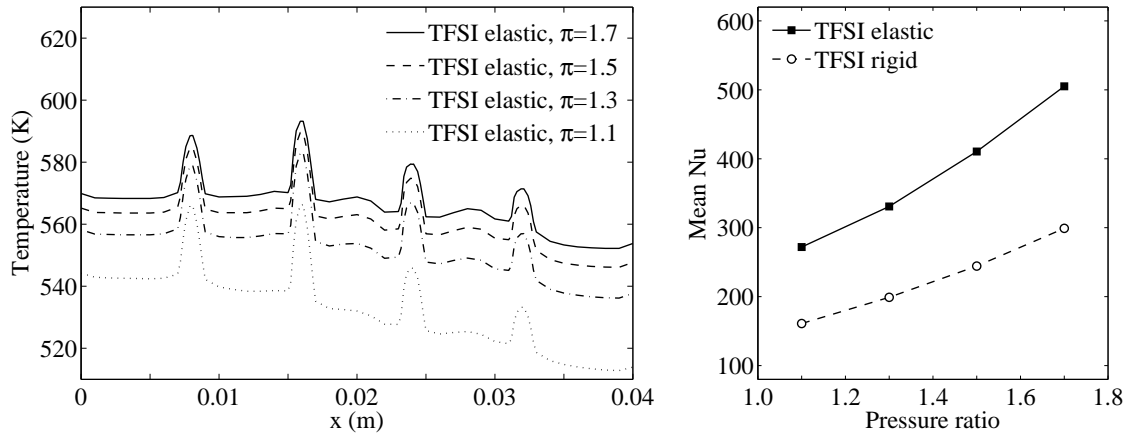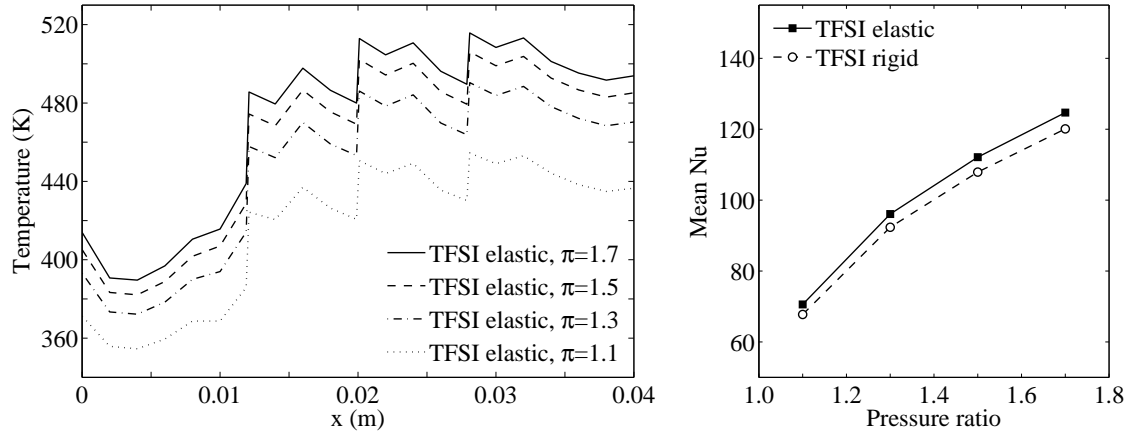
(a) Influence of pressure ratio ($n = 6,000$ rpm, $T_{tot,in} = 600$ K)
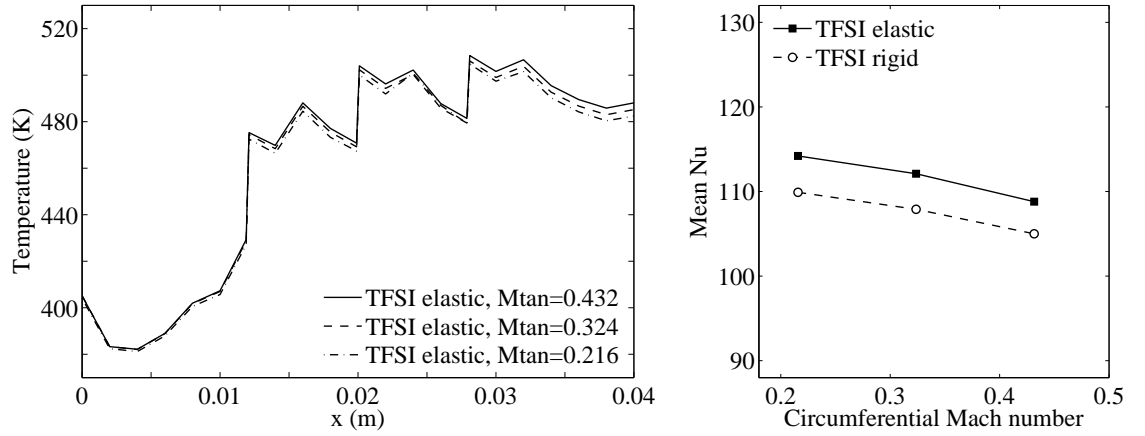
(b) Influence of rotational speed ($\pi = 1.5$, $T_{tot,in} = 600$ K)
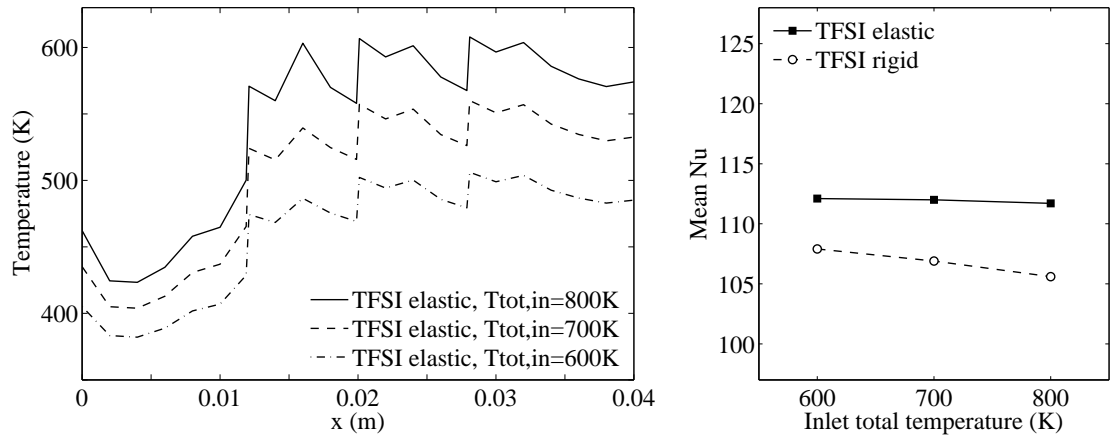
(c) Influence of inlet total temperature ($\pi = 1.5$, $n = 6,000$ rpm)

Figure 6.21: Structural temperature distribution across the labyrinth seal (left) and mean Nusselt number (right) of the stator

6.4   Summary

The thermal and centrifugal effects in a rotating stepped labyrinth seal are studied using FSI simulations. The inflow temperature varies from 300 K to 800 K, and the temperature–dependent material properties are used in the solid model. Mechanical and thermal variables are exchanged at fluid–rotor/stator surfaces. This study focuses on model comparisons, as well as the fluid–solid interfacial heat transfer phenomenon.

After defining the numerical models of the fluid and the structure, various FSI models are proposed to simulate the thermal and centrifugal FSI effects, which include: 1) one–way/two–way mechanical FSI for the centrifugal effects; 2) two–way thermal FSI with elastic/rigid structures for the thermal effects. Then, the CFD model and the CSM model are verified and validated against experimental results. The CFD model is examined with respect to the turbulence model and mesh dependency study. Velocity profiles and various dimensionless numbers are in excellent agreement with the test results. The centrifugal and thermal responses of the CSM model are well validated against test data and analytical solutions, too. Next, detailed flow features are illustrated. By comparing different FSI models, it is found that: 1) one–way and two–way centrifugal FSI models lead to almost identical results, but; 2) the thermal FSI models with elastic and rigid structures differ in results. All cases require comparable computational resources.

Based on the studies above, a systematic comparison of CFD and various FSI models is conducted. The study reveals the influences of pressure ratio, rotational speed, and inlet total temperature on the dimensionless numbers, structural displacement and temperature. It is also shown that CFD, centrifugal FSI, and thermal FSI lead to distinctively different results under some conditions and consistent results under other conditions. Moreover, thermal FSI modeled with elastic structure and rigid structure lead to different results in some cases.

Last, the heat transfer across fluid–solid interfaces is studied. The structural temperature field and thermal expansion are presented, and the temperature distribution as well as the interfacial mean Nusselt number are compared at various operating conditions. The results are discussed in detail to show how the structural thermal behaviors are affected by the pressure ratio, rotational speed, and inlet total temperature. The difference between thermal FSI models with elastic/rigid structures is also scrutinized.

In conclusion, the findings of this study help us to better understand the thermal and centrifugal FSI effects in labyrinth seals. In particular, it is clearly shown that there are gaps between FSI simulations and CFD predictions in some cases. The differences are studied in detail to provide guidelines on the significance of thermal and centrifugal FSI effects in labyrinth seals, and therefore, help to choose from various FSI models and traditional CFD models accordingly.

Chapter 7

Conclusions

The research work in this dissertation focuses on numerical investigations of various FSI effects in labyrinth seals. A fully coupled FSI approach is employed in all the simulations.

FSI effects have strong influences on the performance of labyrinth seals. However, in previous numerical studies, FSI problems are usually simplified by decoupling the fluid and solid fields. In contrast, the present study set out to model the mechanical and thermal FSI effects in labyrinth seals in a fully coupled manner. The advantages of FSI simulations over single field analyses are discussed in depth in the thesis and can be concluded as follows. First, FSI simulations can cope with the FSI effects that cannot be achieved by independent CFD/CSM simulations, such as the fluid force induced vibration. Second, the coupling behavior of labyrinth seals is obtained directly without empirical models or assumptions, avoiding possible errors introduced by the decoupling procedure. Finally, FSI analyses enhance the accuracy of fluid/solid field predictions, since the real physics is depicted more precisely.

The present study adopts an implicit partitioned approach for two–way FSI, which provides high accuracy, stability, and flexibility. As a preliminary study, the accuracy and efficiency of the FSI approach in parallel computations is examined against the numerical FSI benchmark. Then, three important FSI effects are studied in two test cases. In the first case, the fluid force induced vibration in non–rotating labyrinth seals is analyzed using 3D transient FSI simulations. The second case focuses on the FSI effects due to centrifugal growths and fluid–solid heat transfer in rotating high–temperature labyrinth seals.

The following conclusions can be drawn from the present study.

In the benchmark case, the verification work against the benchmark suggests that the current FSI approach has a relatively good accuracy in predicting fluid/solid fields as well as coupling effects. In addition, the FSI approach shows good parallel performance, such as a significant parallel speed–up, a four–times acceleration using the algebraic multigrid scheme, and an evenly distributed workload across the processors.

In the FSI case of fluid force induced vibration, periodic oscillations of the rotor are obtained. Linear relationships between the amplitude and pressure ratio/mass flow are well observed. Dependency study shows that inappropriate initial conditions can lead to over–predicted amplitudes. Thus, dependency tests are recommended to be carried out in advance. Under the given conditions, the amplitudes calculated using FSI are very small, which indicates that the rotor vibration caused by fluid forces is not critical. The methodology and results can contribute towards the FSI simulation of entire turbines.

In the FSI case of thermal and centrifugal effects, it is found that one–way and two–way centrifugal FSI models lead to almost identical results, while the thermal FSI models with elastic and rigid structures differ in results. The systematic comparison among CFD and various FSI models shows that the FSI effects can strongly influence seal performances, such as the discharge behavior, windage heating, swirl development, and heat transfer across fluid–solid interfaces. In particular, the difference between FSI and CFD simulations is discussed in detail to provide guidelines on the choice of models for future research. Moreover, the parameter study also reveals the impacts of the pressure ratio, rotational speed, and inlet total temperature on seal performances.

To sum up, the findings of this study help us to better understand the mechanical and thermal FSI effects in labyrinth seals, and thereby assist in improving the seal design.

Although the current study only involves two types of seal configurations, it is apparent that the same numerical approach is applicable to other complex configurations. For example, seals with honeycomb can be one of the further works using the proposed methods. Moreover, it is foreseeable to extend fully coupled FSI simulations to other critical components of jet engines in future research.

Appendix A

Performing Parallel FSI Analysis in ANSYS MFX

A.1 Standard CFD Analysis

This and the next sections are not intended as step–for–step instructions, for which the reader is urgently recommended to refer to the manuals, but rather a supplement based on the author's experiences.

- Launch the programs

    - Pre–processor: `cfx5pre`

    - Post–processor: `cfx5post`

    - Solver manager: `cfx5solve`

- Run the solver via `cfx5solve`

    - For a summary of full capacities:
      `cfx5solve -h`

    - Start from the definition file ⟨`filename`⟩`.def` using double precision:
      `cfx5solve -def` ⟨`filename`⟩`.def -double`

    - Start from ⟨`filename`⟩`.def` with the initial solution ⟨`filename`⟩`.res` interpolated onto the grid in ⟨`filename`⟩`.def`, where the result file can be replaced by full transient files `*_full.trn` or backup files `*_full.bak`:
      `cfx5solve -def` ⟨`filename`⟩`.def -ini` ⟨`filename`⟩`.res -interp-iv`

    - Restart from the result file ⟨`filename`⟩`.res`:
      `cfx5solve -def` ⟨`filename`⟩`.res`

    - Increase the memory allocation size when needed:
      `cfx5solve -def` ⟨`filename`⟩`.def -s` ⟨`factor`⟩

- Run in parallel

  - In local PVM mode on ⟨n⟩ processors:
    ```
    cfx5solve -def ⟨filename⟩.def -part ⟨n⟩ -par-local
    cfx5solve -def ⟨filename⟩.def -part ⟨n⟩ -start-method 'PVM
    Local Parallel'
    ```

  - In local MPICH mode on ⟨n⟩ processors:
    ```
    cfx5solve -def ⟨filename⟩.def -part ⟨n⟩ -start-method 'MPICH
    Local Parallel'
    ```

- Read and write the CCL file, which provides a flexible way of editing the definition and result files with text editors
  ```
  cfx5cmds -read -def ⟨filename⟩.def/res -text ⟨filename⟩.ccl
  cfx5cmds -write -def ⟨filename⟩.def/res -text ⟨filename⟩.ccl
  ```

- Write backup files during solution
  ```
  cfx5control ⟨directory⟩.dir -backup
  ```

- Post–processing from the command line using pre–defined ⟨filename⟩.cst/cse can be very convenient sometimes
  ```
  cfx5post -batch ⟨filename⟩.cst/cse -res ⟨filename⟩.res
  ```

A.2 Standard CSM Analysis

- Launch the program in GUI mode using the *ANSYS Academic Teaching Advanced* license
  ```
  ansys110 -g -p aa_t_a -j ⟨jobname⟩ -o ⟨output filename⟩
  ```

- Execute the APDL file ⟨filename⟩.inp in ANSYS
  ```
  /input,⟨filename⟩,inp
  ```

A.3 FSI Analysis

The complete FSI procedure is described below. The FSI input files are obtained by modifying the standard CFD/CSM input files.

1. Modify the CFD input file

   - Choose the *ANSYS Multifield via Prep7* solver coupling mode

   - Set the global mesh deformation options

   - Set the mesh motion for each boundary

2. Modify the CSM input file

   – Define FSI surfaces using command `SFA,,,FSIN,`⟨n⟩

3. Set FSI controls in the CSM input file

   – Use serial commands `MF-` to control the time duration, timestep, under–relaxation factors, convergence criteria, etc. of the FSI simulation

4. Start the solution using `cfx5solve`

   – `cfx5solve -def` ⟨filename⟩`.def -ansys-input` ⟨filename⟩`.inp`
     `-ansys-license aa_r`

5. Restart the solution

   – Note that ⟨`filename`⟩`.inp` here is different from the one above
     `cfx5solve -def` ⟨filename⟩`.res -ansys-input` ⟨filename⟩`.inp`
     `-ansys-restart` ⟨directory⟩`.ansys/`⟨filename⟩`.db`
     `-ansys-license aa_r`

6. Monitor the solution in the solver manager

   – Residuals of the governing equations

   – Convergence of the interface loads

   – Global and local monitor variables

7. Stop the solution

   – `cfx5stop -dir` ⟨directory⟩`.dir`

Comments

⋆ License issues: The academic research license `aa_r` is most powerful for its unlimited number of elements and parallel FSI capability. In contrast, the academic teaching licenses, such as `aa_t_a`, set an limit to the maximum number of elements and do not support parallel FSI. However, they should be sufficient for common structural analyses. Each FSI simulation takes one `aa_r` license. According to the current license policy, parallel CFD simulations running on no more than 4 processors do not require additional HPC (High Performance Computing) licenses.

⋆ Useful literature

   – ANSYS 11.0 Documentation: Coupled–Field Analysis Guide

– ANSYS CFX–Solver Modeling Guide: Coupling ANSYS CFX to an External Solver

– ANSYS CFX–Solver Modeling Guide: Using the Solver in Parallel

– ANSYS CFX–Solver Manager User's Guide: Starting ANSYS–CFX Solver from the Command Line

– Best Practice Guidelines from ERCOFTAC, ANSYS CFX (in the manuals), and www.cfd–online.com

⋆ There is another solver coupling mode called *ANSYS Multifield*, where the FSI controls are included in the CFD input file. The two modes are identical regarding the simulation results. However, the current mode is more convenient in the author's opinion.

⋆ In addition to step 4 in section A.3, it is also possible to start the solid and the fluid simulations separately using `ansys110` and `cfx5solve`. However, such method requires more operation steps and does not show any advantage over the current method; therefore it is omitted.

⋆ Note that the command lines and input files in the appendixes are based on ANSYS version 11.0, except in section B.3.

Appendix B

Input Files of FSI Benchmark

The following shows an example of the modifications required by the mechanical FSI analysis based on the existing CFD/CSM input files.

B.1   Excerpts from the CCL File

```
...
  BOUNDARY: fsi
    Boundary Type = WALL
    BOUNDARY CONDITIONS:
      MESH MOTION:
        Option = ANSYS MultiField
        Receive from ANSYS = Total Mesh Displacement
      END
      ...
  BOUNDARY: inlet
    Boundary Type = INLET
    BOUNDARY CONDITIONS:
      MESH MOTION:
        Option = Stationary
      END
      ...
  BOUNDARY: outlet
    Boundary Type = OUTLET
    BOUNDARY CONDITIONS:
      MESH MOTION:
        Option = Stationary
      END
      ...
```

```
BOUNDARY: sym
  Boundary Type = SYMMETRY
  BOUNDARY CONDITIONS:
    MESH MOTION:
      Option = Unspecified
    END
    ...
BOUNDARY: wall
  Boundary Type = WALL
  BOUNDARY CONDITIONS:
    MESH MOTION:
      Option = Stationary
    END
    ...
  MESH DEFORMATION:
    Option = Regions of Motion Specified
    MESH MOTION MODEL:
      Option = Displacement Diffusion
      MESH STIFFNESS:
        Option = Increase near Boundaries
        Stiffness Model Exponent = 1
      END
      ...
EXPERT PARAMETERS:
  include pref in forces = t
  ...
SIMULATION TYPE:
  Option = Transient
  EXTERNAL SOLVER COUPLING:
    ANSYS Input File = ⟨directory name⟩/⟨filename⟩.inp
    Option = ANSYS MultiField via Prep7
  END
  INITIAL TIME:
    Option = Coupling Initial Time
  END
  TIME DURATION:
    Option = Coupling Time Duration
  END
  TIME STEPS:
    Option = Coupling Timesteps
  END
```

```
  END
...
    EQUATION CLASS: meshdisp
      CONVERGENCE CONTROL:
        Maximum Number of Coefficient Loops = 20
        Minimum Number of Coefficient Loops = 1
        Timescale Control = Coefficient Loops
      END
      CONVERGENCE CRITERIA:
        Residual Target = 1e-4
        Residual Type = RMS
      END
    END
    ...
```

B.2   Excerpts from the APDL File

Start a new solution:

```
/UNITS,SI
/PREP7
    ...
FINISH
/SOL
    ANTYPE,4
    TRNOPT,FULL
    NLGEOM,ON
    *SET,fsidt,0.001
    DELTIM,fsidt,fsidt,fsidt
    AUTOTS,0
    KBC,0
    TINTP,,0.3,0.6
    TIMINT,ON
    ...
    ASEL,S,,,3
    ASEL,A,,,5
    ASEL,A,,,6
    SFA,ALL,,FSIN,1
    ALLSEL,ALL
```

```
   !************ Multifield Settings ******************
   MFAN,ON
   MFPS,GROUP1,ANSYS
   MFPS,GROUP2,CFX
   MFSO,GROUP1,GROUP2
   !*
   MFLC,SURF,ANSYS,1,DISP,CFX,fsi,Total Mesh Displacement,NONC
   MFLC,SURF,CFX,fsi,Total Force,ANSYS,1,FORC,CPP
   !*
   MFTI,5
   MFDT,fsidt,fsidt,fsidt,0
   AUTOTS,OFF
   MFRS,0,SING
   !*
   MFIT,100,1,1
   MFCO,ALL,0.001
   MFCO,UZ,1.0
   MFCO,FZ,1.0
   MFRE,DISP,0.1,RELX
   MFRE,FORC,0.75,RELX
   !*
   /GST,ON,ON
   TIME,5.0
   SOLVE
   SAVE
FINISH
```

Restart with a different timestep size and different FSI under–relaxation:

```
RESUME,⟨restart filename⟩,db
/SOLU
   *SET,fsidt,0.004
   DELTIM,fsidt,fsidt,fsidt
   TIME,2.0+fsidt*10e3
   !*
   MFRS,-1,SING
   MFTI,2.0+fsidt*10e3
   MFDT,fsidt,fsidt,fsidt,off
   MFRE,DISP,0.2,RELX
   MFRE,FORC,1.0,RELX
   !*
```

```
    /GST,ON,ON
    SOLVE
    SAVE
FINISH
```

B.3 LoadLeveler File

The following LoadLeveler file contains the parallel settings on HHLR and the solution commands of ANSYS version 12.0.

```
#!/usr/bin/bash
#-----------------------------------------
# Beginning of step0
# @ step_name = step0
# @ output = out
# @ error = err
# @ notification = always
# @ notify_user = ⟨email adress⟩
# @ checkpoint = no
# @ restart = no
# @ job_type = parallel
# @ class = fnb_class
# @ requirements = (Machine == "hlr1d")
# @ node = 1
# @ total_tasks = 16
# @ resources = ConsumableCpus(1) ConsumableMemory(1GB)
# @ wall_clock_limit = 23:59:59
# @ initialdir = ⟨directory⟩
# @ queue
echo "Starting FSI:"

/ansys_inc/v120/CFX/bin/cfx5solve -def ⟨filename⟩.res -double \
-ansys-input ⟨filename⟩.inp \
-ansys-restart ⟨directory⟩.ansys/⟨filename⟩.db \
-ansys-license aa_r -ansys-installation /ansys_inc/v120/ansys \
-part 16 -start-method 'MPICH Local Parallel'

echo "Finished"
/sw/bin/collect_accounting
#-----------------------------------------------
```

Appendix C

Input Files of FSI Case II

This chapter demonstrates how to modify the CFD/CSM input files for a thermal FSI analysis.

C.1   Excerpts from the CCL File

```
...
  BOUNDARY: inlet
    Boundary Type = INLET
    BOUNDARY CONDITIONS:
      MESH MOTION:
        Option = Unspecified
      END
      ...
  BOUNDARY: outlet
    Boundary Type = OUTLET
    BOUNDARY CONDITIONS:
      MESH MOTION:
        Option = Unspecified
      END
      ...
  BOUNDARY: rotor
    Boundary Type = WALL
    BOUNDARY CONDITIONS:
      HEAT TRANSFER:
        Option = ANSYS MultiField
        Receive from ANSYS = Temperature
      END
      MESH MOTION:
```

```
              Option = ANSYS MultiField
              Receive from ANSYS = Total Mesh Displacement
            END
            ...
    BOUNDARY: stator
      Boundary Type = WALL
      BOUNDARY CONDITIONS:
        HEAT TRANSFER:
            Option = ANSYS MultiField
            Receive from ANSYS = Temperature
        END
        MESH MOTION:
            Option = ANSYS MultiField
            Receive from ANSYS = Total Mesh Displacement
        END
        ...
      MESH DEFORMATION:
        Option = Regions of Motion Specified
        MESH MOTION MODEL:
            Option = Displacement Diffusion
            MESH STIFFNESS:
              Option = Increase near Small Volumes
              Stiffness Model Exponent = 0.5
            END
            ...
EXPERT PARAMETERS:
    include pref in forces = t
    ...
SIMULATION TYPE:
    Option = Steady State
    EXTERNAL SOLVER COUPLING:
      ANSYS Input File = ⟨directory name⟩/⟨filename⟩.inp
      Option = ANSYS MultiField via Prep7
    END
END
...
    EQUATION CLASS: meshdisp
      CONVERGENCE CONTROL:
        Maximum Number of Coefficient Loops = 10
        Minimum Number of Coefficient Loops = 1
        Timescale Control = Coefficient Loops
```

```
      END
      CONVERGENCE CRITERIA:
         Residual Target = 1e-4
         Residual Type = RMS
      END
   END
   ...
```

C.2 Excerpts from the APDL File

Start a new solution:

```
/UNITS,SI
/PREP7
   ...
   !*** FSI interfaces:  rotor
   ASEL,S,,,31,46,5
   ASEL,A,,,32,47,5
   ...
   SFA,ALL,,FSIN,1
   ALLSEL,ALL
   !*** FSI interfaces:  stator
   ASEL,S,,,148
   ASEL,A,,,153,156,3
   ...
   SFA,ALL,,FSIN,2
   ALLSEL,ALL
FINISH
/SOL
   ANTYPE,4
   TRNOPT,FULL
   NLGEOM,ON
   *SET,fsidt,1e-5
   DELTIM,fsidt,fsidt,fsidt
   AUTOTS,0
   KBC,1
   TIMINT,OFF
   ...
   !************ Multifield Settings ******************
```

```
MFAN,ON
MFPS,GROUP1,ANSYS
MFPS,GROUP2,CFX
MFSO,GROUP1,GROUP2
!*
MFLC, SURF,ANSYS,1,DISP,CFX,rotor,Total Mesh Displacement,NONC
MFLC, SURF,CFX,rotor,Total Force,ANSYS,1,FORC,CPP
MFLC, SURF,ANSYS,1,TEMP,CFX,rotor,Temperature,NONC
MFLC, SURF,CFX,rotor,Wall Heat Flow,ANSYS,1,HFLU,CPP
!*
MFLC, SURF,ANSYS,2,DISP,CFX,stator,Total Mesh Displacement,NONC
MFLC, SURF,CFX,stator,Total Force,ANSYS,2,FORC,CPP
MFLC, SURF,ANSYS,2,TEMP,CFX,stator,Temperature,NONC
MFLC, SURF,CFX,stator,Wall Heat Flow,ANSYS,2,HFLU,CPP
!*
MFTI,1.0
MFDT,fsidt,fsidt,fsidt,0
AUTOTS,OFF
MFRS,0,SING
!*
MFIT,100,1,1
MFCO,ALL,0.001
MFRE,DISP,0.1,RELX
MFRE,FORC,1.0,RELX
MFRE,TEMP,0.1,RELX
MFRE,HFLU,0.1,RELX
!*
/GST,ON,ON
TIME,1.0
SOLVE
SAVE
FINISH
```

Bibliography

[1] J. Denecke. *Rotierende Labyrinthdichtungen mit Honigwabenanstreifbelägen – Untersuchung der Wechselwirkung von Durchflussverhalten, Drallverlauf und Totaltemperaturänderung (PhD Thesis)*. LOGOS–Verlag, 2007.

[2] D. Childs. *Turbomachinery rotordynamics: phenomena, modeling, and analysis*. John Wiley & Sons, 1993.

[3] **Y. Du** and M. Schäfer. Fluid Structure Interaction in labyrinth seals. In *ANSYS conference and 26. CADFEM users' meeting, CD ROM*, Darmstadt, Germany, 2008.

[4] J. Denecke, K. Dullenkopf, S. Wittig, and H. J. Bauer. Experimental investigation of the total temperature increase and swirl development in rotating labyrinth seals. ASME Paper No. GT2005-68677, 2005.

[5] H. K. Müller and B. S. Nau. *Drosseldichtungen für Gase*. www.fachwissen–dichtungstechnik.de, Waiblingen, Germany, 2008.

[6] I. R. Delgado and M. P. Proctor. Continued investigation of leakage and power loss test results for competing turbine engine seals. NASA/TM-2006-214420, 2006.

[7] W. Waschka, S. Wittig, and S. Kim. Influence of high rotational speeds on the heat transfer and discharge coefficients in labyrinth seals. *ASME Journal of Turbomachinery*, 114:462–468, 1992.

[8] J. A. Millward and M. F. Edwards. Windage heating of air passing through labyrinth seals. *ASME Journal of Turbomachinery*, 118:414–419, 1996.

[9] S. Wittig, K. Jacobsen, U. Schelling, and S. Kim. Heat transfer in stepped labyrinth seals. *ASME Journal of Engineering for Gas Turbines and Power*, 110:63–69, 1988.

[10] W. Waschka, S. Wittig, S. Kim, and T. Scherer. Heat transfer and leakage in high–speed rotating stepped labyrinth seals. In *AGARD, Heat Transfer and Cooling in Gas Turbines*, 1993.

[11] M. P. Proctor and I. R. Delgado. Leakage and power loss test results for competing turbine engine seals. NASA/TM-2004-213049, ASME Paper No. GT2004-53935, 2004.

[12] A. J. M. Gamal and J. M. Vance. Labyrinth seal leakage test: tooth profile, tooth thickness, and eccentricity effects. *ASME Journal of Engineering for Gas Turbines and Power*, 130:012510, 2008.

[13] W. Waschka, S. Wittig, T. Scherer, and S. Kim. Leakage loss and heat transfer in high-speed rotating labyrinth seals : an experimental verification of numerical codes. In *The International Gas Turbine Congress : book of abstracts*, number 2, pages 239–247, 1991.

[14] W. Waschka, T. Scherer, S. Kim, and S. Wittig. Study of heat transfer and leakage in high rotating stepped labyrinth seals. In *ISROMAC*, number 4, pages 326–334, 1992.

[15] K. Willenborg, S. Kim, and S. Wittig. Effects of Reynolds number and pressure ratio on leakage loss and heat transfer in a stepped labyrinth seal. *ASME Journal of Turbomachinery*, 123:815–822, 2001.

[16] K. Willenborg, V. Schramm, S. Kim, and S. Wittig. Influence of a honeycomb facing on the heat transfer in a stepped labyrinth seal. *ASME Journal of Engineering for Gas Turbines and Power*, 124:133–139, 2002.

[17] K. Kwanka. Dynamic coefficients of stepped labyrinth gas seals. *ASME Journal of Engineering for Gas Turbines and Power*, 122:473–477, 2000.

[18] K. Kwanka. Improving the stability of labyrinth gas seals. *ASME Journal of Engineering for Gas Turbines and Power*, 123:383–387, 2001.

[19] X. Shen, J. Jing, and Q. Gong. Experimental and numerical analysis of dynamics of the rotor–bearing–seal system. ASME Paper No. DETC2007-34374, 2007.

[20] D. L. Rhode, J. W. Johnson, and D. H. Broussard. Flow visualization and leakage measurements of stepped labyrinth seals: part 1–annular groove. *ASME Journal of Turbomachinery*, 119:839–843, 1997.

[21] D. L. Rhode, J. S. Younger, and M. D. Wernig. Flow visualization and leakage measurements of stepped labyrinth seals: part 2–sloping surfaces. *ASME Journal of Turbomachinery*, 119:844–848, 1997.

[22] M. Michaud, A. Vakili, and A. Meganathan. An experimental study of labyrinth seal flow. ASME Paper No. IJPGC2003-40097, 2003.

[23] J. Denecke, V. Schramm, S. Kim, and S. Wittig. Influence of rub–grooves on labyrinth seal leakage. *ASME Journal of Turbomachinery*, 125:387–393, 2003.

[24] D. Rhode and R. Hibbs. Clearance effects on corresponding annular and labyrinth seal flow leakage characteristics. *ASME Journal of Tribology*, 115: 699–704, 1993.

[25] V. Schramm, J. Denecke, S. Kim, and S. Wittig. Shape optimization of a labyrinth seal applying the simulated annealing method. *International Journal of Rotating Machinery*, 10(5):365–371, 2004.

[26] Y. Wang, C. Young, G. Snowsill, and T. Scanlon. Study of airflow features through step seals in the presence of dis–engagement due to axial movement. ASME Paper No. GT2004-53056, 2004.

[27] A. Vakili, A. Meganathan, M. Michaud, and S. Radhakrishnan. An experimental and numerical study of labyrinth seal flow. ASME Paper No. GT2005-68224, 2005.

[28] J. Li, X. Yan, and Z. Feng. Effects of pressure ratio and fin pitch on leakage flow characteristics in high rotating labyrinth seals. ASME Paper No. GT2006-91145, 2006.

[29] J. J. Moore. Three–dimensional CFD rotordynamic analysis of gas labyrinth seals. *ASME Journal of Vibration and Acoustics*, 125:427–433, 2003.

[30] T. Hirano, Z. Guo, and R. G. Kirk. Application of Computational Fluid Dynamics analysis for rotating machinery–part II: labyrinth seal analysis. *ASME Journal of Engineering for Gas Turbines and Power*, 127:820–826, 2005.

[31] J. Schettel, M. Deckner, K. Kwanka, B. Lüneburg, and R. Nordmann. Rotordynamic coefficients of labseals for turbines – comparing CFD results with experimental data on a comb–grooved labyrinth. ASME Paper No. T2005-68732, June 2005.

[32] V. Schramm, K. Willenborg, S. Kim, and S. Wittig. Influence of a honeycomb facing on the flow through a stepped labyrinth seal. *ASME Journal of Engineering for Gas Turbines and Power*, 124:140–146, 2002.

[33] D.-C. Choi and D. L. Rhode. Development of a two–dimensional Computational Fluid Dynamics approach for computing three–dimensional honeycomb labyrinth leakage. *ASME Journal of Engineering for Gas Turbines and Power*, 126:794–802, 2004.

[34] B. Soemarwoto, J. Kok, K. Cock, A. Kloosterman, and G. Kool. Performance evaluation of gas turbine labyrinth seals using Computational Fluid Dynamics. ASME Paper No. GT2007-27905, 2007.

[35] X. Yan, J. Li, L. Song, and Z. Feng. Investigations on the discharge and total temperature increase characteristics of the labyrinth seals with honeycomb and smooth lands. *ASME Journal of Turbomachinery*, 131:041009, 2009.

[36] H. Lange. *Methoden zur numerischen Simulation des strömungs– und strukturmechanischen Verhaltens von Labyrinthdichtungen (PhD Thesis).* VDI–Verlag, 2005.

[37] V. Kudriavtsev, M. Braun, and R. Hendricks. Fluid Structure Interaction analysis of the adaptive finger seal assembly using CFD–ACE+/FEMSTRESS. ASME Paper No. PVP2003-1964, 2003.

[38] K. Fujita and M. Kato. Instability of an axial leakage flow–induced vibration of thin cylindrical shells having freely supported end. ASME Paper No. IMECE2004-59491, 2004.

[39] U. Yucel and J. Y. Kazakia. Analytical prediction techniques for axisymmetric flow in gas labyrinth seals. *ASME Journal of Engineering for Gas Turbines and Power*, 123:255–257, 2001.

[40] D. Eser. Rotordynamic coefficients in stepped labyrinth seals. *Computer Methods in Applied Mechanics and Engineering*, 191:3127–3135, 2002.

[41] J. Denecke, J. Färber, K. Dullenkopf, and H. J. Bauer. Dimensional analysis and scaling of rotating seals. ASME Paper No. GT2005-68676, 2005.

[42] J. Denecke, J. Färber, K. Dullenkopf, and H. J. Bauer. Interdependence of discharge behavior, swirl development and total temperature increase in rotating labyrinth seals. ASME Paper No. GT2008-51429, 2008.

[43] H. J. Bungartz and M. Schäfer. *Fluid–Structure Interaction – modelling, simulation, optimization.* Springer, Berlin, Heidelberg, 2006.

[44] D. C. Sternel, M. Schäfer, M. Heck, and S. Yigit. Efficiency and accuracy of Fluid–Structure Interaction simulations using an implicit partitioned approach. *Computational mechanics*, 43:103–113, 2008.

[45] M. Schäfer. Coupled fluid–solid problems: survey on numerical approaches and applications. ASME Paper No. PVP2003-1942, 2003.

[46] M. Schäfer, M. Heck, and S. Yigit. An implicit partitioned method for numerical simulation of Fluid–Structure Interaction. In H. J. Bungartz and M. Schäfer, editors, *Fluid–Structure Interaction – modelling, simulation, optimization*, Berlin, 2006. Springer Verlag.

[47] *FASTEST–user manual*. Institute of numerical methods in mechanical engineering, Technische Universität Darmstadt, Germany, 2005.

[48] R. Taylor. *FEAP – a finite element analysis program. Version 7.5 Theory manual*. University of California at Berkeley, 2003.

[49] *MpCCI 3.0.6–21 documentation*. Fraunhofer SCAI, Sankt Augustin, Germany.

[50] M. Heck. *Mehrgitterverfahren zur effizienten numerischen Simulation von Fluid–Struktur–Wechselwirkungen (PhD Thesis)*. Shaker–Verlag, 2008.

[51] S. Turek and J. Hron. Proposal for numerical benchmarking of Fluid–Structure Interaction between an elastic object and laminar incompressible flow. In H. J. Bungartz and M. Schäfer, editors, *Fluid–Structure Interaction – modelling, simulation, optimization*, pages 371–385, Berlin, 2006. Springer Verlag.

[52] M. Schäfer, S. Yigit, and M. Heck. Implicit partitioned Fluid–Structure Interaction coupling. ASME Paper No. PVP2006-ICPVT-11-93184, 2006.

[53] S. Yigit. *Phänomene der Fluid–Struktur–Wechselwirkung und deren numerische Berechnung (PhD Thesis)*. Shaker–Verlag, 2008.

[54] P. Pironkov. *Numerical simulation of thermal Fluid–Structure Interaction (PhD Thesis)*. Published online, 2010.

[55] M. Schäfer and I. Teschauer. Numerical simulation of coupled fluid–solid problems. *Computer Methods in Applied Mechanics and Engineering*, 190:3645–3667, 2001.

[56] J. Dale and A. Holdø. Fluid Structure Interaction modelling. ASME Paper No. PVP2004-2858, 2004.

[57] J. Hron and S. Turek. A monolithic FEM/multigrid solver for ALE formulation of Fluid Structure Interaction with application in biomechanics. In H. J. Bungartz and M. Schäfer, editors, *Fluid–Structure Interaction – modelling, simulation, optimization*, pages 146–170. Springer, Berlin, 2006.

[58] B. Gatzhammer. Exploiting the partitioned coupling approach with preCICE. In *International workshop on computational engineering – special topic Fluid–Structure–Interaction*, Herrsching, Germany, 2009.

[59] J. Vierendeels. Stability issues in Fluid–Structure Interaction calculation with partitioned solvers. In *International workshop on computational engineering – special topic Fluid–Structure–Interaction*, Herrsching, Germany, 2009.

[60] C. Förster, W. A. Wall, and E. Ramm. Artificial added mass instabilities in sequential staggered coupling of nonlinear structures and incompressible viscous flows. *Computer Methods in Applied Mechanics and Engineering*, 196:1278–1293, 2007.

[61] U. Küttler and W. A. Wall. Fixed–point Fluid–Structure Interaction solvers with dynamic relaxation. *Computational Mechanics*, 43:61–72, 2008.

[62] U. Küttler and W. A. Wall. Vector extrapolation for strong coupling Fluid–Structure Interaction solvers. *ASME Journal of Applied Mechanics*, 76:021205, 2009.

[63] A. H. Van Zuijlen and H. Bijl. Subiteration acceleration in partitioned FSI problems using multi–grid. In *International workshop on computational engineering – special topic Fluid–Structure–Interaction*, Herrsching, Germany, 2009.

[64] M. Münsch and M. Breuer. Numerical simulation of Fluid–Structure Interaction using eddy–resolving schemes. In *International workshop on computational engineering – special topic Fluid–Structure–Interaction*, Herrsching, Germany, 2009.

[65] C. D. Wang and C. M. Wang. Computation of the stress resultants of a floating mindlin plate in response to linear wave forces. *Journal of Fluids and Structures*, 24:1042–1057, 2008.

[66] J. Sigrist, D. Broc, and C. Lainé. Fluid–Structure Interaction effects modeling for the modal analysis of a nuclear pressure vessel. *ASME Journal of Pressure Vessel Technology*, 129:1–6, 2007.

[67] J. Sigrist and D. Broc. Fluid–Structure Interaction effects modeling for the modal analysis of a steam generator tube bundle. *ASME Journal of Pressure Vessel Technology*, 131:031302, 2009.

[68] F. K. Benra and H. J. Dohmen. Comparison of pump impeller orbit curves obtained by measurement and FSI simulation. ASME Paper No. PVP2007-26149, 2007.

[69] P. Diwakar and L. Lin. Study of dynamic stresses in pipe networks and pressure vessels using Fluid–Solid–Interaction models. ASME Paper No. PVP2007-26009, 2007.

[70] R. Gorla, S. Pai, and J. Rusick. Probabilistic study of Fluid Structure Interaction. ASME Paper No. GT-2002-30308, 2002.

[71] R. Gorla, S. Pai, I. Blankson, S. Tadepalli, and S. Gorla. Unsteady Fluid Structure Interaction in a turbine blade. ASME Paper No. GT2005-68157, 2005.

[72] H. Ito, Y. Suh et al. A direct assessment approach for structural strength evaluation of cargo containment system under sloshing inside LNGC tanks based on Fluid Structure Interaction. ASME Paper No. OMAE2008-57572, 2008.

[73] M. Kuntz and F. R. Menter. Simulation of Fluid–Structure Interactions in aeronautical applications. In *European Congress on Computational Methods in Applied Sciences and Engineering (ECCOMAS)*, 2004.

[74] I. Pericevic, M. Moatamedi, and M. Souli. Numerical modelling of Fluid Structure Interaction in blood vessels. ASME Paper No. PVP2005-71456, 2005.

[75] M. Souli, Y. Sofiane, and L. Olovsson. ALE and Fluid/Structure Interaction in LS–DYNA. ASME Paper No. PVP2004-2870, 2004.

[76] A. Timperi, T. Pättikangas et al. Validation of Fluid Structure Interaction calculations in a Large–Break Loss Of Coolant Accident. ASME Paper No. ICONE16-48206, 2008.

[77] S. Zhang. A flexible, yet robust coupled method for Fluid Structure Interaction. ASME Paper No. FEDSM2007-37123, 2007.

[78] T. Tezduyar and S. Sathe. Modelling of Fluid–Structure Interactions with the space–time finite elements: solution techniques. *International Journal for Numerical Methods in Fluids*, 54:855–900, 2007.

[79] R. Gasch, R. Nordmann, and H. Pfützner. *Rotordynamik*. Springer, Berlin, Heidelberg, second edition, 2006.

[80] *ANSYS CFX–Solver theory guide, ANSYS CFX Release 11.0*. ANSYS Europe Ltd., .

[81] J. H. Ferziger and M. Perić. *Computational methods for fluid dynamics*. Springer, Berlin, Heidelberg, third edition, 2002.

[82] H. K. Versteeg and W. Malalasekera. *An introduction to Computational Fluid Dynamics – the finite volume method*. Pearson Education Limited, England, second edition, 2007.

[83] M. Schäfer. *Computational engineering – introduction to numerical methods.* Springer, Berlin, Heidelberg, 2006.

[84] K. Huang, M. Xue, and M. Lu. *Tensor analysis.* Tsinghua University Press, Beijing, 2003.

[85] F. R. Menter. Two–equation eddy–viscosity turbulence models for engineering applications. *AIAA Journal*, 32(8):1598–1605, 1994.

[86] L. Davidson. *Lecture notes: numerical methods for turbulent flow.* Chalmers University of Technology, Göteborg, Sweden, 2005.

[87] I. Demirdžić and M. Perić. Space conservation law in finite volume calculations of fluid flow. *International Journal for Numerical Methods in Fluids*, 8:1037–1050, 1988.

[88] B. R. Hutchinson and G. D. Raithby. A multigrid method based on the additive correction strategy. *Numerical heat transfer, part B: fundamentals*, 9:511–537, 1986.

[89] *ANSYS CFX–Solver modeling guide, ANSYS CFX Release 11.0.* ANSYS Europe Ltd., .

[90] M. Casey and T. Wintergerste. *Best practice guidelines.* ERCOFTAC, first edition, 2000.

[91] *ANSYS® Academic Research, Release 12.0, Help system.* ANSYS Inc.

[92] T. Belytschko, W. K. Liu, and B. Moran. *Nonlinear finite elements for continua and structures.* John Wiley & Sons, first edition, 2000.

[93] M. Lu and X. Luo. *Foundations of elasticity theory.* Tsinghua University Press, Beijing, 2001.

[94] X. Wang. *Finite element method.* Tsinghua University Press, Beijing, 2003.

[95] O. C. Zienkiewicz, R. L. Taylor, and J. Z. Zhu. *The finite element method – its basis and fundamentals.* Elsevier Butterworth–Heinemann, Oxford, sixth edition, 2005.

[96] F. Menter, P. Sharkey, S. Yakubov, and M. Kuntz. Overview of fluid–structure coupling in ANSYS–CFX. ASME Paper No. OMAE2006-92145, 2006.

[97] ANSYS, Inc. Multiphysics for the real world. *ANSYS advantage*, 3:11–13, 2009.

[98] K. Dietrich. *Implementation of partitioned solution approaches for the numerical simulation of Fluid–Structure Interactions (Bachelor Thesis)*. Institute of numerical methods in mechanical engineering, Technische Universität Darmstadt, 2009.

[99] G. Becker, **Y. Du**, P. Pironkov, and M. Schäfer. Quantitative comparison of FSI simulation approaches with respect to efficiency and accuracy. In B. Schrefler, E. Oñate, and M. Papadrakakis, editors, *Computational methods for coupled problems in science and engineering III, CD ROM*, Ischia, Italy, 2009.

[100] **Y. Du** and M. Schäfer. Fluid Structure Interaction in non–contacting gas seals. In B. Schrefler, E. Oñate, and M. Papadrakakis, editors, *Computational methods for coupled problems in science and engineering III, CD ROM*, Ischia, Italy, 2009.

[101] **Y. Du** and M. Schäfer. Fluid Structure Interaction in non–contacting gas seals. In *International workshop on computational engineering – special topic Fluid–Structure–Interaction*, Herrsching, Germany, 2009.

[102] *Users' manual for the labyrinth seal design model (KTK), NASA/CR–2003–212367*. Mechanical Technology, Inc., 2005.

[103] **Y. Du** and M. Schäfer. Mechanical and thermal Fluid Structure Interaction of non–contacting gas seals in jet engines. In J. C. F. Pereira and A. Sequeira, editors, *European conference on Computational Fluid Dynamics (ECCOMAS CFD), CD ROM*, Lisbon, Portugal, 2010.

[104] J. Denecke, K. Dullenkopf, and H. J. Bauer. Vergleichende Bestimmung des Drallverlaufs in schnell rotierenden Labyrinthdichtungen mittels LDA und CFD. In *12. GALA – Fachtagung – Lasermethoden in der Strömungsmetechnik*, 2004.

[105] F. R. Menter. A comparison of some recent eddy–viscosity turbulence models. *ASME Journal of Fluids Engineering*, 118:514–519, 1996.

Lebenslauf

Persönliche Angaben

Name	Yu Du
Geburtsdatum	6. März 1984
Geburtsort	Tianjin, V. R. China
Nationalität	chinesisch
Familienstand	ledig

Werdegang

1990 – 1995 **Grundschule**
Anshandao-Schule und Shiyan-Schule in Tianjin

1995 – 2001 **Gymnasium**
Yizhong-Gymnasium und Xinhua-Gymnasium in Tianjin

2001 – 2005 **Bachelor-Studium der Engineering Mechanics**
Tsinghua University

2005 – 2007 **Master-Studium der Computational Solid Mechanics**
Institute of Solid Mechanics,
Department of Engineering Mechanics,
Tsinghua University

seit 2007 **Wissenschaftliche Mitarbeiterin**
Fachgebiet Numerische Berechnungsverfahren im Maschinenbau,
Technische Universität Darmstadt

Darmstadt, 11. Mai 2010